CONTRACTOR REPORT

8024

Dean

RS-8232-21 *65752*

C. 1

8232-2//065752

000000001 -

A Numerical Model for Unsteady Two-Dimensional Flow Calculations With Flow Separation

J. W. Oler, J. H. Strickland, B. J. Im
Department of Mechanical Engineering
Texas Tech University
Lubbock, TX 79409

1077075

A Numerical Model for Unsteady

Two-Dimensional Flow Calculations

With Flow Separation

J.W. Oler, J.H. Strickland, and B.J. Im
Department of Mechanical Engineering
Texas Tech University
Lubbock, TX 79409

ABSTRACT

A numerical model for two-dimensional airfoils in unsteady
motion with boundary layer separation is described. The
airfoil and wake surfaces are represented by a finite set of
combined source and vortex panels. The source strengths are
prescribed to have the same magnitude as the normal relative
velocity on the surface due to the freestream and motion of
the airfoil. The vortex strengths on the airfoil surface are
determined by applying a kinematic surface tangency condition
to a Green's function representation of the potential field
while simultaneously enforcing the Kutta condition. Wake
shedding is governed by a dynamic free surface condition and
the characteristics of the flow near any boundary layer
separation points. Wake deformation is predicted by applying
a geometric free surface condition. Calculation results are
presented for steady motion, impulsively started rectilinear
motion, harmonic pitch oscillations, and constant pitching
motions. Experimental data and analytical solutions are also
presented for comparison.

TABLE OF CONTENTS

LIST OF FIGURES

NOMENCLATURE

A $\quad$ = Normal induced velocity coefficient due to vortex distribution

A^* $\quad$ = Tangential induced velocity coefficient due to vortex distribution

B $\quad$ = Normal induced velocity coefficient due to source distribution

B^* $\quad$ = Tangential induced velocity coefficient due to source distribution

c $\quad$ = Chord length of the airfoil

C_d $\quad$ = Drag coefficient

C_f $\quad$ = Skin friction coefficient

C_1 $\quad$ = Lift coefficient

C_p $\quad$ = Pressure coefficient

D $\quad$ = Normal downwash due to the freestream and motion of the airfoil

H $\quad$ = Shape parameter

k $\quad$ = Reduced frequency ($\omega c/2U_\infty$)

$\vec{n}$ $\quad$ = Surface normal at a "source" point

P $\quad$ = Pressure

R $\quad$ = Distance between "source" and "field" point

$\vec{r}$ $\quad$ = Position vector of a "field" point

Re $\quad$ = Reynolds number

S $\quad$ = Airfoil surface

s $\quad$ = Surface distance

t $\quad$ = time

$\vec{U}$ $\quad$ = Local fluid velocity

$\vec{U}_B$ $\quad$ = Airfoil translational velocity

U_e = Boundary layer edge velocity

$\vec{U}_\infty$ = Free stream velocity

$\vec{U}_R$ = Relative velocity

$\vec{u}$ = Disturbance velocity

W = Wake surface

α = Angle of attack

Φ = Total velocity potential

ϕ = Disturbance velocity potential

γ = Vortex strength

μ = Source strength

$\vec{\xi}$ = Position vector of a "source" point

$\vec{\upsilon}$ = Surface normal at a "field" point

$\vec{\omega}$ = Airfoil angular rotation vector

Γ = Circulation

δ = Boundary layer thickness

δ^* = Displacement thickness

Θ = Momentum thickness

Λ = Blockage factor

λ = Pressure gradient parameter

τ_w = Wall shearing stress

ρ = Fluid density

(Subscript)

B   = Airfoil

ℓ = Lower side

S   = Separating wake

stag = Stagnation point

TE   = Trailing edge

tr   = Transition

u   = Upper side

W   = Trailing edge wake

(Superscript)

s   = Separating wake

w   = Trailing edge wake

CHAPTER I

INTRODUCTION

1.1 Research Motivation and Objectives

The prediction of the aerodynamic behavior of an airfoil has been an important element in many engineering designs such as aircraft wings, helicopter rotors, turbomachinery vanes, propellers and prop fans. Recently, the effective utilization of wind energy has been the focus of many aerodynamic studies.

Wind turbines involve complex aerodynamic phenomena due to the randomness of the natural wind and the complexity and influence of their trailing wake structures. The overall performance of a vertical axis wind turbine may be characterized by a power output curve as is shown in Fig. 1.1. Field experiments (Ref. 27) have shown that the power produced by a Darrieus turbine at high windspeeds or low tip-to-windspeed ratios is much higher than would be expected from an analysis based on steady airfoil data. It is thought that the additional power output is a direct consequence of an unsteady flow phenomena known as dynamic stall. Although the maximum power associated with dynamic stall only occurs at infrequent high wind speeds, it is necessary to design for those peak loads. Consequently, wind energy conversion systems are over-designed for the loads which are encountered during the majority of normal operations. This adversely effects the initial system cost, energy conversion effi-

Power

current curve

ideal curve

regulation windspeed
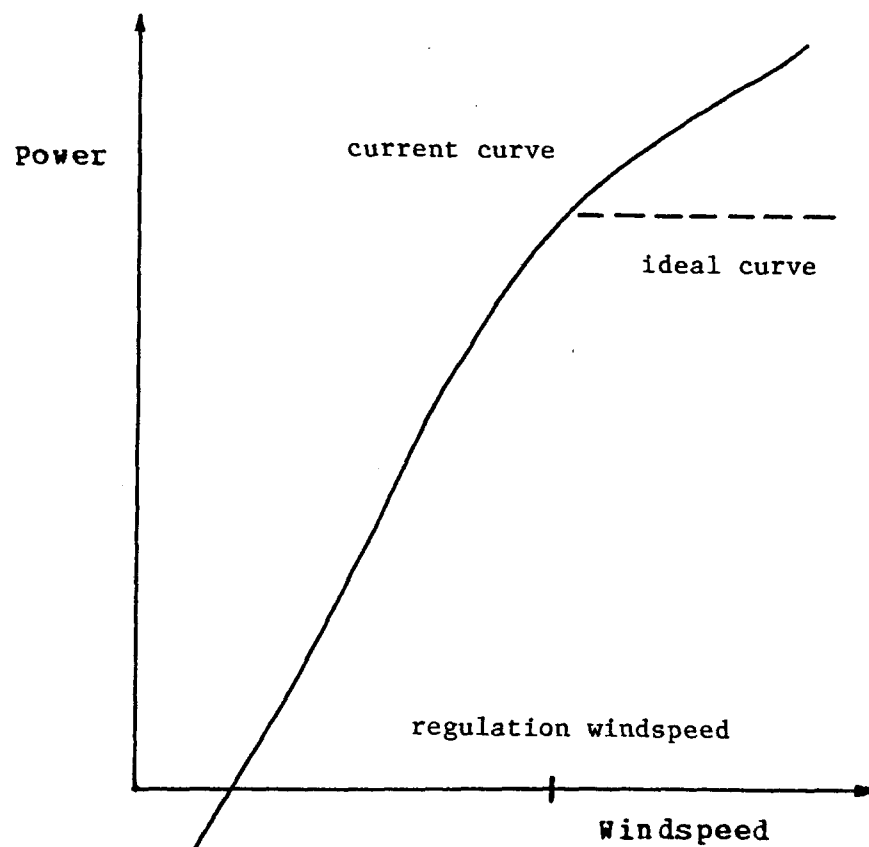
Windspeed

Figure 1.1 Power vs. Windspeed

2

ciency, and the overall cost of energy during their service life. It is desirable to identify a regulation windspeed (see Fig. 1.1) at which the power output from the turbine is a maximum. This requires the use of some sort of power regulation mechanism at windspeeds higher than the regulation windspeed.

In attempts to reduce the peak power output of a Darrieus turbine without adversely affecting its performance in the low and medium windspeed ranges, several studies of dynamic stall regulation have been conducted (Ref. 22 and 28). These experimental investigations have shown that regulation may be achieved through the design of blade sections which either passively exhibit the desired characteristics or have provisions for active boundary layer control.

A valuable tool in the design and evaluation of the aerodynamic characteristics of a blade or airfoil section is a numerical model. It allows the examination of many more new geometries at lower cost than wind tunnel or full-scale experiments. Realization of the economic benefits and flexibility of numerical aerodynamic models has given rise to many active research programs. The work reported herein is one such effort.

1.2 Review of Previous Works

A historical review of aerodynamic panel methods by Kraus (Ref. 29) reveals that one of the first applications of the method was by Smith and Hess (Ref. 50) for an airfoil with zero lift. In their study, as well as in other early efforts, airfoils were modeled with either distributed

potential source panels for nonlifting flows or vortex panels for flow with lift.

Other types of panel singularities have been evaluated in more recent studies by Robert and Saaris (Ref. 42), and Bristow, et al. (Ref. 4, 5, 6). Both utilized combined source and vortex singularities in efforts to develop a numerical model for 3-dimensional steady flows. Whole aircraft configurations have been successfully analyzed by Robert and Saaris with this approach. Bristow has developed a numerical model which is very accurate in the design of an airfoil to produce a prescribed pressure distribution as well as in the analysis of a specified airfoil geometry.

Most of the investigations using panel methods have been for steady flow, although the general method may be extended to unsteady flows as is evidenced by the works of Ashley (Ref. 3), Djojodihardjo and Widnall (Ref. 13), Summa (Ref. 52), Lewis (Ref. 31), and Oler (Ref. 40). Past utilization of the panel method has been concentrated on attached flows where the boundary layer vorticity is shed smoothly from the trailing edge and the Kutta condition is satisfied exactly.

The modeling of separated wakes using discrete vortices can be viewed as being a natural extension of unsteady panel methods. For instance, in the case of a stalled airfoil, the wake may be represented by two vortex sheets instead of the usual one for attached flow. Clements and Maull (Ref. 9) give a comprehensive review of wake modeling techniques which utilize discrete vortices. Most prior investigations of wake calculations pertain to the flow behind bluff bodies such as that by Sarpkaya and Schoaff (Ref. 46) for flow behind circular cylinders. These bluff bodies

4

were in all cases immersed in a fluid with a steady, uniform freestream velocity. Most of the investigators have utilized potential flow models based on conformal mapping techniques as opposed to utilization of the more flexible panel methods. Examples of wake modeling using discrete vortices are found in Ham (Ref. 18), Gerrard (Ref. 15), Deffenbaugh and Marshall (Ref. 12), Sarpkaya, et al. (Ref. 45, 46, 47), and Kiya and Arie (Ref. 26). In each study, the separating boundary layers were represented by an array of discrete vortices emanating from a known separation point location on the airfoil surface. Ham allowed a single vortex to be shed from the leading edge of the airfoil when its orientation exceeded an assumed stall angle of attack. Sarpkaya (Ref. 45) and Kiya also assumed the leading edge of the flat plate to be a boundary layer separation point, while Gerrard (Ref. 15) and Deffenbraug (Ref. 12) relied on experimental data for a circular cylinder.

Common difficulties reported in these investigations were the uncertainty of the determination of the fraction of boundary layer vorticity imparted to the wake at the boundary layer separation point and the unrealistic downwash associated with free wake vortices convecting close to the airfoil surface. Gerrard (Ref. 15) and Sarpkaya (Ref. 45) concluded that approximately 50 to 75% of the boundary layer vorticity should be injected into the separation wake to produce reasonable results. A similar conclusion was made in the authors' previous work (Ref. 20).

Several investigators have made extensive calculations using unsteady turbulent boundary layer codes in recent years, e.g., Nash, Carr, and Singleton (Ref. 38); Dwyer and McCroskey (Ref. 14); Telionis (Ref. 53); Daneshyar and Mugglestone (Ref. 11); and Lyrio, Ferziger, and Kline

(Ref. 32). Notable among the codes which have been developed are the several variations of a differential boundary layer model due to Nash, et al. (Ref. 39). This model may be used to predict both laminar and turbulent flows, includes unsteady effects, and is capable of predicting flow in the vicinity of separation. In addition, the model has been applied to dynamic stall problems and has been shown to yield good agreement with experimental results (see Ref. 34).

Recently, integral techniques for unsteady turbulent boundary layers have appeared in the literature. The method developed by Daneshyar and Mugglestone (Ref. 11) utilizes the unsteady momentum integral equation along with the entrainment equation and a skin friction relation derived from the Coles (Ref. 9) velocity profiles. Lyrio, Ferziger, and Kline (Ref. 32) formulated and tested a similar integral technique which gives agreement with the experimentally evaluated steady turbulent flows reported by Tillman, Herring and Norbury; Stratford, Samuel and Joubert [see Coles and Hirst (Ref. 10) for these four flows]; Kim (Ref. 25); Simpson, Strickland, and Barr (Ref. 48); and Wieghardt [see Kim (Ref. 25)]. More importantly, this method predicts the unsteady turbulent boundary layer data of Karlson (Ref. 24), and Houdeville, et al. (Ref. 19), and compares well with the finite difference methods of McCroskey and Phillippe (Ref. 34), and Singleton and Nash (Ref. 49) while being an order of magnitude faster in numerical computation time.

In summary, the strongest trends found in the current literature involve the analysis of potential flow via panel methods, separating wakes via discrete vortices, and turbulent boundary layers via a number of closure models. These techniques were combined for the first time in the author's previous work (Ref. 20) and refined in the current investigation.

CHAPTER II

THEORETICAL BACKGROUND

2.1 Governing Equations and Boundary Conditions

The present study is concerned with the motion of a two-dimensional airfoil through a homogeneous, incompressible, and inviscid fluid. The airfoil surface is represented with respect to a fluid fixed reference frame by

$$S(\vec{r},t) = 0. \tag{2.1}$$

The wake following the airfoil may be defined by a surface of potential discontinuity given by

$$W(\vec{r},t) = 0. \tag{2.2}$$

The possibility of separated flow is accounted for by allowing the wake to include a surface of potential discontinuity emanating from a boundary layer separation point as well as from the trailing edge.

Since the airfoil plus wake comprise a complete lifting system, and assuming that the ideal fluid was started from a state of rest or uniform motion, it follows that the motion is irrotational for all time. This requirement of irrotationality is a necessary and sufficient condition to guarantee the existence of a velocity potential, i.e.,

$$\nabla \times \vec{U} = 0 \tag{2.3}$$

therefore, $\vec{U} = \nabla\Phi$

$$= \vec{U}_\infty + \nabla\phi \tag{2.4}$$

where Φ = total velocity potential

  ϕ = disturbance potential due to the presence of the airfoil.

Conservation of mass for an incompressible fluid requires that the vector velocity field not diverge. This requirement may be expressed as

$$\nabla \cdot \vec{U} = 0. \tag{2.5}$$

Substituting Eq. 2.4 into Eq. 2.5 yields Laplace's equation which is the governing equation expressed in terms of the disturbance potential, i.e.,

$$\nabla^2\phi = 0. \tag{2.6}$$

A unique solution of Eq. 2.6 may be obtained through application of appropriate boundary conditions:

(1) The Infinity Condition:

   The disturbance potential resulting from the presence of the airfoil must vanish at infinity.

(2) The Kinematic Surface Tangency Condition:

   On the airfoil surface, the normal relative fluid velocity must be zero.

(3) The Kutta Condition:

   At all times, the flow of fluid from the trailing edge must be geometrically smooth and continuous.

(4) The Boundary Layer Separation Condition:

   The sheet of potential discontinuity emanating from a boundary

8

layer separation point must reflect the injection of the boundary
layer vorticity.

(5) The Dynamic Free Surface Condition:

The pressure must be continuous through the wake surfaces since they

cannot sustain a load.

(6) The Geometric Free Surface Condition:

The wake surfaces are distorted and convected downstream at local

convection velocities.

Once the potential field has been determined, the pressure distribut-
tion on the airfoil may be found from conservation of momentum which takes
the familiar form of Bernoulli's equation:

$$P = P_\infty - \rho \left[\frac{\partial \Phi}{\partial t} + \frac{1}{2} (\nabla \Phi)^2 \right].$$ (2.7)

2.2 Green's Identity for Laplace Equation

As stated in the previous section, the governing equation is the
linear Laplace equation. By use of Green's theorem (Ref. 30, pp. 57-59),
it may be shown that the disturbance velocity potential at any point in
continuous, acyclic irrotational flow may be given by

$$\phi(\vec{r},t) = - \frac{1}{2\pi} \iint_S \frac{\mu}{R} \, ds + \frac{1}{2\pi} \iint_{S+W} \sigma \frac{\partial}{\partial n} \left(\frac{1}{R} \right) ds$$ (2.8)

where, $R = \left| r - \xi \right|$, scalar distance between the "field" point r, and a
"potential source" point, $\vec{\xi}$

$n(\vec{\xi},\vec{t})$ = surface normal at a "source" point on a fluid boundary

9

The first term is the velocity potential at $\vec{r}$ due to a source distribution on the airfoil surface of strength μ per unit area, while the second term represents the velocity potential produced by a distribution of doublets on the airfoil and wake surfaces with axes normal to those surfaces, and strength σ. Therefore, the doublet strength distribution may be interpreted as the distribution of potential jump across the wake and airfoil surfaces. In actual application, this distribution of doublets is replaced by an equivalent distribution of vortices in which the local vortex strength is equal to the local gradient of the potential jump across the airfoil or wake surface. Additional details concerning the equivalent vortex distribution are given in Section 3.4.

The source and vortex strength distributions must be determined through application of the boundary conditions stated in Section 2.1. It may be noted that the first boundary condition, the infinity condition, is inherently satisfied by Eq. 2.8.

The kinematical surface tangency condition on the surface of the airfoil may be expressed (Ref. 23, pp. 190-192) as

$$\frac{1}{\left| \nabla S(\vec{r},t) \right|} \frac{\partial S(\vec{r},t)}{\partial t} + \frac{\partial \phi}{\partial \upsilon} + \vec{U}_\infty \cdot \vec{\upsilon} = 0 \qquad (2.9)$$

on $S(\vec{r},t) = 0$.

The first term of Eq. 2.9 represents the normal downwash on the airfoil due to the airfoil motion where $\vec{\upsilon}$ is the local surface normal. It may be expressed for a body fixed coordinate system as

10

$$\frac{1}{\left| \nabla S(\vec{r},t) \right|} \frac{\partial S(\vec{r},t)}{\partial t} = - (\vec{U}_B + \vec{\omega}_B \times \vec{r}) \cdot \vec{\upsilon} \qquad (2.10)$$

on $S(\vec{r},t) = 0$

where, $\vec{U}_B$ = airfoil translational velocity vector

$\vec{\omega}_B$ = airfoil angular rotation vector.

The second and third terms of Eq. 2.9 represent normal components of the disturbance velocity field and the freestream velocity, respectively. Substituting Eq. 2.10 into Eq. 2.9 and rearranging yields

$$\frac{\partial \phi}{\partial \upsilon} + (\vec{U}_\infty - \vec{U}_B - \vec{\omega}_B \times \vec{r}) \cdot \vec{\upsilon} = 0 \qquad (2.11)$$

which is valid for a body fixed reference frame. Substituting Eq. 2.8 into Eq. 2.11 yields

$$\frac{1}{2\pi} \iint_S \mu \frac{\partial}{\partial \upsilon} \left(\frac{1}{R}\right) ds + \frac{1}{2\pi} \iint_{S+W} \sigma \frac{\partial^2}{\partial n \partial \upsilon} \left(\frac{1}{R}\right) ds$$

$$= - (\vec{U}_\infty - \vec{U}_B - \vec{\omega}_B \times \vec{r}) \cdot \vec{\upsilon} \cdot \qquad (2.12)$$

This provides a governing integral equation for the unknown vortex and source strength distributions on the airfoil and wake surfaces. Once Eq. 2.12 has been solved subject to the remaining boundary conditions, the disturbance velocity at any point in the flow may be determined through Eq. 2.8.

2.3 Separated Flow Model

For modeling purposes, it is assumed that the wake may be adequately represented by two sheets of potential discontinuity. One surface extends from the trailing edge while the other originates at the boundary layer separation point as illustrated in Fig. 2.1.
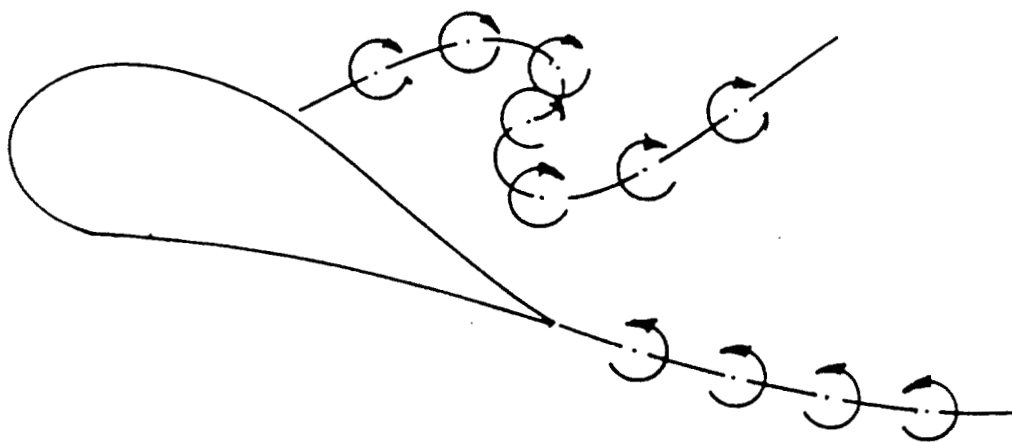
Figure 2.1 Separated Flow Model

The rates at which vorticity is shed into the two wake surfaces are related by the Kelvin-Helmholtz theorem to the rate of change of the vorticity bound to the airfoil surface and the vorticity in the boundary layer at the separation point. The theorem requires that the rate of change of the net circulation in the flow field be zero, i.e.,

$$\frac{d\Gamma_{net}}{dt} = 0$$

$$\frac{d\Gamma_B}{dt} + \frac{d\Gamma_W}{dt} + \frac{d\Gamma_S}{dt} = 0 \quad . \tag{2.13}$$

Here, the net circulation has been divided into three components: the circulation associated with the vorticity bound to the airfoil surface, Γ_B, the vorticity shed from the boundary layer separation point, Γ_S, and the vorticity shed from the trailing edge, Γ_W. The time derivatives of Γ_W and Γ_S represent the rates of vorticity shedding to the respective wake surfaces.

A simple vorticity flux analysis may be utilized to estimate the vorticity shedding rate from the boundary layer separation point, i.e.,

$$\frac{d\Gamma_S}{dt} = \int_0^\delta u \left(\frac{\partial u}{\partial y} - \frac{\partial v}{\partial x}\right) dy$$

$$\simeq \int_0^\delta \frac{1}{2} \frac{\partial u^2}{\partial y} dy \tag{2.14}$$

$$\simeq \frac{U_S^2}{2}$$

where U_S is the velocity at the edge of the boundary layer (or the surface velo-

13

city from the potential flow solution) at the boundary layer separation point. The assumption is made that 100% of the vorticity contained in the boundary layer is injected into the inviscid flow field at the separation point.

Referring to Fig. 2.2, the bound vorticity may be written as

$$\Gamma_B = {}_A\!\!\int^B \gamma_b ds$$

$$\Gamma_B = {}_A\!\!\int^B \frac{d(\Delta\sigma)}{ds} ds \qquad\qquad (2.15)$$

$$= \Delta\sigma_{TE}$$

where γ_b is the vortex strength per unit length along the airfoil surface and $\Delta\sigma$ is the distribution of potential discontinuity or doublet strength along the surface. The rate of change of bound vorticity is, therefore, equivalent to the rate of change of the difference in surface doublet strength at the trailing edge given by

$$\frac{d\Gamma_B}{dt} = \frac{d}{dt} (\Delta\sigma_{TE}). \qquad\qquad (2.16)$$

Substituting Eq. 2.14 and Eq. 2.16 into Eq. 2.13 provides an expression for the rate of shedding of vorticity to the wake surface extending from the trailing edge,

$$\frac{d\Gamma_W}{dt} = - [\frac{d}{dt} (\Delta\sigma_{TE}) + \frac{U_S^2}{2}]. \qquad\qquad (2.17)$$

Eq. 2.17 was based on the Kelvin-Helmholtz vorticity conservation theorem. The same result may be arrived at by applying the dynamic free

14
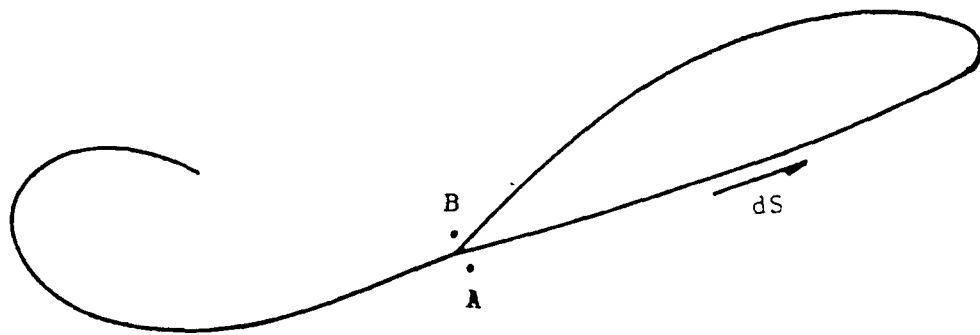
Figure 2.2   Bound Vorticity on an Airfoil

surface boundary condition at the airfoil trailing edge. Specifically the pressure must be continuous across the wake over its entire length including the point of attachment at the trailing edge. There, the pressure difference across the infinitely thin surface is zero which leads to

and
$$P_u - P_\ell = 0$$

$$\frac{\partial}{\partial t} (\phi_u - \phi_\ell) + \frac{1}{2}(\nabla\phi_u^2 - \nabla\phi_\ell^2) = 0 . \tag{2.18}$$

Recognizing that $\nabla\phi = U$ for the fluid fixed reference frame, then

$$\frac{1}{2} (U_u^2 - U_\ell^2) = - \frac{\partial}{\partial t}(\Delta\phi_{TE}) . \tag{2.19}$$

From Fig. 2.3, it is noted that $(U_u^2 - U_\ell^2)/2$ is the net rate of vorticity shedding from the boundary layers on the upper and lower surface of the airfoil at the trailing edge.

Then,

$$\frac{d\Gamma_W}{dt} = - \frac{d}{dt} (\Delta\phi_{TE}) . \tag{2.20}$$

By calculating the circulation about a curve (as shown in Fig. 2.4) which encloses the airfoil and the wake surfaces extending from the boundary layer separation point, it follows that

$$\frac{d}{dt} (\Delta\phi_{TE}) = \frac{d\Gamma_B}{dt} + \frac{d\Gamma_S}{dt} . \tag{2.21}$$

So,

$$\frac{d\Gamma_W}{dt} = - (\frac{d\Gamma_B}{dt} + \frac{d\Gamma_S}{dt}) \tag{2.22}$$

which is equivalent to the result obtained from the Kelvin-Helmholtz theorem.

16
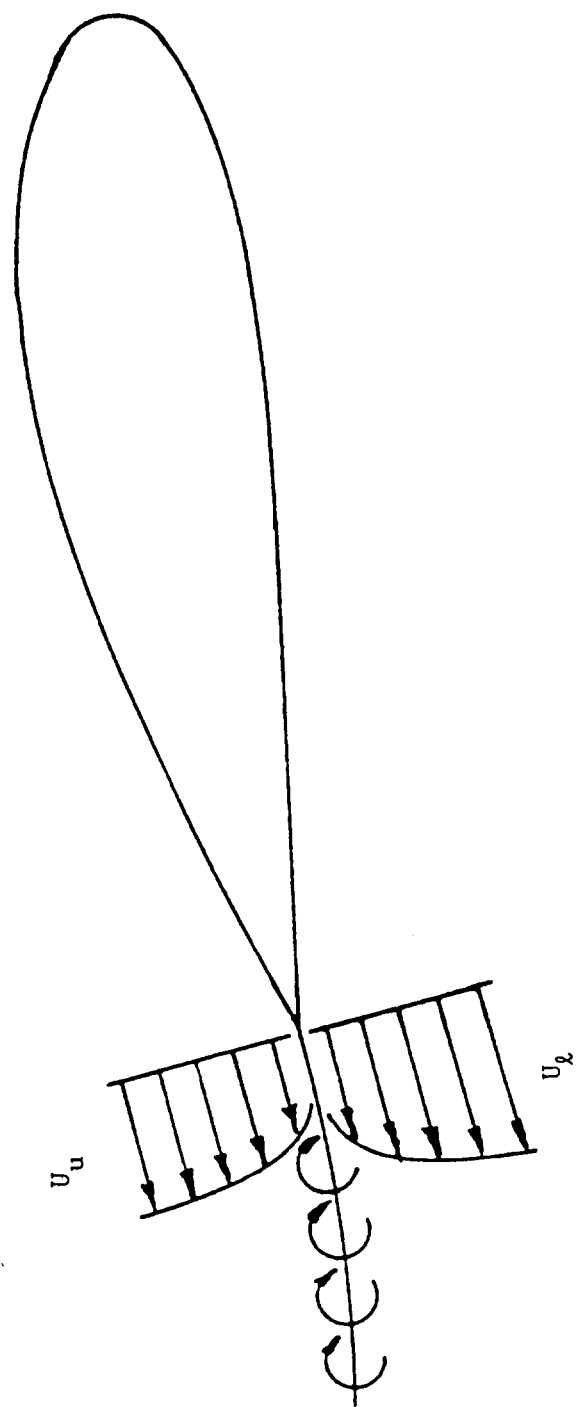
Figure 2.3   The Net Rate of Vorticity shedding at Trailing Edge
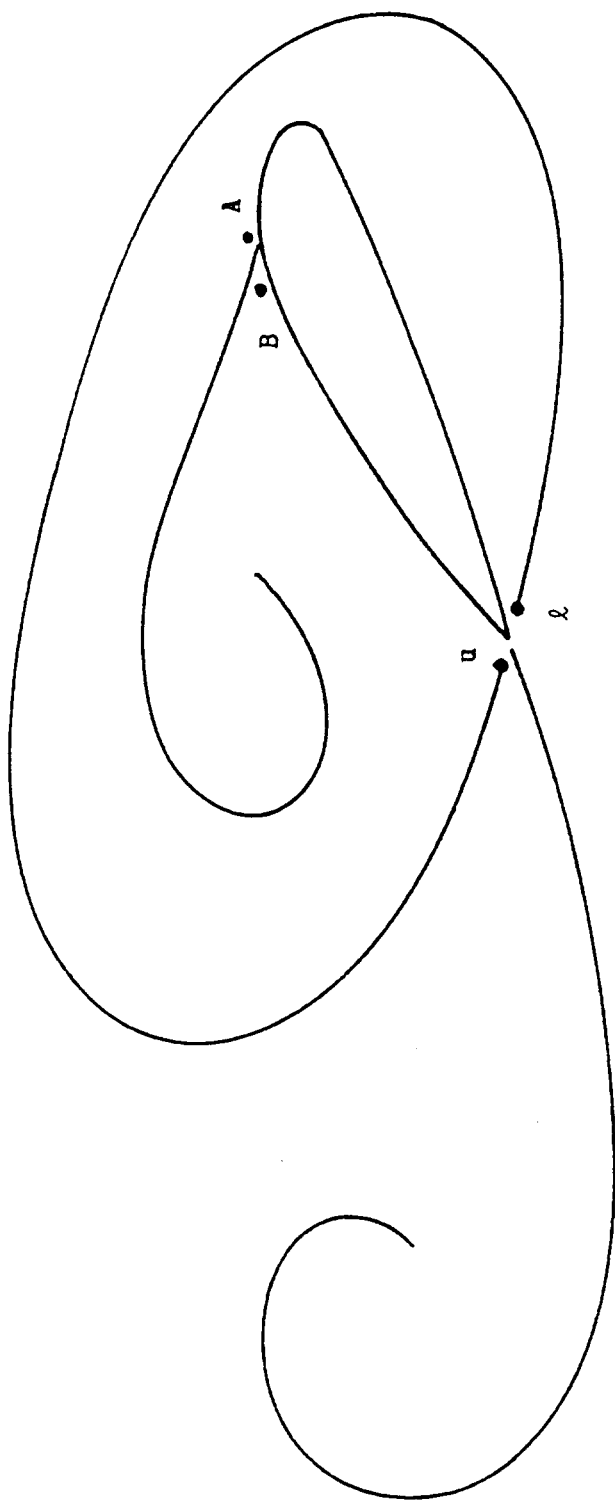
Figure 2.4   The Rate of Change of Potential Jump Across
the Trailing Edge

An important consequence of boundary layer separation may be noted by applying the dynamic free surface condition to the wake surface extending from the separation point. Referring to Fig. 2.4, points A and B are located an infinitesimal distance ahead of and behind the boundary layer separation point. The pressure difference between the two points or across the separating wake surface must be zero. This results in

$$0 = \frac{\partial}{\partial t} (\phi_A - \phi_B) + \frac{1}{2} (\nabla \phi_A^2 - \nabla \phi_B^2) . \qquad (2.23)$$

As in Eq. 2.19

$$\frac{\partial \Gamma_S}{\partial t} = \frac{1}{2} (\nabla \phi_A^2 - \nabla \phi_B^2) . \qquad (2.24)$$

Substituting into Eq. 2.23 yields

$$\frac{\partial \phi_B}{\partial t} = \frac{\partial \phi_A}{\partial t} + \frac{d\Gamma_S}{dt} . \qquad (2.25)$$

Therefore, behind the boundary layer separation point, there is an additional increment to $\partial \phi / \partial t$ equal to the rate of vorticity shedding from the separation point.

The existence of the additional contribution to $\partial \phi / \partial t$ within the separation region may be verified by considering the rate of change of the potential jump across the trailing edge as described by Eq. 2.21. This equation may be rewritten as

$$\frac{d\phi_u}{dt} = \frac{d\phi_\ell}{dt} + \frac{d\Gamma_B}{dt} + \frac{d\Gamma_S}{dt} . \qquad (2.26)$$

For the case of a steady, stalled airfoil, the average rates of change of Γ_B and ϕ_ℓ are zero, yet the $\partial \phi_u / \partial t$ is not zero due to the vorticity being shed from the boundary layer separation point.

19

The additional contribution to $\partial\Phi/\partial t$ in the separated region is essential in the calculation of the pressure distribution around the airfoil. Without its inclusion, a finite pressure jump would be indicated across the two wake surfaces and erroneous predicted values of lift and drag would result.

2.4 Boundary Layer Model

The boundary layer model required in this work must meet several requirements. It should be able to predict both laminar and turbulent portions of the flow as well as the transition region between them as is indicated in Fig. 2.5. It is also necessary to predict the location of a possible boundary layer separation point given a pressure or edge velocity distribution. Boundary layer models may generally be classified as either finite difference, finite element or integral models. Among the various techniques, the momentum integral method has been chosen for the current work. It not only meets the above requirements but also has the advantage of being less expensive computationally while yielding comparable accuracy (Ref. 34).

2.4.1 Momentum Integral Equation

The turbulent boundary layer analysis used here is orginally due to Lyrio, et al. (Ref. 32) and extended for the present work by Strickland (Ref. 51). The formulation for the laminar portion of the boundary layer is based on Thwaites method (see Ref. 7). The major extension of the method for the present study is the inclusion of unsteady terms in the momentum integral equation.

20
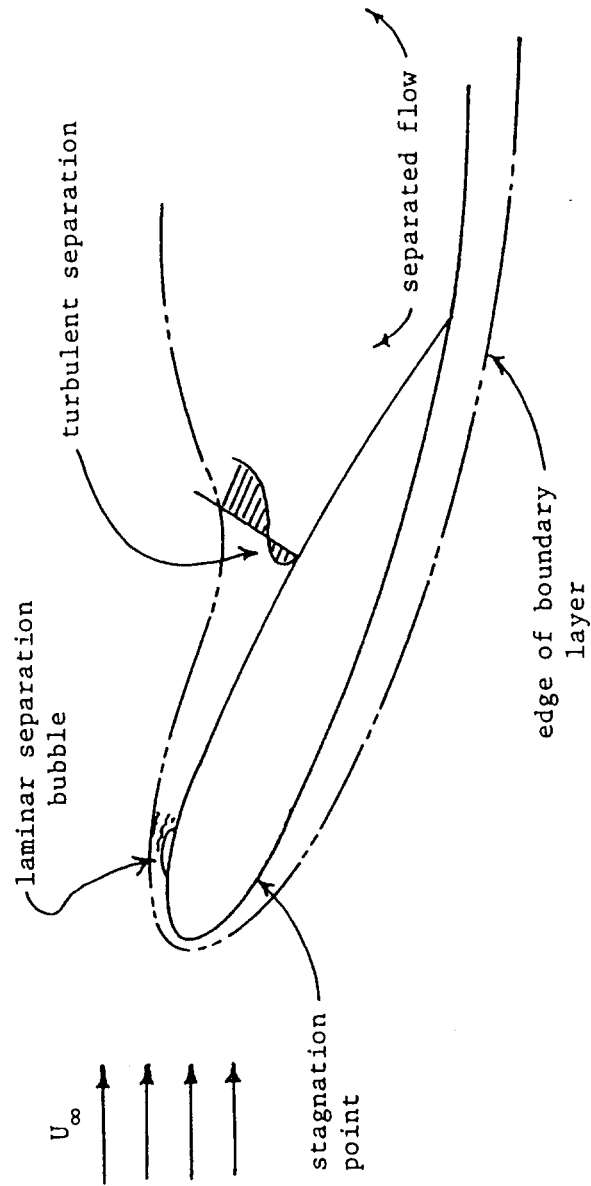
Fig. 2.5 Boundary Layer Characteristics of an Airfoil
at High Angle of Attack

The unsteady momentum integral equation which is valid for both laminar and turbulent flow may be written as

$$\frac{1}{U_e^2} \frac{\partial}{\partial t} (U_e \delta^*) + \frac{\partial \theta}{\partial s} + \frac{1}{U_e} \frac{\partial U_e}{\partial s} (2\theta + \delta^*) = \frac{C_f}{2} \qquad (2.27)$$

where U_e, θ, δ^* and C_f are the freestream velocity, momentum thickness, displacement thickness, and friction factor, respectively. For the laminar formulation, a pressure gradient parameter, λ, is defined as

$$\lambda = \frac{\theta}{U_e} R_\theta \left(\frac{\partial U_e}{\partial s} + \frac{1}{U_e} \frac{\partial U_e}{\partial t} \right) \qquad (2.28)$$

where R_θ is the Reynolds number based on U_e and θ. To obtain a solution for the laminar formulation, auxiliary relations between $C_f/2$, θ, and δ^* must be utilized. The following correlations are obtained based on wedge flow solutions (Ref. 7):

$$\frac{C_f}{2} = \frac{1.91 - 4.13\Lambda}{R_e^*}$$

$$H = (0.680 - 0.922\Lambda)^{-1} \qquad (2.29)$$

$$\Lambda = 0.325 - 0.130\lambda H^2 .$$

Here, H is the usual shape parameter, δ^*/θ, Λ is the blockage factor δ^*/δ, and R_e^* is the Reynolds number based on U_e and δ^*.

The turbulent boundary layer model utilizes an entrainment equation given by

$$\frac{1}{U_e} \frac{\partial}{\partial S} [U_e(\delta - \delta^*)] = F . \qquad (2.30)$$

The entrainment function F is calculated from the following auxiliary equations

$$\frac{dF}{dS} = .025(F_e - F)\delta$$

$$F_e = 4.24 \ K_e \ \left(\frac{\Lambda}{1 - \Lambda}\right)^{.916} \tag{2.31}$$

$$K_e = .013 + .0038e^{-\beta/15}$$

$$\beta = \frac{\delta^*}{\tau_w}\frac{dP}{dx}$$

Where τ_w is the wall shearing stress and dP/dx is the streamwise pressure gradient. Shape factor relationships are obtained from the following general velocity profile:

$$\frac{U}{U_e} = 1 + V_T \ln \left(\frac{y}{\delta}\right) - V_B \cos^2 \left(\frac{\pi y}{2\delta}\right)$$

$$V_T = \frac{1}{.41}(\text{sgn} \ \frac{C_f}{2})(\frac{C_f}{2})^{1/2} \tag{2.32}$$

$$V_B = 2 \ (\Lambda - V_T)$$

$$\frac{C_f}{2} = \frac{\tau_w}{\rho U_e^2}$$

where U is the velocity in the boundary layer at a distance y from the wall and ρ is the fluid density. The skin friction law is given by

$$\frac{C_f}{2} = .051 \ |1 - 2\Lambda|^{1.732} \ \left(\frac{R_e^*}{\Lambda}\right)^{-.268} \quad \text{sgn}(1 - 2\Lambda). \tag{2.33}$$

Additional details concerning the entrainment, wall shear stress and skin friction relations may be found in Ref. 32.

2.4.2 Transition and Separation Criteria

Transition of the laminar boundary layer to a turbulent boundary layer is assumed to occur in one of two ways. In the first case, a separation bubble is formed near the leading edge. This consists of a separating laminar shear layer, transition to turbulence, and possible reattachment as a turbulent boundary layer. In some cases, the shear layer may not reattach and the boundary layer simply separates at that point. In the present model, the streamwise extent of the separation bubble is assumed to be small and turbulent boundary layer reattachment is assumed to begin at the point of laminar separation which is indicated by a value of $H \geq 4.0$. Laminar separation is indicated by the immediate separation of the turbulent boundary layer. A more complete model for the separation bubble has been proposed and tested by Roberts (Ref. 43) and Arena and Mueller (Ref. 2) and should be evaluated for inclusion in the current boundary layer code.

In the absence of a laminar separation bubble, transition may occur by virtue of laminar instabilities. This transition mode can be predicted using the criteria due to Cebecci and Smith (Ref. 7), i.e.,

$$R_\theta = 1.174 \quad (1 + \frac{22,400}{Re_{xtr}} \quad Re_{xtr}^{0.46}) . \tag{2.34}$$

Here, R_θ and Re_{xtr} are Reynolds numbers based on the momentum thickness and distance from the forward stagnation point, respectively.

The separation criteria associated with the unsteady boundary layer is more complicated than for the steady case in which it is generally assumed that separation occurs at a position of zero wall shear stress. For example, it is evident that no separation occurs from a flat plate oscillating parallel to its own surface in a stationary fluid even though the wall shear stress goes to zero twice during each cycle. In spite of this apparent paradox, several investigators have concluded that if properly interpreted, the shear stress must vanish at some point within the boundary layer and in addition, the velocity relative to a coordinate frame moving with the separation point must vanish at the same location. These criteria are also consistent with the findings of Nash and Patel (Ref. 37) in that they conclude that separation will occur if and only if the typical reversed flow velocities exceed the rate of penetration of the reversed flow into the oncoming boundary layer. Neither of these methods may be easily incorporated into an integral boundary layer calcuation due to the lack of prediction detail concerning the instantaneous velocity distribution in the boundary layer.

An alternate separation criteria which has been utilized in the present work is based on monitoring any rapid increase in the various boundary layer parameters such as the displacement thickness or the velocity component normal to the surface. Nash and Patel (Ref. 37) use a crude criterion to identify the approximate location of separation. Boundary layer separation is assumed to occur at the point at which the displacement thickness exceeds 10% of the chord length. In the work of Lyrio, the "fully developed" separation point is defined to occur at the point where $\Lambda = 0.5$. The "intermittent" separation point occurs upstream of the "fully developed" separation point. According to the Sandborn (Ref. 44) correla-

25

tion, the intermittent separation point occurs when

$$H > \frac{2 - \Lambda}{1 - \Lambda} .$$ (2.35)

After considerable experimentation, it was determined that the intermittent separation point criterion yields more reliable predictions of boundary layer separation than the fully developed separation point criterion within the context of the current aerodynamic prediction code.

2.4.3 Numerical Solution

Numerical solutions of the boundary layer equations are obtained using an explicit finite difference formulation of Eq. 2.27. For the laminar formulation, Eqs. 2.27, 2.28 and 2.29 can be cast in the following form:

$$A \frac{\partial \delta^*}{\partial x} = B .$$ (2.36)

This equation is integrated over an interval Δx using a fourth order Runge-Kutta method to yield the variation of δ^* as a function of x at a given time step. Time derivatives with respect to x are obtained from forward differences. These derivatives are held constant over the integration interval Δx. The integration interval Δx is further subdivided into at least eight subintervals. For the turbulent formulation, Eqs. 2.27, 2.30, 2.31, 2.31 and 2.33 may be organized to yield a pair of simultaneous equations:

$$\begin{bmatrix} A_{11} & A_{12} \\ A_{21} & A_{22} \end{bmatrix} \begin{Bmatrix} \dfrac{\partial \delta^*}{\partial x} \\ \dfrac{\partial \Lambda}{\partial x} \end{Bmatrix} = \begin{Bmatrix} B_1 \\ B_2 \end{Bmatrix} .$$ (2.37)

A fourth order Runge-Kutta method is used to calculate simultaneous values of δ^* and Λ as a function of x.

Experimentation with the boundary layer calculations has indicated that the unsteady boundary layer terms have a second order effect on the overall airfoil calculations. Consequently, they have been suppressed for all of the calculation results presented in Chapter IV.

CHAPTER III

SOLUTION METHOD

3.1 General Solution Procedure

As is described in Section 2.2 the governing integral relation is

$$\frac{1}{2\pi} \iint_S \mu \frac{\partial}{\partial \upsilon} \frac{1}{R} ds + \frac{1}{2\pi} \iint_{S+W} \phi \frac{\partial^2}{\partial n \partial \upsilon} \frac{1}{R} ds .$$

$$= - (\vec{U}_\infty - \vec{U}_B - \vec{\omega}_B \times \vec{r}) \cdot \vec{\upsilon} \qquad (3.1)$$

The solution of Eq. 3.1 is made difficult by the nonlinearity which arises

from the fact that the vortex distribution on the wake as well as the wake

geometry is dependent on the history of the vorticity and source distribu-

tions on the airfoil surface. That is, the location of the wake at any instant

is a function of the previous velocity potential fields which are also

functions of the previous wake geometries. One approach to overcoming this

difficulty and obtaining a solution to Eq. 3.1 is the following

step-by-step procedure:

(1) At $t = 0$, let the airfoil be started impulsively and the freestream

velocity brought instantaneously to $\vec{U}_\infty$ with respect to the sta-

tionary coordinate system. For this instant, there is no wake sur-

face and no contribution to the downwash on the airfoil due to the

wake. Therefore, a unique solution for the potential field may be

found through the application of appropriate boundary conditions.

28

(2) Over the next infinitesimal time increment, assume that the velocity field is unchanged. As a result, the geometry of the wake surface generated during that time increment may be predicted through application of the Kutta and boundary layer separation conditions. In addition, at later time steps, the new geometry of existing wake surfaces may be predicted through application of the geometric free surface condition.

(3) With the new geometries of the wake surfaces determined the integration over the wake surfaces in Eq. 2.12 for the next time increment may be accomplished. Therefore, the governing equation may again be solved through the appropriate boundary conditions.

(4) Steps (2) and (3) are repeated so that the solution proceeds in a step-by-step manner towards the steady state or periodic final result.

3.2 Numerical Solution by the Collocation Method

With the boundary conditions described in Section 2.1, the objective is to develop a technique for solving the governing integral equation, Eq. 3.1, with the aid of a digital computer. For this purpose, the airfoil and wake surfaces are discretized into N_B and $N_W(t)$ elements as shown in Fig. 3.1.

On the airfoil, the surface distribution of potential sources is represented as a piecewise linear distribution. This distribution is uniquely defined in terms of the source strength at the center or control point of each element and a zero source strength at the trailing edge. Consequently, there are N_B model degrees of freedom associated with the air-
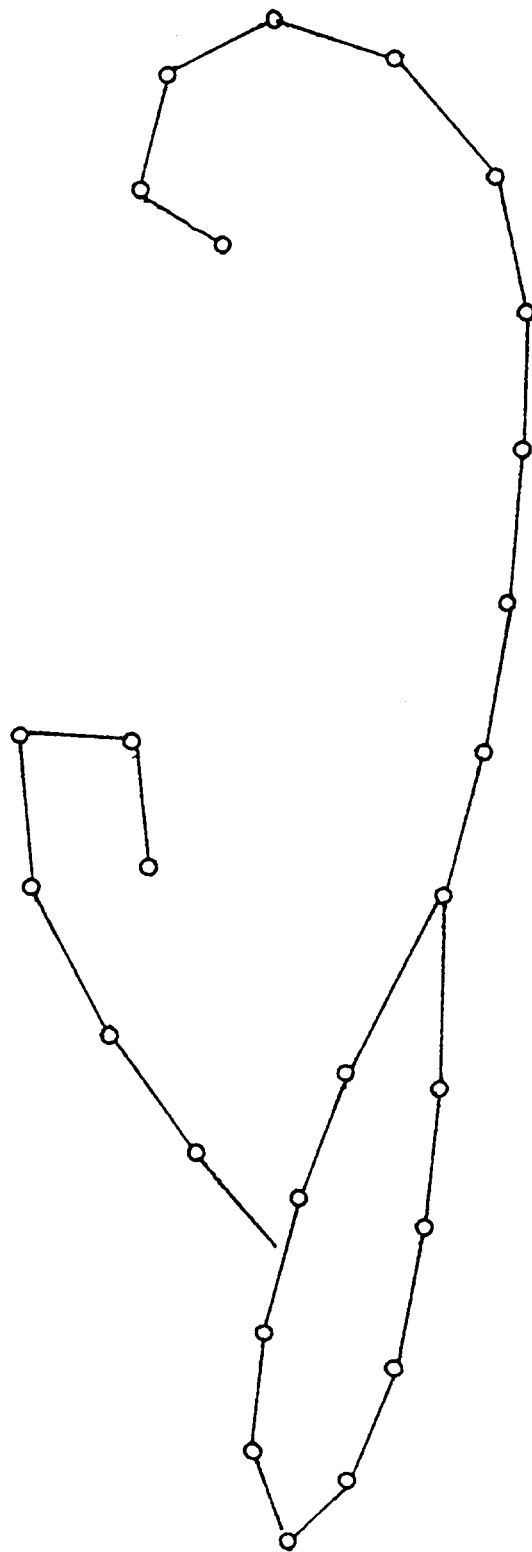
Figure 3.1 Finite Element Representation of Airfoil and Wake Surfaces

foil source distribution.

The surface distribution of potential doublets is represented by a piecewise linear distribution of potential vortices which is equivalent to a quadratic doublet distribution. This distribution is uniquely defined in terms of the vortex strengths at the element boundaries. Allowing independent endpoint vortex strengths for the upper and lower surface elements at the trailing edge, there are N_B+1 model degrees of freedom associated with the airfoil vorticity (or doublet distribution).

The distributions of potential jump on the wake surfaces are represented by lumped vortex distributions which are equivalent to piecewise uniform doublet distributions. Each wake element is modeled as a single lumped vortex located at the element midpoint. The single exception to this modeling strategy is the trailing wake nascent vortex (the trailing wake element immediately adjacent to the trailing edge). The potential jump distribution on this element is represented by a linear vorticity distribution. The endpoint strengths for the nascent element are the sum of the upper and lower surface vortex strengths at the airfoil trailing edge and a free parameter at the downstream edge. Therefore, there are a total of $N_W(t)$ model degrees of freedom associated with the wake potential jump distribution. There are also $2N_W(t)$ degrees of freedom associated with the geometry of the piecewise linear wake surfaces. However, those geometries are allowed to evolve in a step-by-step manner as described in Section 3.1 and are not discussed here in the same context as the singularity distributions.

Summarizing, the present numerical modeling technique leads to $2N_B+N_W+1$ degrees of freedom for which there must be an equal number of constraints or boundary conditions.

31

Application of the Kutta condition for the present model consists of requiring parallel flow on the nascent trailing wake element or equivalently, flow at the trailing edge parallel to the trailing edge bisector. This is equivalent to a surface tangency condition and provides an additional boundary condition.

The Kelvin-Helmholtz vorticity conservation theorem requires that the total vorticity within the flow be constant at all times. Application of the theorem to the current model yields an algebraic relation between all vorticity elements in the flow.

The strengths of all wake lumped vortices are determined at the time that they are shed from the airfoil surface. At the boundary layer separation point, this consists of the flux of boundary layer vorticity which occurs during a numerical time step. At the trailing edge, wake vortices are formed such that they represent the total vorticity that had been distributed on the nascent vortex before convecting downstream. The strengths of the wake vortices are constant as they convect downstream. Hence, in a situation in which boundary layer separation is occurring, the strengths of $N_W(t)-3$ wake vortices are determined by the development history of the flow. The strengths of two additional vortices are determined by the shedding conditions at that time instant. These considerations lead to a total of N_W-1 boundary conditions on the wake vorticity distribution.

Thus far, application of the surface tangency, Kutta, flow field circulation and wake boundary conditions have provided a total N_B+N_W+1 constraints on the overall problem solution. The remaining N_B constraints

32

required for a unique problem solution are provided by arbitrarily setting the airfoil surface source strengths such that they offset the normal downwash on the airfoil due to the relative velocity between the freestream and airfoil surface.

The combination of aerodynamic model degrees of freedom and boundary conditions which have been described represent the most general case of an unsteady airfoil motion with boundary layer separation. If there is no boundary layer separation or the motion is steady, the model is simplified significantly. Examples of the equations sets associated with these special cases are given in Section 3.5.

3.3 Determination of the Source Strength Distribution

As was discussed in Section 2.2, the solution to the governing Laplace equation can be expressed in terms of integrals of induced potentials due to boundary distributions of sources and vortices (or doublets). The surface integrals may be numerically evaluated by using the collocation technique which was described in the previous section. Application of the boundary conditions leads to a set of system equations through which the unknown vortex strengths can be expressed in terms of the total downwash and prescribed source strengths. The system equations have an excess number of degrees of freedom so that the source strengths may be arbitrarily prescribed and the proper vortex strengths will automatically adjust to fit the physical boundary conditions. It follows that there are unlimited combinations of source and vortex distributions which can induce the same flow field and satisfy the same boundary conditions.

33

The prescription of an airfoil source strength distribution is a model feature that may be freely chosen to optimize various aspects of the model's performance. The only limitation on the choice of source strength is that the rationale utilized should guarantee zero net flow to the interior of the airfoil. The significance of this may be understood by considering the boundary of the airfoil to be a closed streamline across which there can be no mass flux. Accordingly, the mass of the imaginary flow locked inside of the airfoil should remain constant.

Satisfaction of this requirement can be asssured in one of the three ways:

1. Establish an algebraic relationship between the normal velocity induced by the source panels.

2. Set all source strengths to zero.

3. Set source strengths equal to the normal relative velocity between the airfoil and freestream, i.e.,

$$\mu = -(\vec{U}_R \cdot \vec{n}) .$$ (3.2)

In an earlier study by the author (Ref. 20), the second approach was utilized for the sake of simplicity. The third strategy has been applied in the present investigation and found to give more stable solutions with less sensitivity to the distribution of panels on the airfoil. The explanation for the improvement of the calculations is that the source distribution reduces the magnitude of the downwash which must be balanced by the vorticity distribution. Consequently, the resulting vortex strengths are all within one order of magnitude, thereby improving the numerical accuracy of the calculations. The same observation has been made by Bristow (Ref. 5).

34

3.4 Influence Coefficients
Evaluation

To summarize, for an irrotational potential field, a unique solution
is obtained by representing the flow boundaries with a combination of
source and vorticity singularity distributions. The flow boundaries are
discretized into a finite number of planar surface panels for numerical
representation. With the exception of the wake element immediately adjacent
to the trailing edge, all wake vorticity is lumped into discrete, point
vortices. The strength of the wake vortices is determined at the time of
their generation and is constant thereafter.

Each panel on the airfoil surface consists of a combination of linear
vortex and source distributions. The vorticity distribution is defined in
terms of the vortex strengths at element endpoints while the source distri-
bution utilizes source strengths at element centroids. Due to the
linearity of the governing Laplace equation, the cumulative induced poten-
tial and velocity at any point in the flow or on a boundary can be calcu-
lated as a linear sum of the individual contributions of the boundary
elements. Therefore, it is computationally convenient if the individual
contributions can be expressed in terms of endpoint and centroid strengths
and multiplying coefficients. These coefficients are known as influence
coefficients and are functions of the boundary geometry.

In this section, influence coefficients for the linearly varying
vortex, the point vortex, and the linearly varying source singularities are
derived.

A general linearly varying vortex distribution on a panel designated B,
adjacent to panels A and C is illustrated in Fig. 3.2. The ξ and η element
axis are tangent and perpendicular, respectively, to the B panel. The vor-
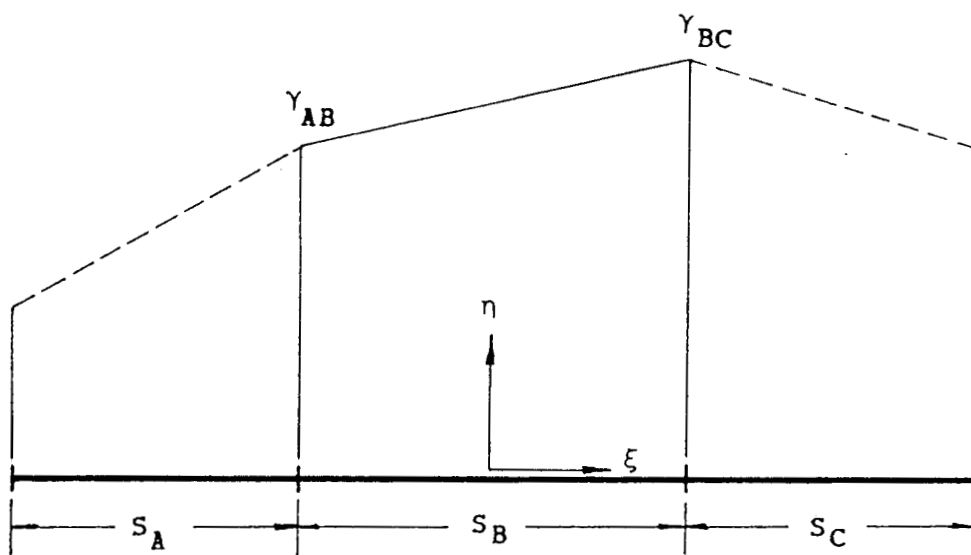
Figure 3.2 Linearly Varying Vortex Distribution

tex distribution function $\gamma(\xi)$ may be expressed in terms of the vortex strength at the end points of panel B, γ_{AB} and γ_{BC}:

$$\gamma(\xi) = \frac{1}{2} \ (\gamma_{AB} + \gamma_{BC}) + (\frac{\gamma_{BC} - \gamma_{AB}}{S_B} \ \xi) \ . \tag{3.3}$$

This equation illustrates that the vortex function $\gamma(\xi)$ may be treated as the sum of uniform and symmetrically linear functions.

The linearly varying source distribution on the panel B illustrated in Fig. 3.3 may be treated as a composition of two functions, $\mu_L(\xi)$ and $\mu_R(\xi)$. The source distribution function on the left side of the panel B is defined by μ_A and μ_B, that on the right side by μ_B and μ_C. The corresponding relations for the left and right sides are

$$\mu_L \ (\xi) = \mu_B + \frac{\mu_B - \mu_A}{\frac{1}{2}(S_A + S_B)} \ \xi \ : \ -\frac{1}{2} \ S_B \leq \xi \leq 0 \tag{3.4}$$

$$\mu_R \ (\xi) = \mu_B + \frac{\mu_C - \mu_B}{\frac{1}{2}(S_B + S_C)} \ \xi \ : \ 0 \leq \xi \leq \frac{1}{2} \ S_B \ . \tag{3.5}$$

The normal induced velocity at a "field" point due to the combined source and vortex distribution may be calculated as follows. First, a (ξ, η) -coordinate system is generated for the influencing panel as in Fig. 3.4. Then, the coordinates of the control point of interest are converted into the (ξ, η) -system by applying:

$$\xi_p = [x_p - \frac{1}{2}(x_i + x_{i+1})] \cos \theta_i + [y_p - \frac{1}{2}(y_i + Y_{i+1})] \sin \theta_i \tag{3.6}$$

$$\eta_p = [y_p - \frac{1}{2}(y_i + y_{i+1})] \cos \theta_i - [x_p - \frac{1}{2}(x_i + x_{i+1})] \sin \theta_i \ . \tag{3.7}$$
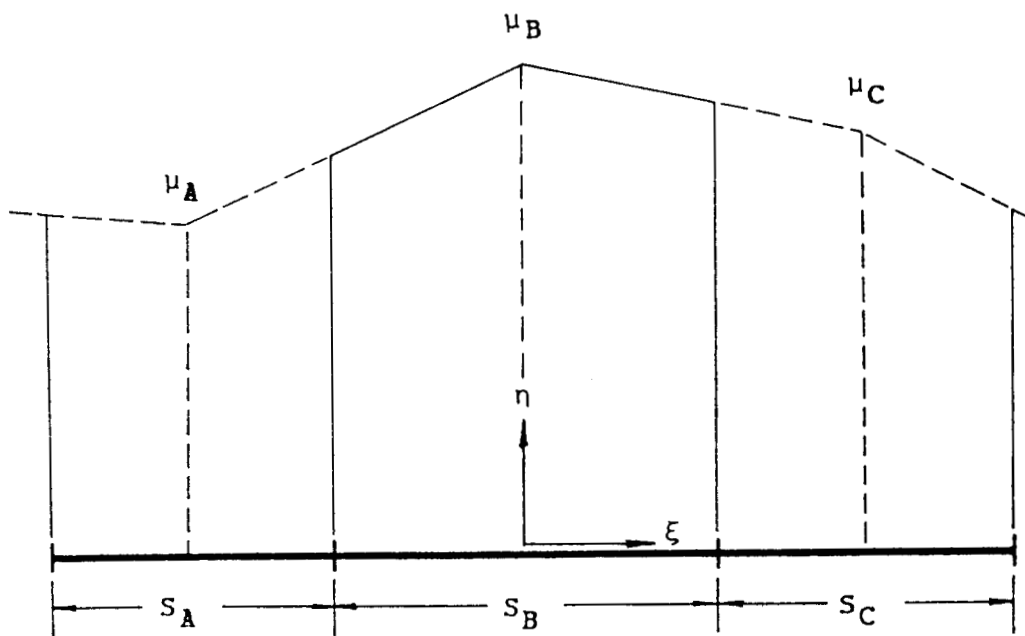
Figure 3.3   Linearly Varying Source Distribution

38
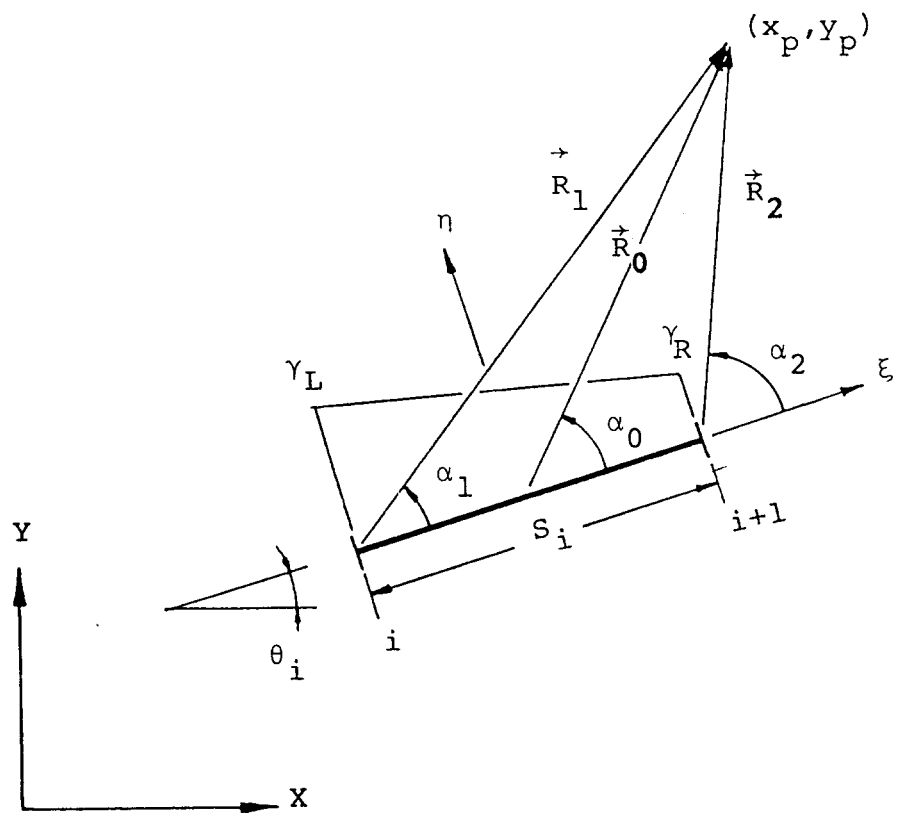
Figure 3.4   Coordinate System For a Singularity Panel

The normal and tangential components of the induced velocities from the single source or vortex element can be obtained by integrating the influence from point i to i+1 in Fig. 3.4 (see Appendix A for a complete explanation).

The use of the following definitions makes it convenient to express the resultant equations:

$$R_0^2 = \xi_p^2 + \eta_p^2$$

$$R_1^2 = (\xi_p + \frac{S_i}{2})^2 + \eta_p^2$$

$$R_2^2 = (\xi_p - \frac{S_i}{2})^2 + \eta_p^2$$

$$\alpha_0 = \tan^{-1} (\frac{\eta_p}{\xi_p})$$

$$\alpha_1 = \tan^{-1} (\frac{\eta_{PS_i}}{\xi_p + \frac{i}{2}})$$

$$\alpha_2 = \tan^{-1} \frac{\eta_{PS_i}}{\xi_p + \frac{i}{2}}$$

$$Z_1 = \frac{1}{2} \ln (\frac{R_1^2}{R_2^2})$$

$$Z_2 = \frac{1}{2} \ln (\frac{R_1^2}{R_0^2})$$

$$Z_3 = \frac{1}{2} \ln (\frac{R_0^2}{R_2^2}) .$$

(3.8)

40

The equations for induced velocity from the different types of singularity distributions are.

<u>Unit Source</u> $\mu(\xi) = 1$

$$U_{s1} = Z_1/2\pi \tag{3.9}$$

$$V_{s1} = (\alpha_2 - \alpha_1)2\pi$$

<u>Unit Vortex</u> $\gamma(\xi) = 1$

$$U_{v1} = (\alpha_1 - \alpha_2)/2\pi \tag{3.10}$$

$$V_{v1} = Z_1/2\pi$$

<u>Left-Half of Unit Linear Source</u> $\mu(\xi) = \xi$

$$U_{SL} = \left[\xi_p Z_2 - \frac{S_i}{2} + \eta_p(\alpha_0 - \alpha_1)\right]/2\pi$$

$$V_{SL} = \left[\xi_p(\alpha_0 - \alpha_1) - \eta_p Z_2\right]/2\pi \tag{3.11}$$

<u>Right-Half of Unit Linear Source</u> $\mu(\xi) = \xi$

$$U_{SR} = \left[\xi_p Z_3 - \frac{S_i}{2} + \eta_p(\alpha_2 - \alpha_0)\right]/2\pi$$

$$V_{SR} = \left[\xi_p(\alpha_2 - \alpha_0) - \eta_p Z_3\right]/2\pi \tag{3.12}$$

<u>Unit Linear Vortex</u> $\gamma(\xi) = \xi$

$$U_{V2} = \left[\xi_p(\alpha_1 - \alpha_2) + \eta_p Z_1\right]/2\pi$$

$$V_{V2} = \left[\xi_p Z_1 - S_i - \eta_p(\alpha_1 - \alpha_2)\right]/2\pi \tag{3.13}$$

In Eqs. 3.9 through 3.13, U and V represent the ξ and η components of the induced velocity, respectively. The induced velocity components may be transformed to the (x,y)-system using

$$U_x = U_\xi \cos\theta_i - V_\eta \sin\theta_i$$

$$V_y = U_\xi \sin\theta_i + V_\eta \cos\theta_i. \tag{3.14}$$

By combining Eqs. 3.3, 3.4, and 3.5 with Eqs. 3.9 through 3.14, it is possible to determine the induced velocity at (x_p, y_p) as illustrated in Fig. 3.4. On the airfoil, it is necessary to consider the normal and tangential components of the induced velocity with respect to the "field" panel P with the normal unit vector, $\vec{n}_p$. Denoting H as the normal component, Eq. 3.14 reduces to

$$H_p = (U_x \vec{i} + V_y \vec{j}) \cdot \vec{n}_p. \tag{3.15}$$

If the same subscripts are used for H as in the Eqs. 3.9 through 3.13, then the total induced normal velocity on the field panel P can be calculated from the following equation:

$$H_p = \frac{1}{2} (\gamma_{AB} + \gamma_{BC}) H_{V1} + \left(\frac{\gamma_{BC} - \gamma_{AB}}{S_B}\right) H_{V2} +$$

$$\mu_B H_{S1} + \frac{\mu_B - \mu_A}{\frac{1}{2}(S_A + S_B)} H_{SL} + \frac{\mu_C - \mu_B}{\frac{1}{2}(S_B + S_C)} H_{SR} \tag{3.16}$$

or

$$H_p = \left(\frac{1}{2} H_{V1} - \frac{H_{V2}}{S_B}\right) \gamma_{AB} + \left(\frac{1}{2} H_{V1} + \frac{H_{V2}}{S_B}\right) \gamma_{BC}$$

$$- \frac{H_{SL}}{\frac{1}{2}(S_A + S_B)} \mu_A + \left(H_{S1} + \frac{H_{SL}}{\frac{1}{2}(S_A + S_B)} - \frac{H_{SR}}{\frac{1}{2}(S_B + S_C)}\right) \mu_B$$

$$+ \frac{H_{SR}}{\frac{1}{2}(S_B + S_C)} \mu_C. \tag{3.17}$$

42

The coefficients of μ_A, μ_B, μ_C, γ_{AB}, and γ_{BC} are the desired normal induced velocity influence coefficients. The corresponding relations for the tangential induced velocity are

$$J_p = (U_x \vec{i} + V_y \vec{j}) \cdot \vec{t}_p \tag{3.18}$$

or

$$J_p = (\frac{1}{2} J_{V1} - \frac{J_{V2}}{S_B}) \gamma_{AB} + (\frac{1}{2} J_{V1} + \frac{J_{V2}}{S_B}) \gamma_{BC}$$

$$- \frac{J_{SL}}{\frac{1}{2}(S_A + S_B)} \mu_A + (J_{S1} + \frac{J_{SL}}{\frac{1}{2}(S_A + S_B)} - \frac{J_{SR}}{\frac{1}{2}(S_B + S_C)}) \mu_B$$

$$+ \frac{J_{SR}}{\frac{1}{2}(S_B + S_C)} \mu_C . \tag{3.19}$$

All the terms of Eqs. 3.17 and 3.19 are defined as functions of the geometry of the airfoil and its orientation with respect to the freestream. Therefore, Eqs. 3.17 and 3.19 can be cast in the form

$$H_p = A_1 \gamma_{AB} + A_2 \gamma_{BC} + B_1 \mu_A + B_2 \mu_B + B_3 \mu_C \tag{3.20}$$

$$J_p = A_1^* \gamma_{AB} + A_2^* \gamma_{BC} + B_1^* \mu_A + B_2^* \mu_B + B_3^* \mu_C \tag{3.21}$$

Where the A's and B's are the desired influence coefficients.

Induced velocity from a point vortex can be obtained from

$$U_x = -y\gamma/2\pi R^2$$
$$V_y = x\gamma/2\pi R^2 . \tag{3.22}$$

43

Its normal and tangential component can be calculated from

$$H_p = (U_x \vec{i} + V_y \vec{j}) \cdot \vec{n}_p \tag{3.23}$$

$$J_p + (U_x \vec{i} + V_y \vec{j}) \cdot \vec{t}_p \cdot \tag{3.24}$$

3.5 Linear Equations Sets

In the previous sections, the theory and numerical technique for the calculation of an unsteady incompressible flow field have been discussed.

In this section, a simple four element airfoil is used for illustration purposes to show the system of equations which result from the cases of steady attached flow, unsteady attached flow, and unsteady separated flow.

3.5.1 Steady Attached Flow.

Steady solutions may be obtained by forcing the initial condition to be equivalent to the steady state condition. Even though the same result can be achieved by allowing the flow to develop until the unsteady initial effects fade away, it is computationally inefficient due to the very long computing times required.

The singularity distributions and the bound circulation should remain constant with respect to time for a steady flow. Consequently, the net rate of vorticity shedding from the upper and lower surface boundary layers at the trailing edge to the wake is zero. The only vorticity in the wake is the starting vortex which is assumed to be at an infinite distance behind the airfoil. The Kelvin-Helmholtz theorem is inherently satisfied

44

in steady flows where the vorticity associated with the starting vortex is equal and opposite to the bound vorticity on the airfoil. This steady flow may be calculated simply by forcing the sum of the upper and lower surface vortex strengths (γ_1 and γ_5 in Fig. 3.5) to be zero at the trailing edge. The complete steady solution can then be obtained with a single solution of the resulting equation set.

For the case of the four element airfoil illustrated in Fig. 3.5, five unknown vortex strengths can be calculated using four surface tangency conditions at the airfoil element mid-points plus one constraint on the upper and lower surface vorticities at the trailing edge. The set of equations for a steady flow becomes

$$A_{11}\gamma_1 + \cdots + A_{15}\gamma_5 + B_{11}\mu_1 + \cdots + B_{14}\mu_4 + \vec{u}_R \cdot \vec{n}_i = 0$$

$$(i = 1,2,\ldots,4)$$

$$\gamma_1 + \gamma_5 = 0 \tag{3.25}$$

or in matrix form

$$\begin{bmatrix} A_{11} & \cdots & A_{15} \\ \cdot & & \cdot \\ \cdot & & \cdot \\ \cdot & & \cdot \\ A_{41} & \cdots & A_{45} \\ 1 & 0 \cdots 0 & 1 \end{bmatrix} \begin{Bmatrix} \gamma_1 \\ \cdot \\ \cdot \\ \cdot \\ \cdot \\ \gamma_5 \end{Bmatrix} = - \begin{bmatrix} B_{11} & \cdots & B_{14} \\ \cdot & & \cdot \\ \cdot & & \cdot \\ \cdot & & \cdot \\ B_{41} & \cdots & B_{44} \\ 0 & \cdots & 0 \end{bmatrix} \begin{Bmatrix} \mu_1 \\ \cdot \\ \cdot \\ \mu_4 \end{Bmatrix} - \begin{Bmatrix} \vec{u}_R \cdot \vec{n}_1 \\ \cdot \\ \cdot \\ u_R \cdot n_4 \\ 0 \end{Bmatrix} \tag{3.26}$$

where, A_{ij} represents the normal induced velocity coefficient on the i-th panel due to j-th vorticity strength, γ_j. The coefficient, B_{ij} is the normal induced velocity coefficient on the i-th panel control point due to
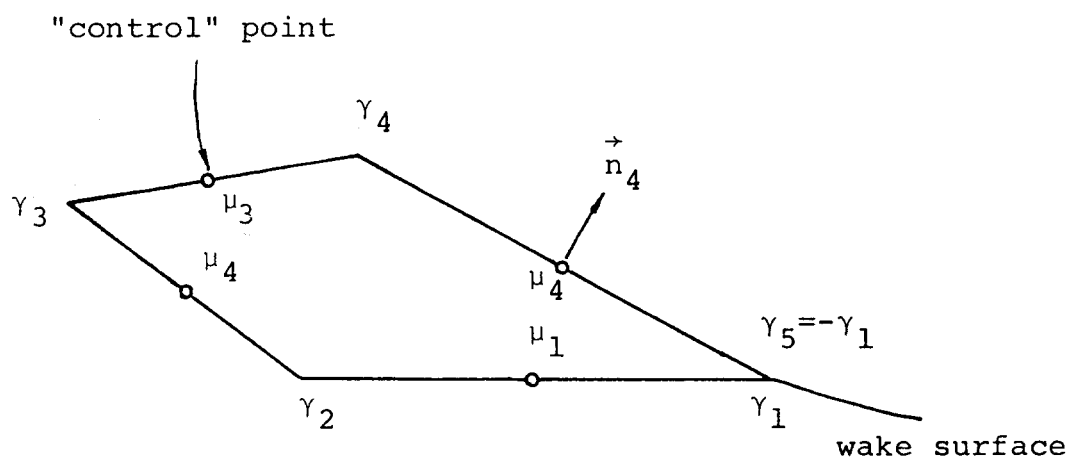
45

Figure 3.5 Vortices and Control Points on the 4 Element
          Airfoil in Steady Flow

the j-th source strength, μ_j. The product, $U_R \cdot n_i$, is the normal relative

velocity between the airfoil and freestream at the control point of the

i-th element.

3.5.2 Unsteady Attached Flow

The basic difference between the unsteady and steady flow calculation is that for the unsteady flow, the model must account for the time dependent wake geometry, motion of the airfoil, and bound circulation. At any instant, the total circulation about all singularities in the flow field should satisfy the Kelvin-Helmholtz theorem. For unsteady flows, this theorem provides an additional constraint equation which must be included in the set of system equations.

Referring to the four panel airfoil illustrated in Fig. 3.6, at the starting instant, there is no wake present and the only singularities in the flow are the source and vortex panels distributed over the airfoil surface. The boundary conditions or system constraints for this situation are the four surface tangency conditions and the Kelvin-Helmholtz theorem. The system equations for the four element airfoil become

$$A_{i1}\gamma_1 + \cdots + A_{i5}\gamma_5 + B_{i1}\mu_1 + \cdots + B_{i4}\mu_4 + \vec{u}_R + \vec{n}_i = 0$$

$$(i = 1,2,\ldots,4)$$

$$\frac{1}{2} S_1(\gamma_1 + \gamma_2) + \cdots + \frac{1}{2} S_4(\gamma_4 + \gamma_5) = 0$$

(3.27)

or in matrix form

$$
\begin{bmatrix}
A_{11} & \cdots & A_{15} \\
\cdot & & \cdot \\
\cdot & & \cdot \\
\cdot & & \cdot \\
A_{41} & & A_{45} \\
\frac{1}{2}S_1 & \cdots & \frac{1}{2}S_4
\end{bmatrix}
\begin{Bmatrix}
\gamma_1 \\
\cdot \\
\cdot \\
\cdot \\
\gamma_5
\end{Bmatrix}
= -
\begin{bmatrix}
B_{11} & \cdots & B_{14} \\
\cdot & & \cdot \\
\cdot & & \cdot \\
\cdot & & \cdot \\
B_{41} & & B_{44} \\
0 & \cdots & 0
\end{bmatrix}
\begin{Bmatrix}
\mu_1 \\
\cdot \\
\cdot \\
\cdot \\
\mu_4
\end{Bmatrix}
-
\begin{Bmatrix}
\vec{u}_R \cdot \vec{n}_1 \\
\cdot \\
\cdot \\
\cdot \\
\vec{u}_R \cdot \vec{n}_4 \\
0
\end{Bmatrix}
$$
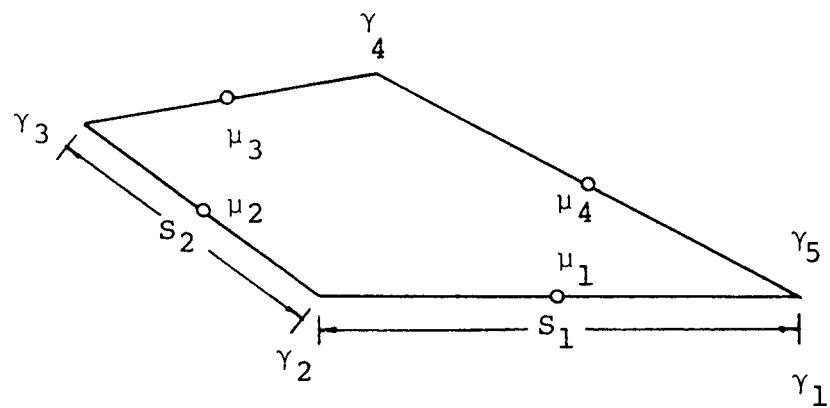
Figure 3.6   Vortices and Control Points on the 4 Element
             Airfoil at the Starting Instant

49

where, A_{ij} and B_{ij} are the source and vortex influence coefficients and S_j is the length of the j-th panel.

After the starting instant, a wake surface will be generated from the trailing edge as illustrated in Fig. 3.7. At any instant thereafter, the rate of vorticity shedding to the trailing edge wake is equal to the vorticity flux from the boundary layers or equivalently, to the instantaneous sum of the upper and lower surface vortex strengths at the trailing edge. Therefore, the vorticity distribution on the nascent wake element at the trailing edge reflects the history of the vortex strength that has been shed to the wake element from the trailing edge of an airfoil during a single time step.

The instantaneous rate of vorticity injection to the wake may be expressed as

$$\frac{d\Gamma_W}{dt} = (\frac{U_u + U_\ell}{2})\ (\gamma_1 + \gamma_5)\ . \tag{3.29}$$

The circulation that is contained in the nascent wake element may then be expressed in terms of an integration of the vorticity injection rate over the time dt. This may be written as

$$\gamma_1^W = \int_t^{t+dt} \frac{d\Gamma_W}{dt}\ dt = \int_t^{t+dt} (\frac{U_u + U_\ell}{2})\ (\gamma_1 + \gamma_5)dt\ . \tag{3.30}$$

In Fig. 3.8, the corresponding variation of vorticity on the nascent wake element at the trailing edge of a flat plate is illustrated. An equivalent linear vorticity distribution on the nascent element is obtained by
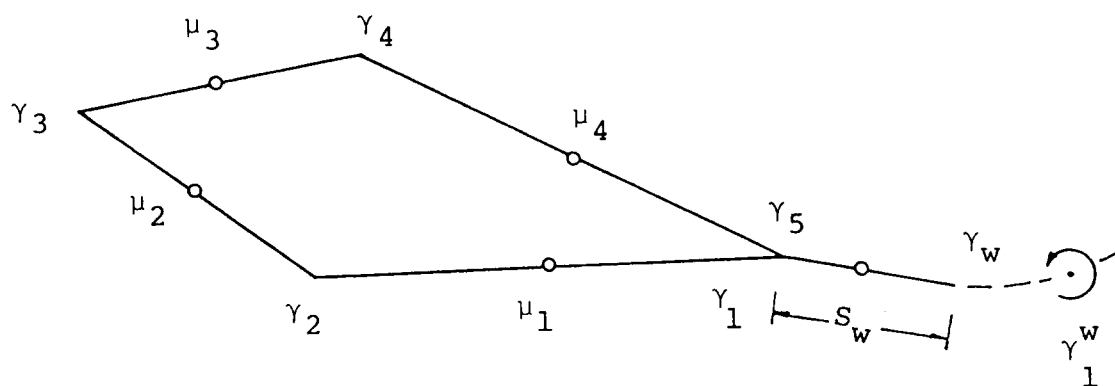
Figure 3.7   Vortices and Control Points on the 4 Element
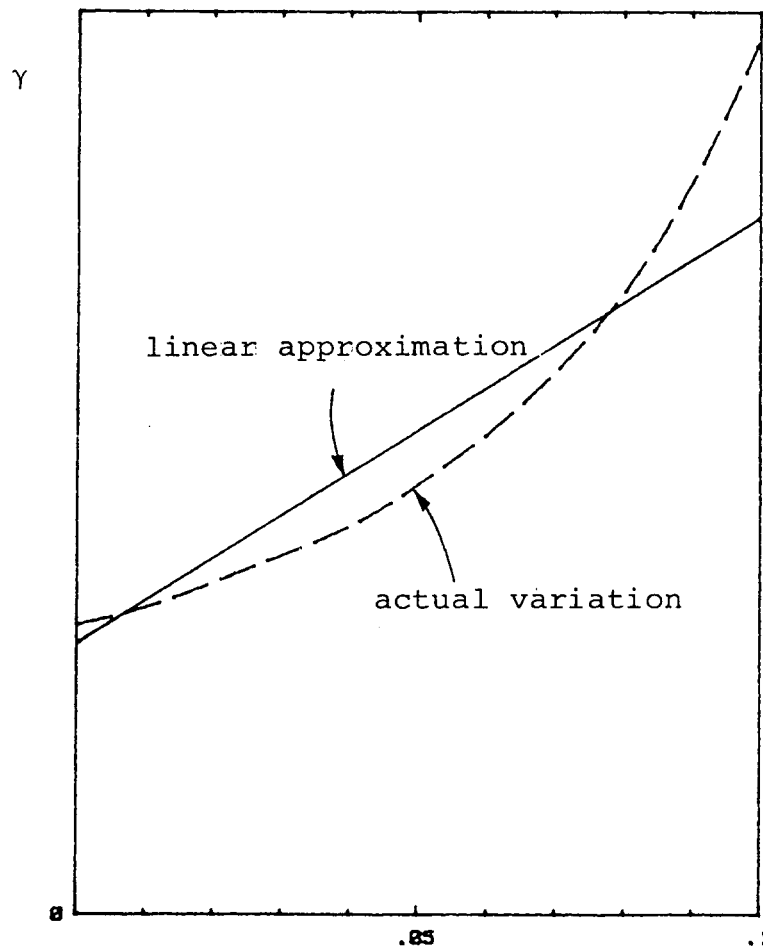Airfoil in Unsteady Attached Flow

Figure 3.8   Vortex Strength Distribution At the Trailing
             Edge Wake Element

matching the induced velocity on the trailing edge control points which would be produced by the exact distribution. This yields

$$\gamma_1^w = \left(\frac{U_u + U_\ell}{2}\right)_t \ dt\left[\ \frac{1}{2}\left\{(\gamma_1 + \gamma_5)_{t+dt} + \gamma_{6_{t+dt}}\right\}\right].$$ (3.31)

It should be noted that the vortex strength at both ends of the nascent wake element are fully coupled into the system equations. This allows the complete solution to include the correct instantaneous effect of the nascent wake element. On the basis of the discussions above, the current investigation uses the Eq. 3.31 which leads to one additional unknown, γ_w (see Fig. 3.7).

With an additional unknown vortex strength, γ_w, one more constraint is needed for a unique solution. For that additional equation, the Kutta condition is applied by putting an additional control point on the nascent trailing edge element (see Fig. 3.7). At that point, the local convection velocity is required to be tangent to the wake element or the trailing edge bisector. The resulting set of system equations for the four element airfoil will have six equations and six unknowns:

$$A_{11}\gamma_1 + \cdots + A_{15}\gamma_5 + A_{1w}\gamma_w + B_{11}\mu_1 + \cdots + B_{14}\mu_4 + A_{11}^4\gamma_1^w + \cdots$$

$$\cdots + \vec{u}_R \cdot \vec{n}_i = 0 \ (i = 1,2,\ldots,4)$$ (3.32)

$$A_{w1}\gamma_1 + \cdots + A_{w5}\gamma_5 + A_{ww}\gamma_w + B_{w1}\mu_1 \cdots + B_{w4}\mu_4 + A_{w1}^w\gamma_1^w + \cdots$$

$$\cdots + \vec{U}_R \cdot \vec{n}_w = 0$$

$$\frac{1}{2} S_1(\gamma_1 + \gamma_2) + \cdots + \frac{1}{2} S_4(\gamma_4 + \gamma_5) + \frac{1}{2} S_w(\gamma_1 + \gamma_5 + \gamma_w) + \cdots$$

$$\cdots + \gamma_1^w + \cdots = 0$$

53

or in matrix form

$$
\begin{bmatrix}
A_{11} & \cdots & A_{15} A_{1w} \\
\cdot & & \cdot \\
\cdot & & \cdot \\
\cdot & & \cdot \\
A_{51} & \cdots & A_{55} A_{1w} \\
A_{w1} & \cdots & A_{w5} A_{ww} \\
\frac{1}{2}(S_1 + S_w) & \cdots & \frac{1}{2}S_w
\end{bmatrix}
\begin{Bmatrix}
\gamma_1 \\
\cdot \\
\cdot \\
\cdot \\
\gamma_5 \\
\gamma_w
\end{Bmatrix}
= -
\begin{bmatrix}
B_{11} & \cdots & B_{14} \\
\cdot & & \cdot \\
\cdot & & \cdot \\
B_{41} & \cdots & B_{44} \\
B_{w1} & \cdots & B_{w4} \\
0 & \cdots & 0
\end{bmatrix}
\begin{Bmatrix}
\mu_1 \\
\cdot \\
\cdot \\
\mu_4
\end{Bmatrix}
-
$$

$$
-
\begin{bmatrix}
\vec{u}_R \cdot \vec{n}_1 \\
\cdot \\
\cdot \\
\vec{u}_R \cdot \vec{n}_4 \\
u_R \cdot n_w \\
0
\end{bmatrix}
- \gamma_1^w
\begin{bmatrix}
A_{11}^w \\
\cdot \\
\cdot \\
A_{51}^w \\
A_{w1}^w
\end{bmatrix}
- \gamma_2^w
\begin{bmatrix}
A_{12}^w \\
\cdot \\
\cdot \\
A_{52}^w \\
A_{w2}^w
\end{bmatrix}
- \cdots
\tag{3.33}
$$

where the subscript w indicates terms involving the nascent wake element. The last matrix product represents the downwash due to the wake other than the nascent vortex where the number of wake elements is a function of time, $N(t)$.

3.5.3 Unsteady Separated Flow

When the boundary layer separates, a second wake surface will be introduced in the flow at the separation point as shown in Fig. 3.9. For the present study, the nascent vortex for the separation wake surface is represented as a lumped vortex whose strength is related to the local vorticity in the boundary layer as described in Section 2.3.

The rationale for the introduction of vorticity at the boundary layer separation point is similar to that followed at the trailing edge. The nascent vortex represents the vorticity shed during a time step. This is calculated as

$$\gamma_S = \int_t^{t+\Delta t} \frac{d\Gamma_S}{dt} \, dt = \int_t^{t+\Delta t} \frac{U_S^2}{2} \, dt$$

$$= \frac{1}{2} U_S^2 \bigg|_t \Delta t$$

As is the case at the trailing edge, a direction of shedding must be assumed. After extensive computational experiments, it was determined that a shedding angle of 10° above the local surface tangent yields calculated lift and drag coefficients in best agreement with experimental results. This value for the shedding angle was utilized for the results presented in Chapter IV.
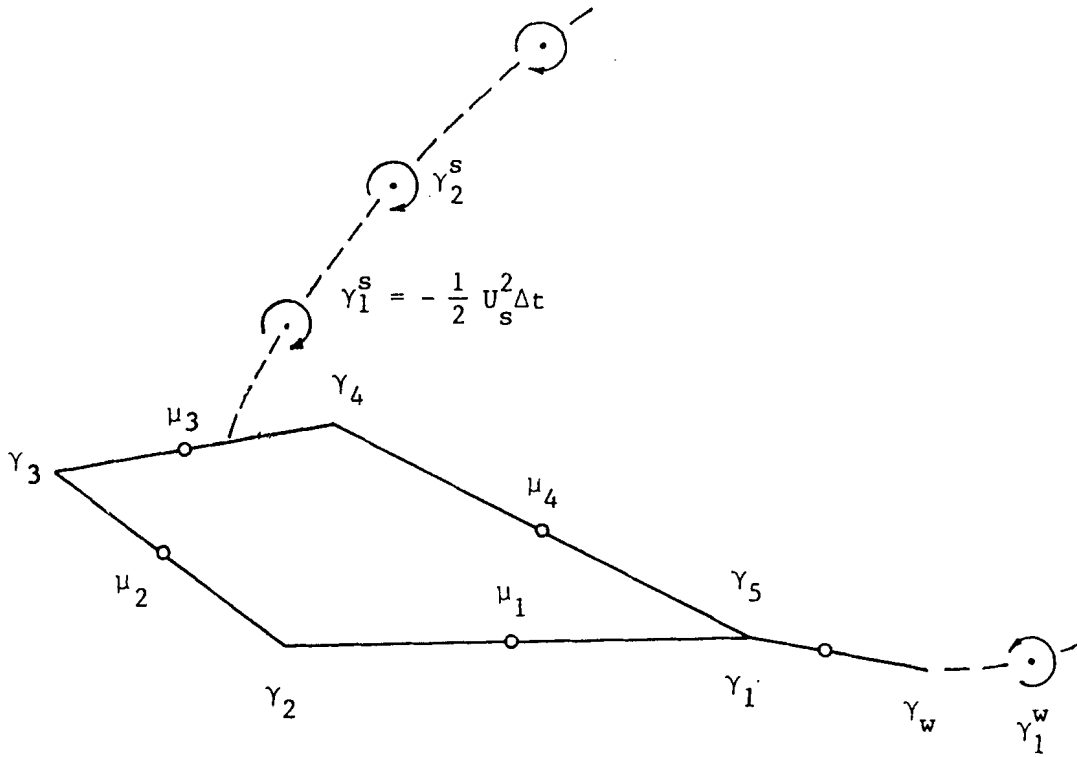
55

Figure 3.9   Vortices and Control Points on the 4 Element
Airfoil in Separated Flow

56

The presence of a separated wake surface adds several terms to the system equations which become

$$A_{i1}\gamma_1 + \ldots + A_{i5}\gamma_5 + A_{iw}\gamma_w + B_{i1}\mu_1 + \ldots + B_{i4}\mu_4 + {}^{W}A_{i1}^{w}\gamma_1 + \ldots$$

$$\ldots + A_{i1}^{s}\gamma_1^{s} + \ldots + \vec{u}_R \cdot \vec{n}_i = 0 \qquad (i = 1,2,\ldots,4)$$

$$A_{w1}\gamma_1 + \ldots + A_{w5}\gamma_5 + A_{ww}\gamma_w + B_{w1}\mu_1 + B_{w4}\mu_4 + A_{w1}^{w}\gamma_1^{w} + \ldots$$

$$\tag{3.34}$$

$$+ A_{w1}^{s}\gamma_1^{s} + \ldots + \vec{U}_R \cdot \vec{n}_w = 0$$

$$\frac{1}{2} S_1(\gamma_1 + \gamma_2) + \ldots + \frac{1}{2} S_4(\gamma_4 + \gamma_5) + \frac{1}{2} S_w(\gamma_1 + \gamma_5 + \gamma_w) + \ldots$$

$$\ldots + \gamma_1^{w} + \ldots - \frac{1}{2} U_s^2 \Delta t + \gamma_2^{s} + \ldots = 0$$

or in matrix form

$$
\begin{bmatrix}
A_{11} & \cdots & A_{15} & A_{1w} \\
\vdots & & & \\
\vdots & & & \\
A_{51} & \cdots & A_{55} & A_{5w} \\
A_{w1} & \cdots & A_{w5} & A_{ww} \\
\frac{1}{2}(S_1+S_w) & \cdots & & \frac{1}{2}S_w
\end{bmatrix}
\begin{Bmatrix}
\gamma_1 \\ \vdots \\ \vdots \\ \vdots \\ \gamma_5 \\ \gamma_w
\end{Bmatrix}
= -
\begin{bmatrix}
B_{11} & \cdots & B_{14} \\
\vdots & & \\
\vdots & & \\
B_{41} & \cdots & B_{44} \\
B_{w1} & \cdots & B_{w4} \\
0 & \cdots & 0
\end{bmatrix}
\begin{Bmatrix}
\mu_1 \\ \vdots \\ \vdots \\ \mu_4
\end{Bmatrix}
\tag{3.35}
$$

$$
-
\begin{Bmatrix}
\vec{u}_R \cdot \vec{n}_1 \\ \vdots \\ \vdots \\ \vdots \\ \vec{u}_R \cdot \vec{n}_4 \\ \vec{u}_R \cdot \vec{n}_w \\ 0
\end{Bmatrix}
- \gamma_1^{w}
\begin{bmatrix}
A_{11}^{w} \\ \cdot \\ \cdot \\ \cdot \\ A_{51}^{w} \\ A_{w1}^{w}
\end{bmatrix}
- \ldots + \frac{1}{2}U_s^2 \Delta t
\begin{Bmatrix}
A_{11}^{s} \\ \cdot \\ \cdot \\ \cdot \\ A_{51}^{s} \\ A_{w1}^{s}
\end{Bmatrix}
- \gamma_2^{s}
\begin{bmatrix}
A_{12}^{s} \\ \cdot \\ \cdot \\ \cdot \\ A_{52}^{s} \\ A_{w2}^{s}
\end{bmatrix}
- \ldots = 0
$$

where u_R represents the separating edge velocity obtained at the previous time step and superscript s indicates relations involving the separating wake.

3.6 Calculation of Airloads

The pressure at any point in an irrotational, ideal flow may be found with the unsteady Bernoulli equation,

$$P = P_\infty - \rho \left[\frac{\partial \Phi}{\partial t} + \frac{1}{2} (\nabla \Phi)^2 \right] . \qquad (3.36)$$

As shown by Summa (Ref. 52, Appendix B), this may be rewritten in body fixed coordinates as

$$P = P_\infty - \rho \left[\frac{\partial \phi}{\partial t} + (\vec{U}_\infty - \vec{U}_B - \vec{\omega}_B \times \vec{r}) \cdot \nabla \phi + \frac{1}{2} (\nabla \phi)^2 \right] . \qquad (3.37)$$

The primary difference between Eqs. 3.36 and 3.37 is the additional increment to $\partial \phi / \partial t$ on the airfoil due to the motion of the airfoil through the potential field. The significance of this term may be appreciated by recognizing that even if the potential field is steady, $\partial \phi / \partial t$ for a point moving through the field is not equal to zero unless the potential field is also uniform.

Eq. 3.37 may be rewritten in a more convenient form for numerical computation by expressing $\nabla \phi$ as

$$\nabla \phi = \nabla_S \phi + \frac{\partial \phi}{\partial n} \vec{e}_n \qquad (3.38)$$

where ∇_S is the surface gradient. In Section 2.2, the surface tangency condition was written in body fixed coordinates as

$$\frac{\partial \phi}{\partial n} = - (\vec{U}_\infty - \vec{U}_B - \vec{\omega}_B \times \vec{r}) \cdot \vec{n} . \qquad (3.39)$$

58

With Eq. 3.37, Eq. 3.38 may be expanded to yield

$$P = P_\infty - \rho \left[\frac{\partial \Phi}{\partial t} + (\vec{U}_\infty - \vec{U}_B - \vec{\omega}_B \times \vec{r}) \cdot \nabla_S \phi \right.$$

$$\left. + \frac{\partial \Phi}{\partial n} (\vec{U}_\infty - \vec{U}_B - \vec{\omega}_B \times \vec{r}) \cdot \vec{n} + \frac{1}{2} (\nabla_S \phi)^2 + \frac{1}{2} (\frac{\partial \Phi}{\partial n})^2 \right] . \qquad (3.40)$$

Substituting Eq. 3.39 into Eq. 3.40 leads to

$$P = P_\infty - \rho \left[\frac{\partial \Phi}{\partial t} + (\vec{U}_\infty - \vec{U}_B - \vec{\omega}_B \times \vec{r}) \cdot \nabla_S \phi \right.$$

$$\left. - \frac{1}{2} \{(\vec{U}_\infty - \vec{U}_B - \vec{\omega}_B \times \vec{r}) \cdot \vec{n}\}^2 + \frac{1}{2} (\nabla_S \phi)^2 \right] . \qquad (3.41)$$

Pressure calculations utilizing Eq. 3.41 require the direct evaluation of the surface potential distribution in order to calculate $\partial \Phi / \partial t$. A number of complications arose in the present study due to the multivaluedness of the potential induced by a point vortex and the necessity of defining a reference line for angle measurements, i.e., for a point vortex, the induced potential is

$$\phi = \gamma \theta / 2\pi .$$

The problem of multi-valued induced potentials may be circumvented by evaluating the pressure distribution in terms of induced tangential velocity. For this purpose the surface gradient of the pressure distribution may be written as

$$\frac{\partial C_P}{\partial s} = - \frac{2}{U_\infty^2} \left[\frac{\partial}{\partial t} (\nabla_S \phi) \right] - \frac{2}{U_\infty^2} \frac{\partial}{\partial s} \left[(\vec{U}_\infty - \vec{U}_B - \vec{\omega}_B \times \vec{r}) \cdot \nabla_S \phi \right.$$

$$\left. - \frac{1}{2} \{(\vec{U}_\infty - \vec{U}_B - \vec{\omega}_B \times \vec{r}) \cdot \vec{n}\}^2 + \frac{1}{2} (\nabla_S \phi)^2 \right] \qquad (3.42)$$

59

where $C_p = (P - P_\infty)/(\frac{1}{2} \rho U_\infty^2)$ the pressure coefficient.

The pressure coefficient at any point on the surface may be obtained by integrating $\partial C_p/\partial S$ along the surface from the stagnation point where the pressure coefficient is known, i.e.,

$$C_p = \int_{stag}^{s} \frac{\partial C_p}{\partial S} \, dS + 1 \; .$$

(3.43)

With Eq. 3.43, the airloads on the airfoil may be calculated by integrating the pressure force vector components over the entire surface of the airfoil.

CHAPTER IV

RESULTS

This chapter contains the calculation results for the current model, ADAM2 (Advanced Dynamic Airfoil Model in 2 dimensions). The capabilities of ADAM2 are illustrated for three different flow conditions: steady attached flow, unsteady attached flow, and unsteady separated flow. The calculated results are compared with experimental data and analytical solutions where available. Areas of significant improvements over the previous model, USTAR2, are also indicated.

4.1 Steady Flow Calculations

Figs. 4.1 through 4.8 illustrate the capability of ADAM2 to predict the pressure distribution on different types of two-dimensional airfoils in steady flow without boundary layer separation. The calculation results presented are for the cases of a circular cylinder and typical laminar and turbulent airfoils. The superiority of ADAM2 over USTAR2 is clearly shown through several comparisons.

The case of a circular cylinder with different numbers of elements is presented in Figs. 4.1 through 4.3 in which the surface pressure coefficient is plotted as a function of azimuthal angle around the cylinder. Surface panel placement is not a particularly critical factor in the use of ADAM2. The general rules to follow are to vary the element size in proportion to the local radius of curvature of the airfoil surface and that no element should be less than 50% of the size of the adjacent elements. For
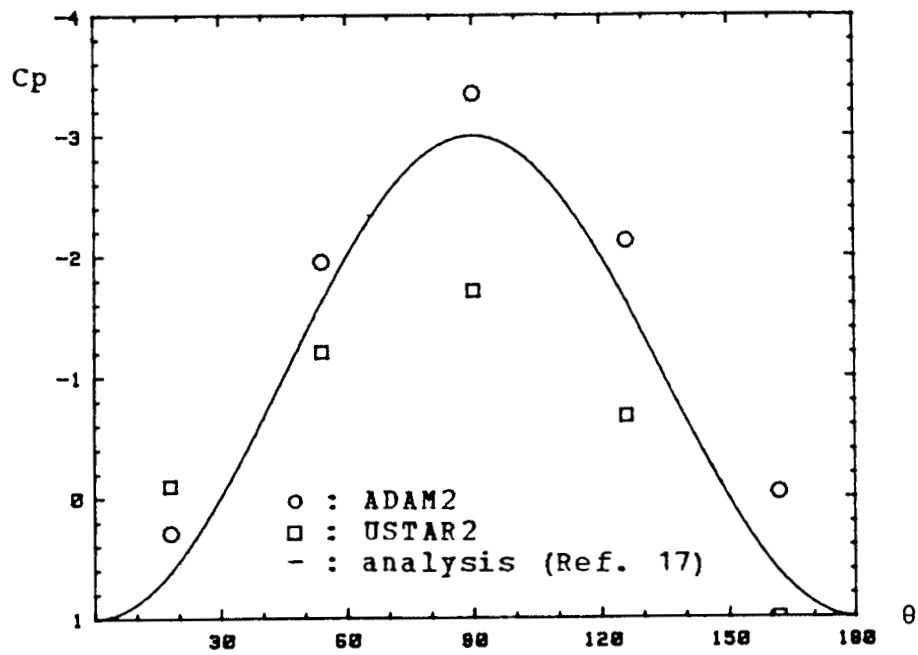
Figure 4.1   Steady Pressure Distribution On
             a 10 Element Circular Cylinder

62
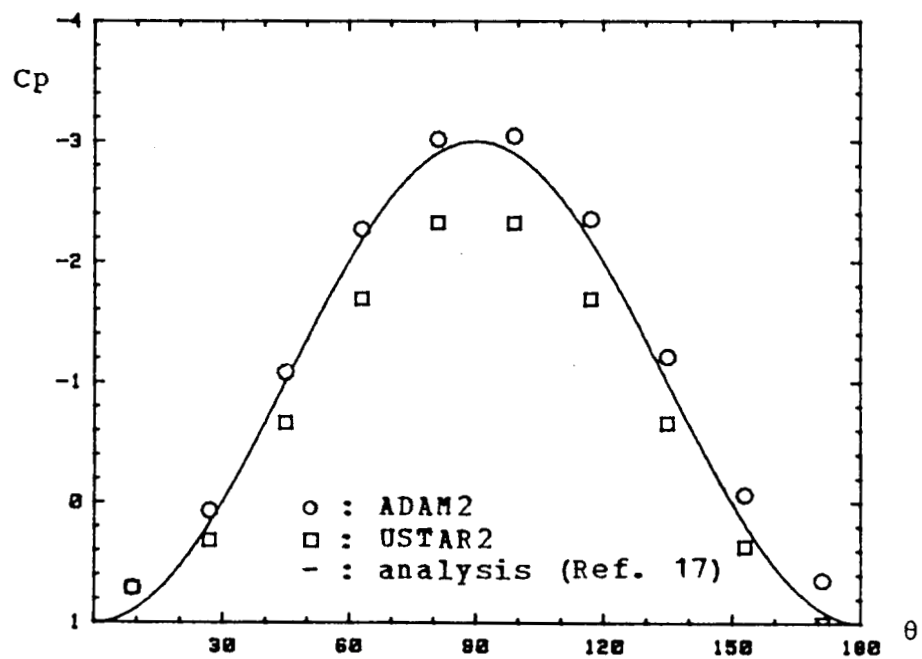
Figure 4.2   Steady Pressure Distribution On
a 20 Element Circular Cylinder
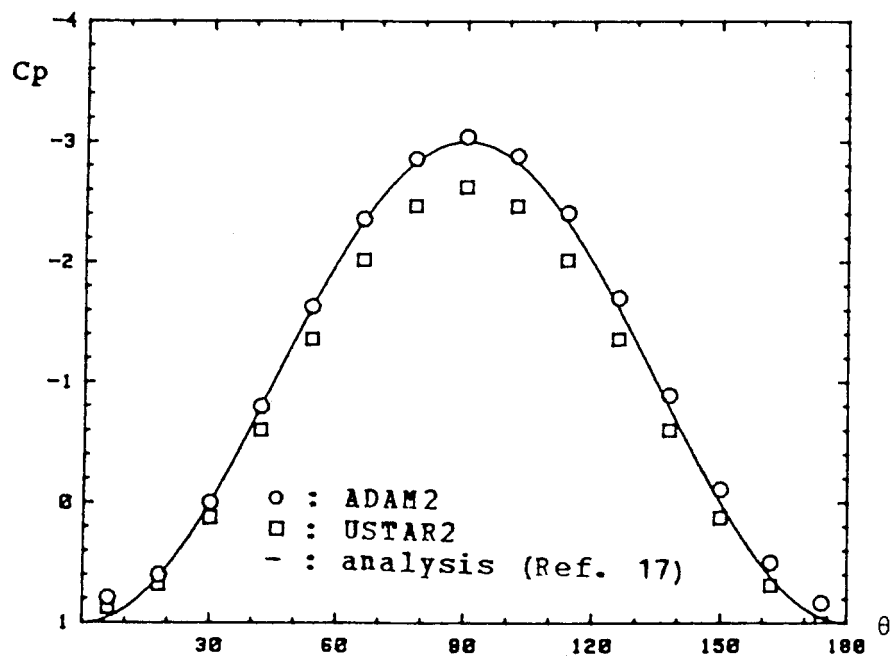
Figure 4.3 Steady Pressure Distribution On
a 30 Element Circular Cylinder
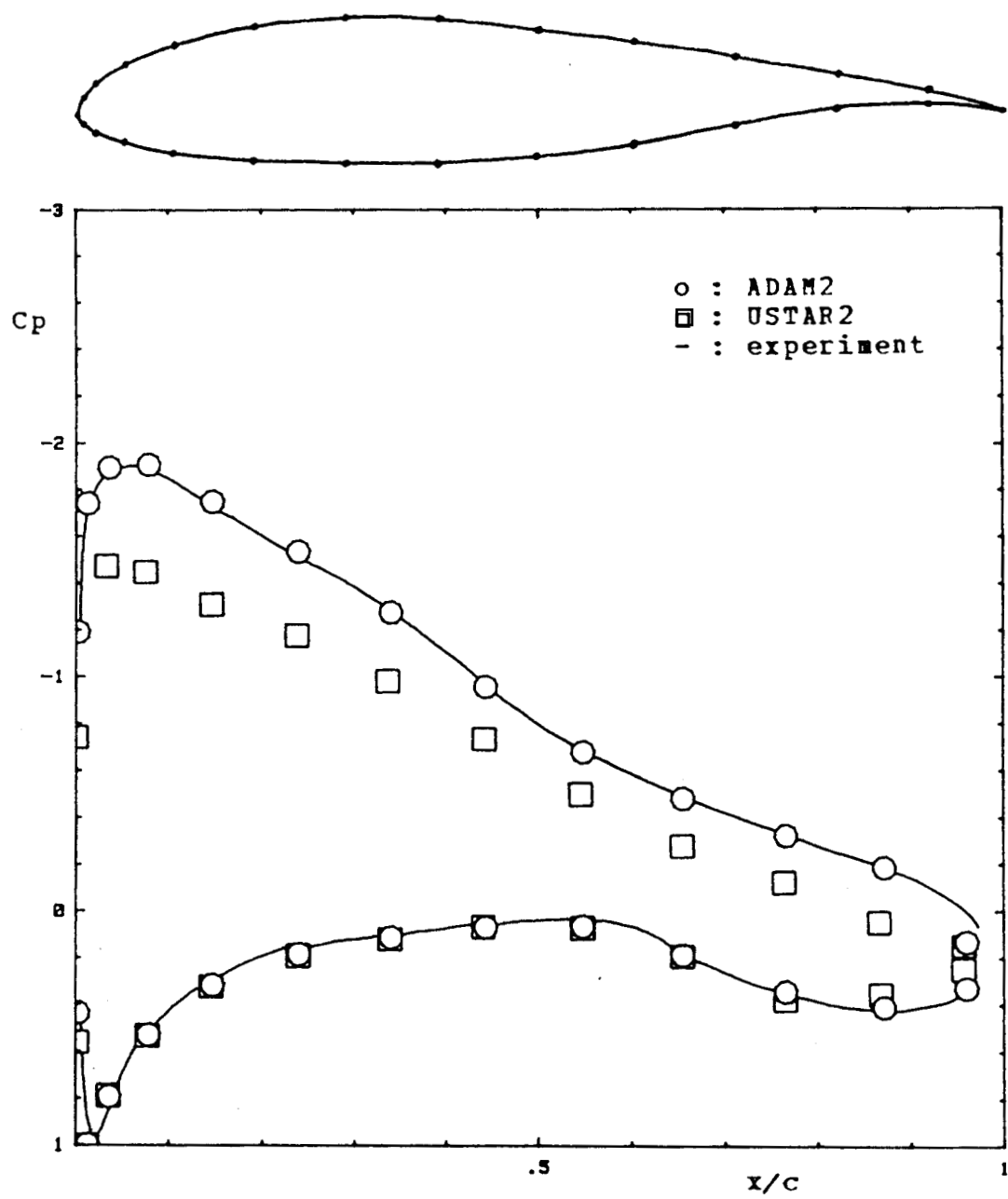
Figure 4.4   Steady Pressure Distribution On an NLF(1)-0416
Airfoil at 6.1° Angle of Attack
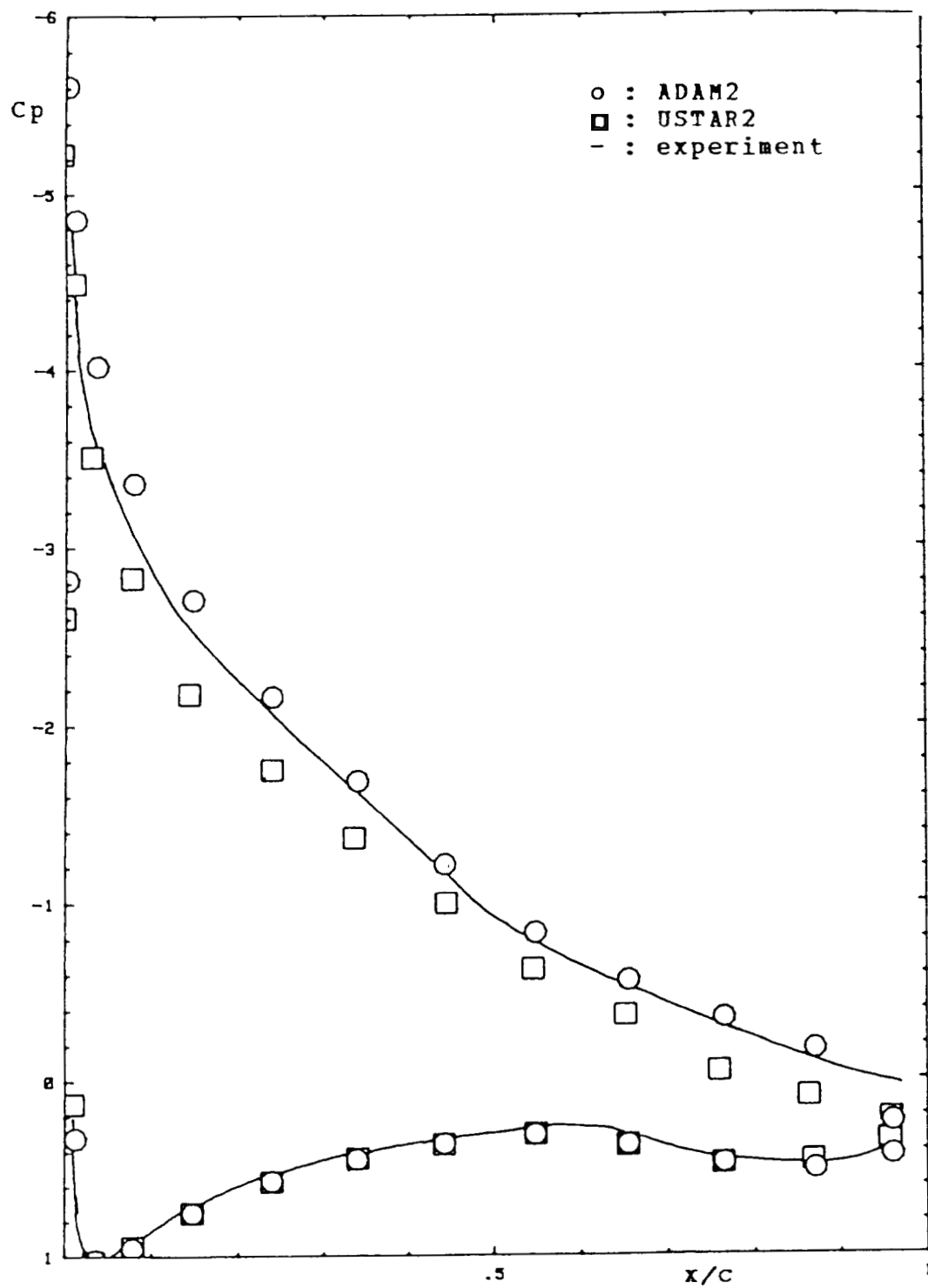
Figure 4.5 Steady Pressure Distribution On an NLF(1)-0416
Airfoil at 12.21° Angle of Attack
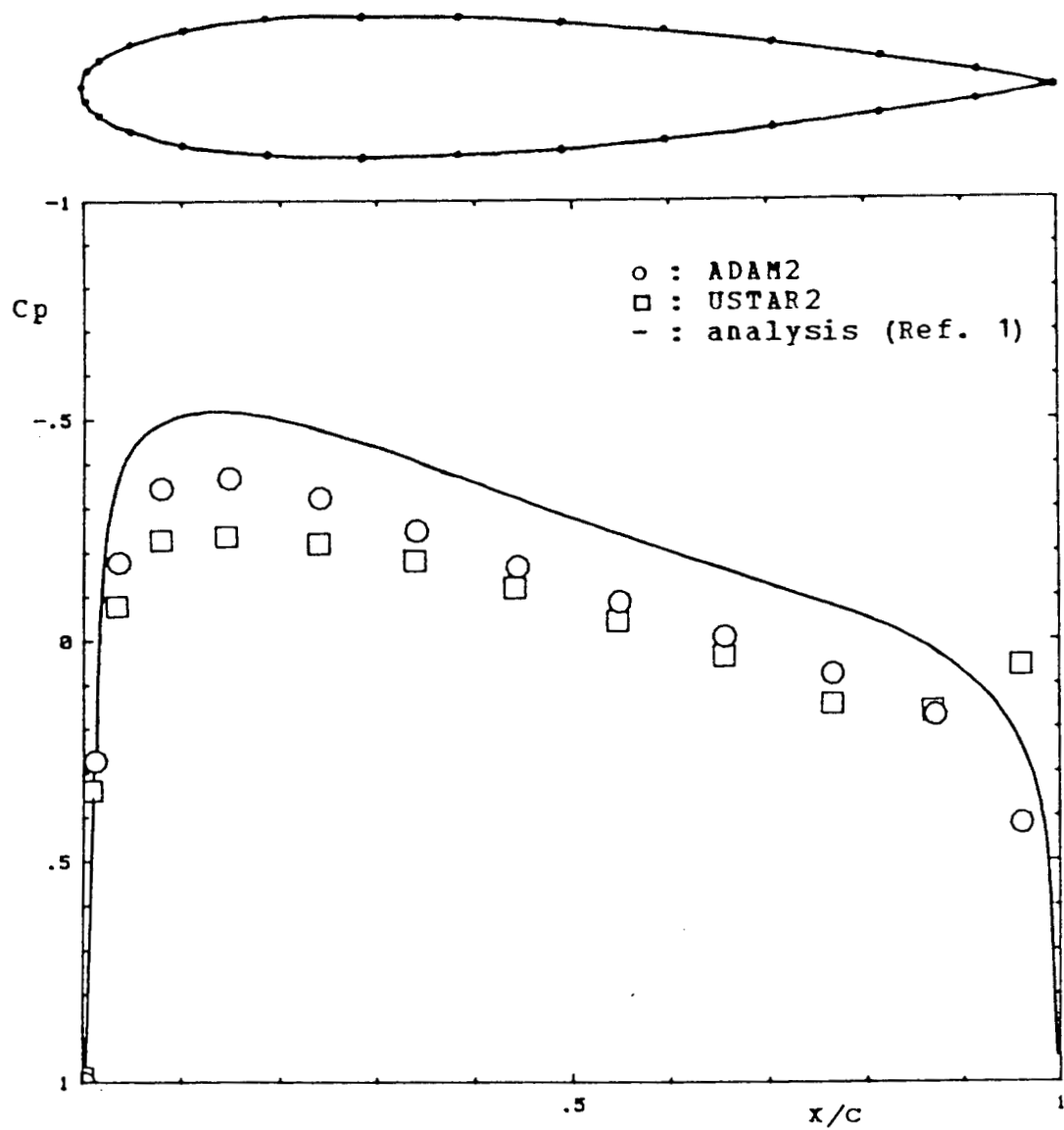
Figure 4.6 Steady Pressure Distribution on a NACA 0015
Airfoil at 0° Angle of Attack (26 element)
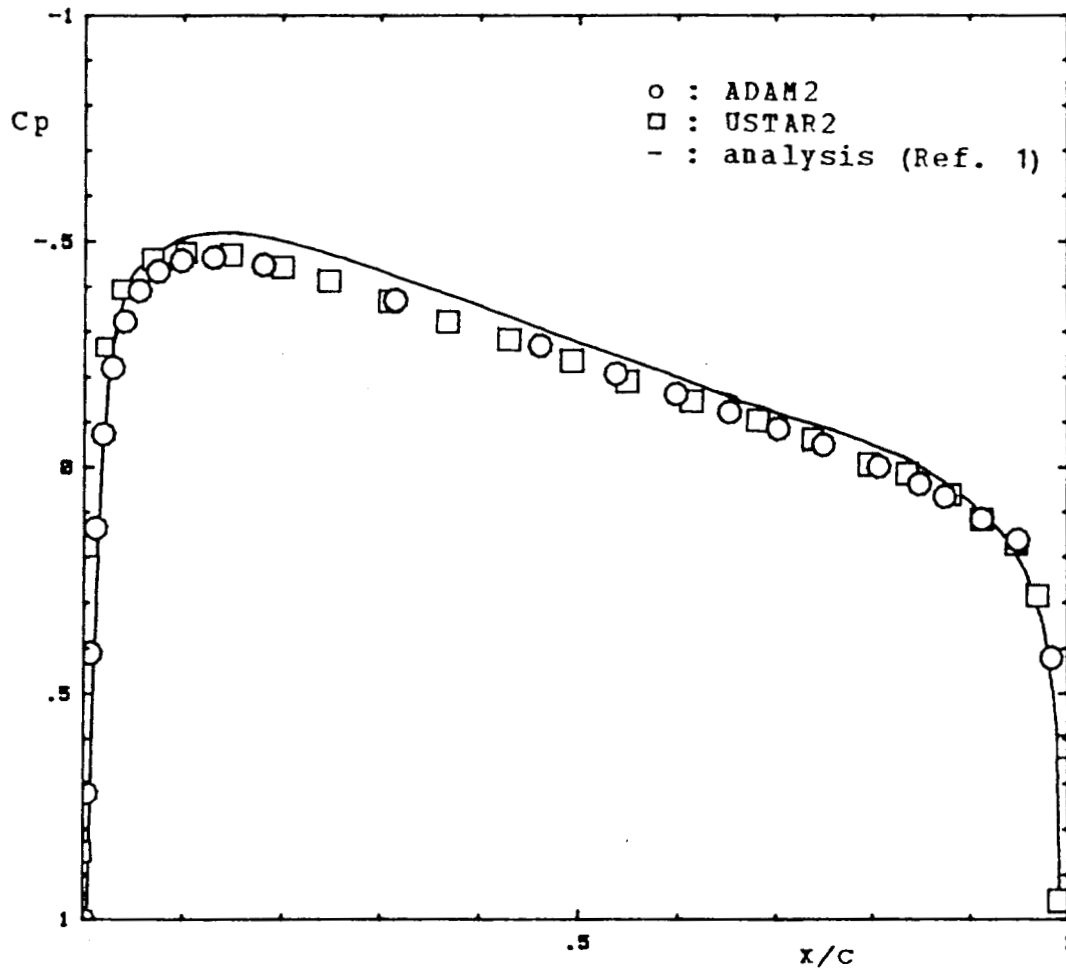
Figure 4.7 Steady Pressure Distribution on a NACA 0015
Airfoil at 0° Angle of Attack (50 element)
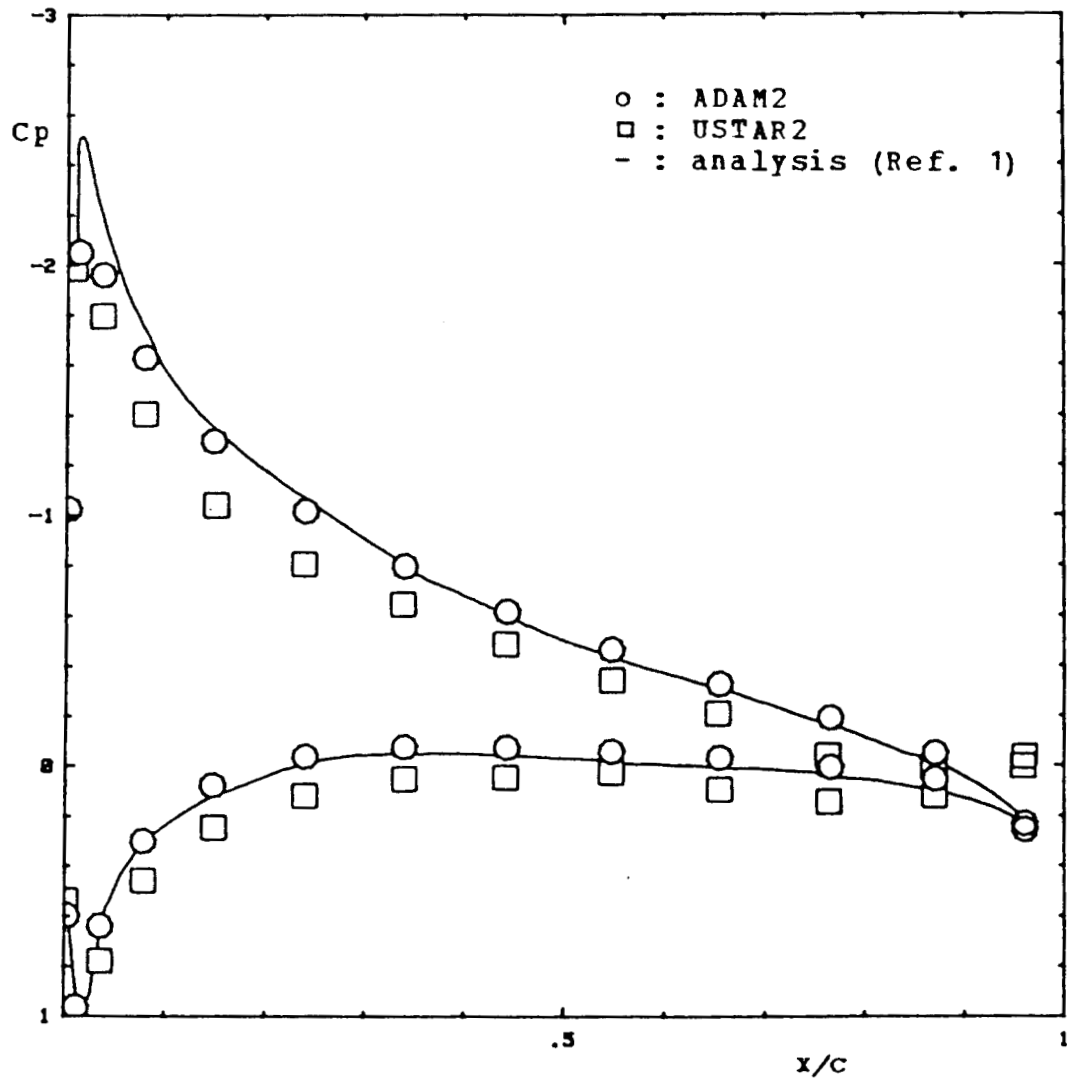
Figure 4.8   Steady Pressure Distribution on a NACA 0015
Airfoil at 6° Angle of Attack

the case of a cylinder with a uniform radius of curvature, it is sufficient to simply choose equally sized elements.

Although ADAM2 and USTAR2 will both converge to the exact solution as the number of elements is increased, it is apparent from the figures that the rate of convergence of ADAM2 is more rapid.

Figs. 4.4 and 4.5 illustrate the calculated chordwise pressure coefficient distribution for a laminar airfoil at two angles of attack, 6.1° and 12.21°. Similar results from USTAR2 and experimental data are also plotted for comparison. Laminar airfoils present unique computational difficulties since they typically have sharp leading edges and locally concave surfaces. It may be noted from the figures that the calculated pressure distribution closely follows the experimental data. The slight discrepancy on the suction side of the airfoil at the higher angle of attack may be reduced through the use of denser element spacing around the nose.

Typical calculations of chordwise pressure distribution for turbulent airfoils are presented in Figs. 4.6 through 4.8 at 0° and 6° angle of attack. Again, the improved accuracy of ADAM2 is noted.

USTAR2 (see Ref. 20), the predecessor to ADAM2, utilized a single control point on the trailing edge bisector to represent the combination of surface tangency conditions on the upper and lower surface at the trailing edge and the Kutta condition. With ADAM2, the trailing edge is more completely modeled by including separate surface tangency conditions on the upper and lower surface and a separate Kutta condition enforced on the nascent wake panel. The benefits of the improved trailing edge modeling are apparent in Figs. 4.6 through 4.8, particularly with coarser surface paneling.

70

4.2 Unsteady Attached Flow

Figs. 4.9 through 4.11 are typical of calculations of chordwise poten-
tial jump distribution for non-separated flow over an impulsively started
flat plate. Although cases of impulsively started airfoils with thickness
may be predicted as well, there are no corresponding experimental or ana-
lytical results for comparison. Fig. 4.9 presents a comparison between the
computed and exact potential jump distribution over an impulsively started
flat plate at the starting instant. The improved convergence charac-
teristics of ADAM2 are noted for unsteady flows as well as for the previous
steady flow results.

Figs. 4.10 and 4.11 illustrate the subsequent development of cir-
culation and lift with respect to time for the flat plate airfoil.
Wagner's (Ref. 21) analytical results are also plotted for comparison.

4.3 Unsteady Separated Flow

Figs. 4.12 through 4.14 illustrate the comparison between computed and
experimentally determined lift coefficient versus angle of attack for a
NACA 0015 airfoil at three different Reynolds numbers. In all cases, the
airfoil is impulsively set into motion and maintained at a constant angle
of attack. For these cases, the calculations have been continued for 20
chord lengths of travel, with the lift arithmetically averaged over that
interval.

It is observed that the boundary layer separation point obtained from
the boundary layer calculations, starts from the trailing edge and
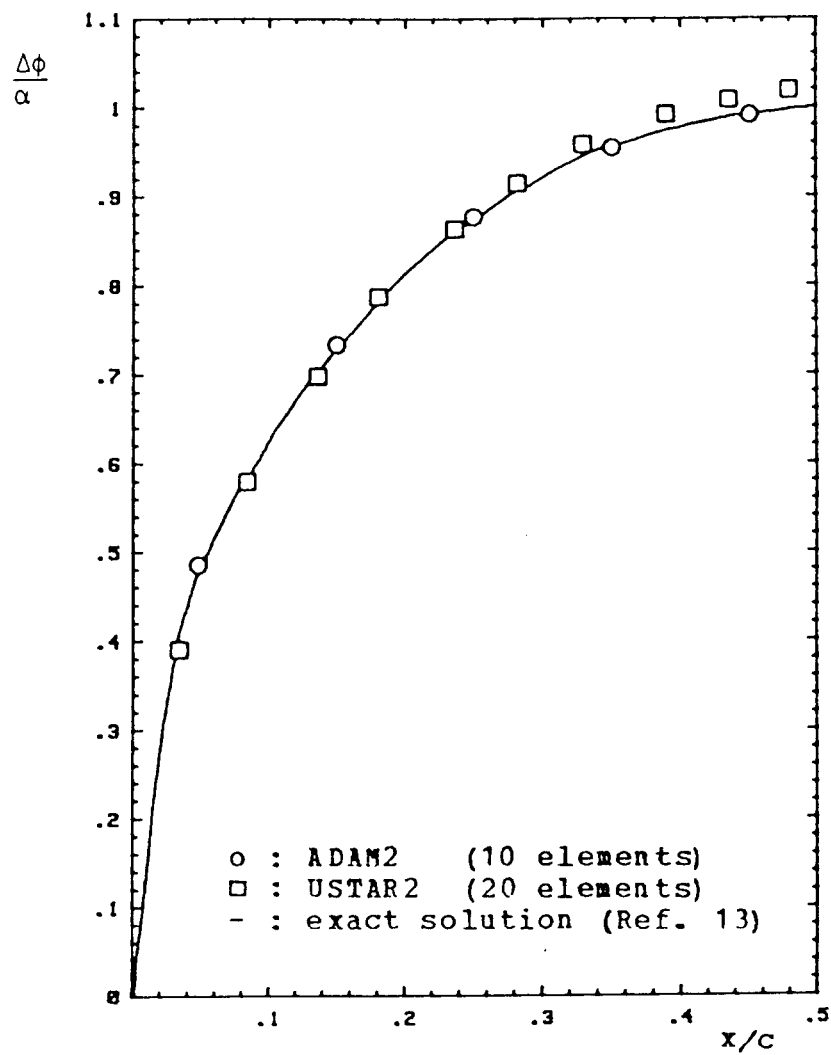
Figure 4.9   Potential Jump Distribution on an Impulsively
              Started Flat Plate Airfoil
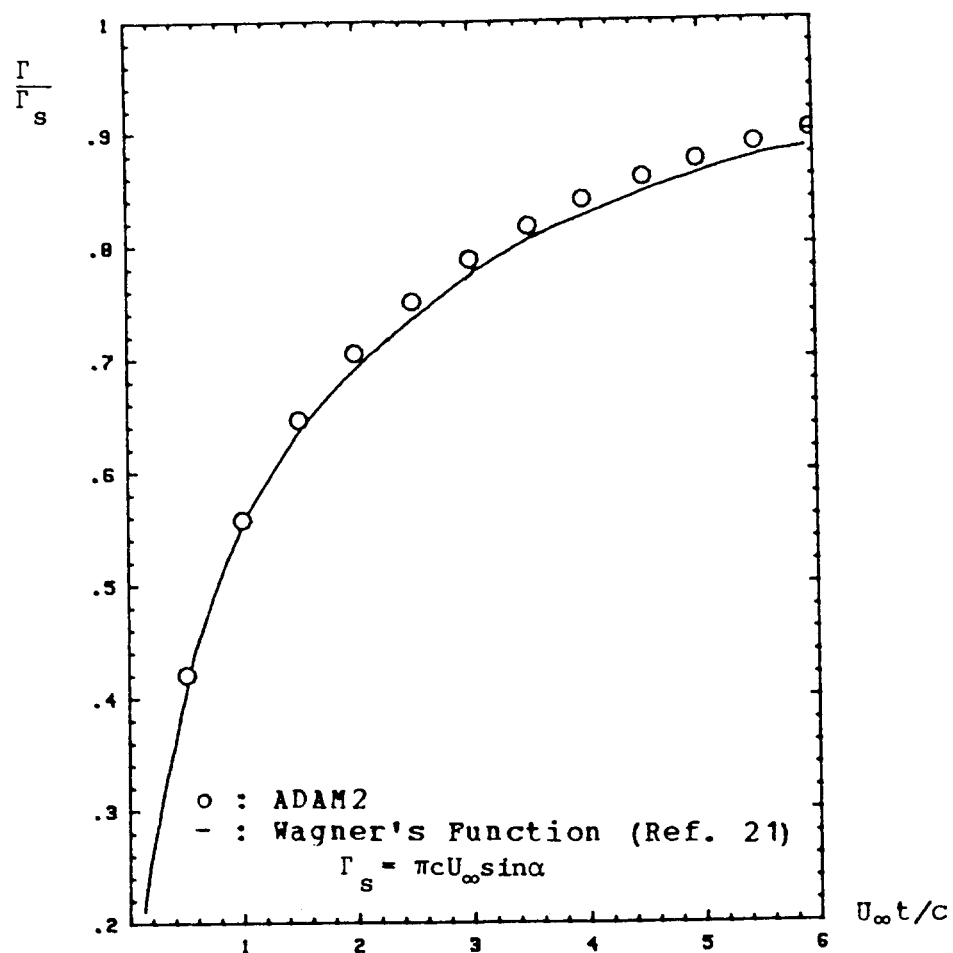
Figure 4.10   Indicial Circulation on an Impulsively Started
              Flat Plate Airfoil

$$\phi^* = \frac{C_\ell}{2\pi\alpha}$$

o : ADAM2

— : Wagner's Function (Ref. 21)

$$\phi^* = 1 - .165e^{-.455s} - .335e^{-.3s}$$

where, $s = 2U_\infty t/c$

$U_\infty t/c$
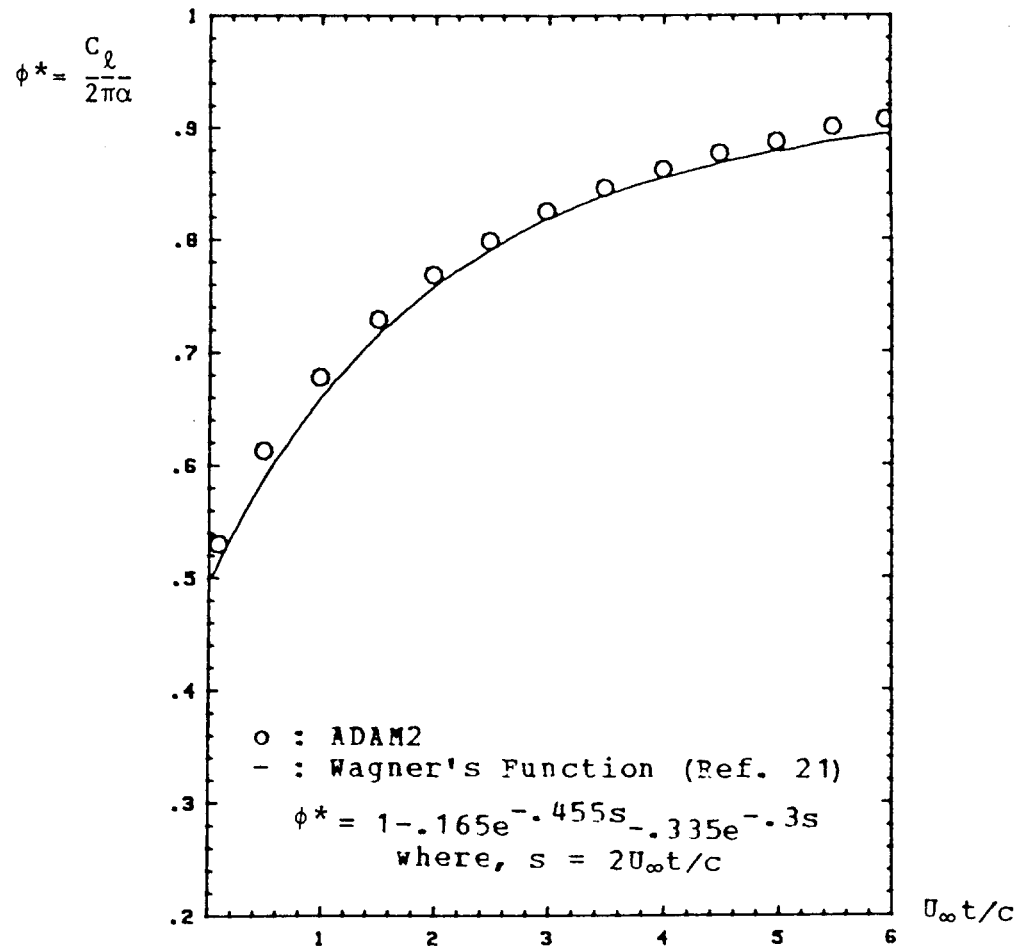
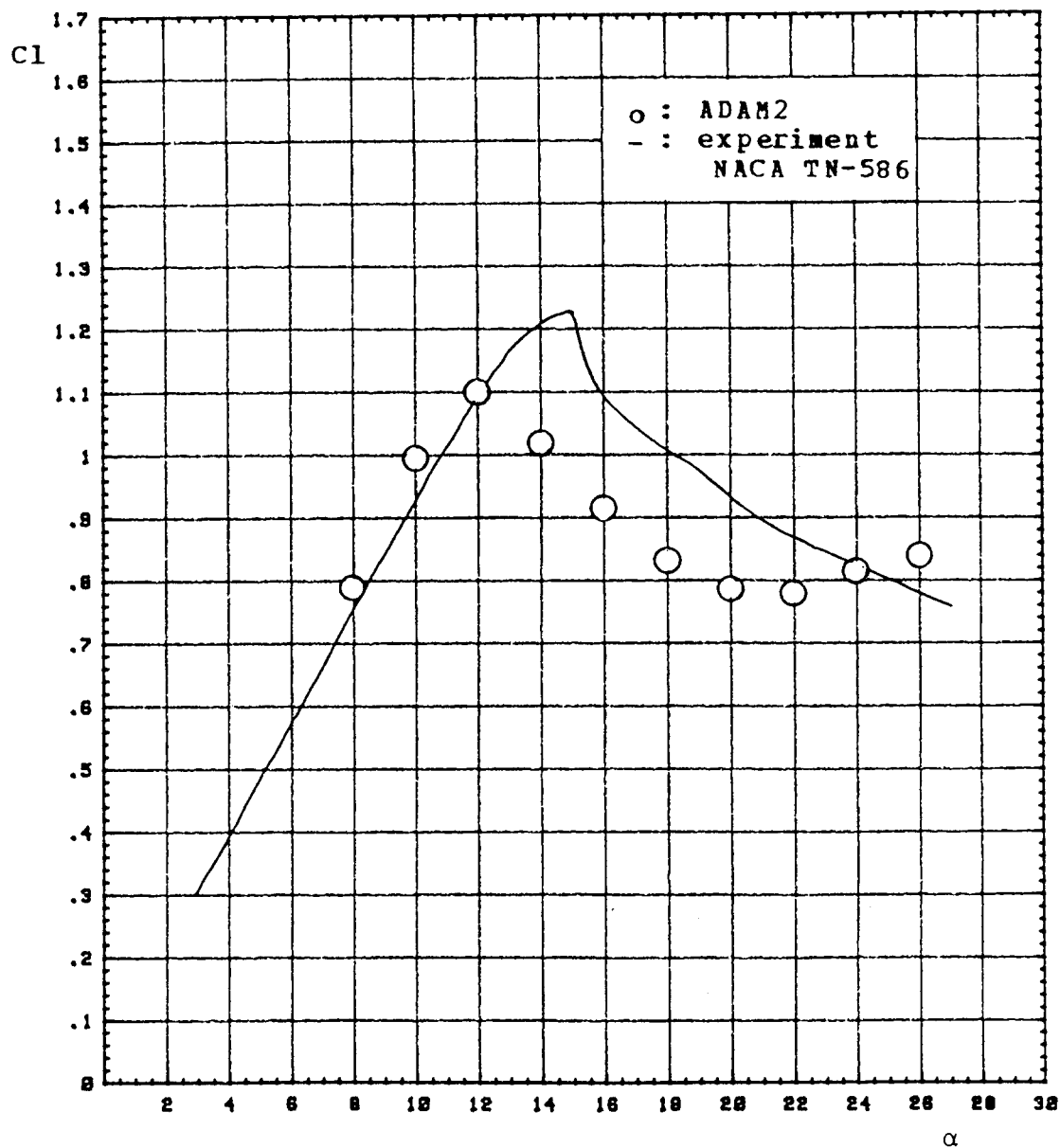Figure 4.11   Indicial Lift on an Impulsively Started Flat
Plate Airfoil

74

Figure 4.12   Variation of Lift Coefficients for
a NACA 0015 Airfoil at Re=655,000
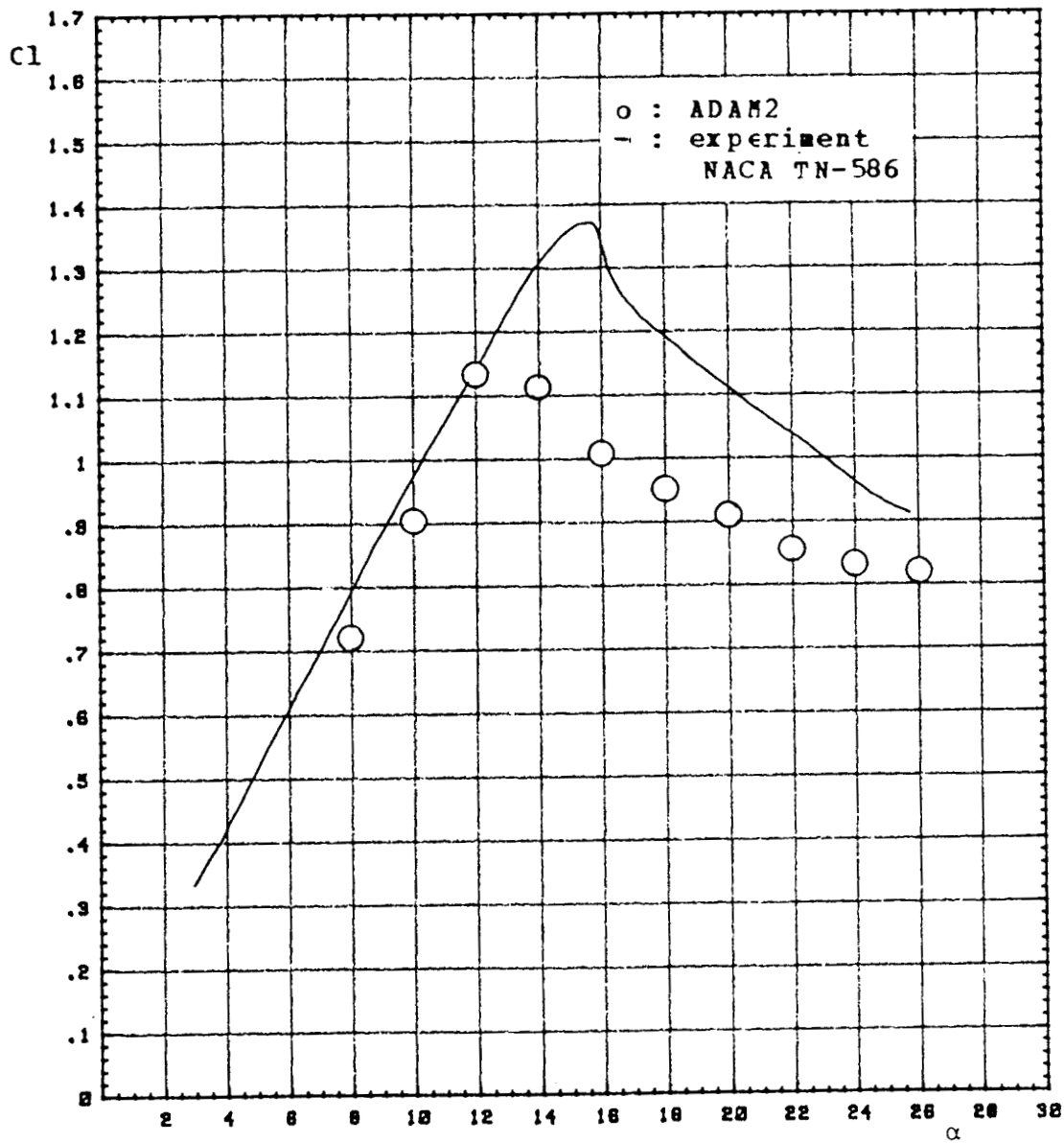
Figure 4.13   Variation of Lift Coefficients for
a NACA 0015 Airfoil at Re=1,270,000
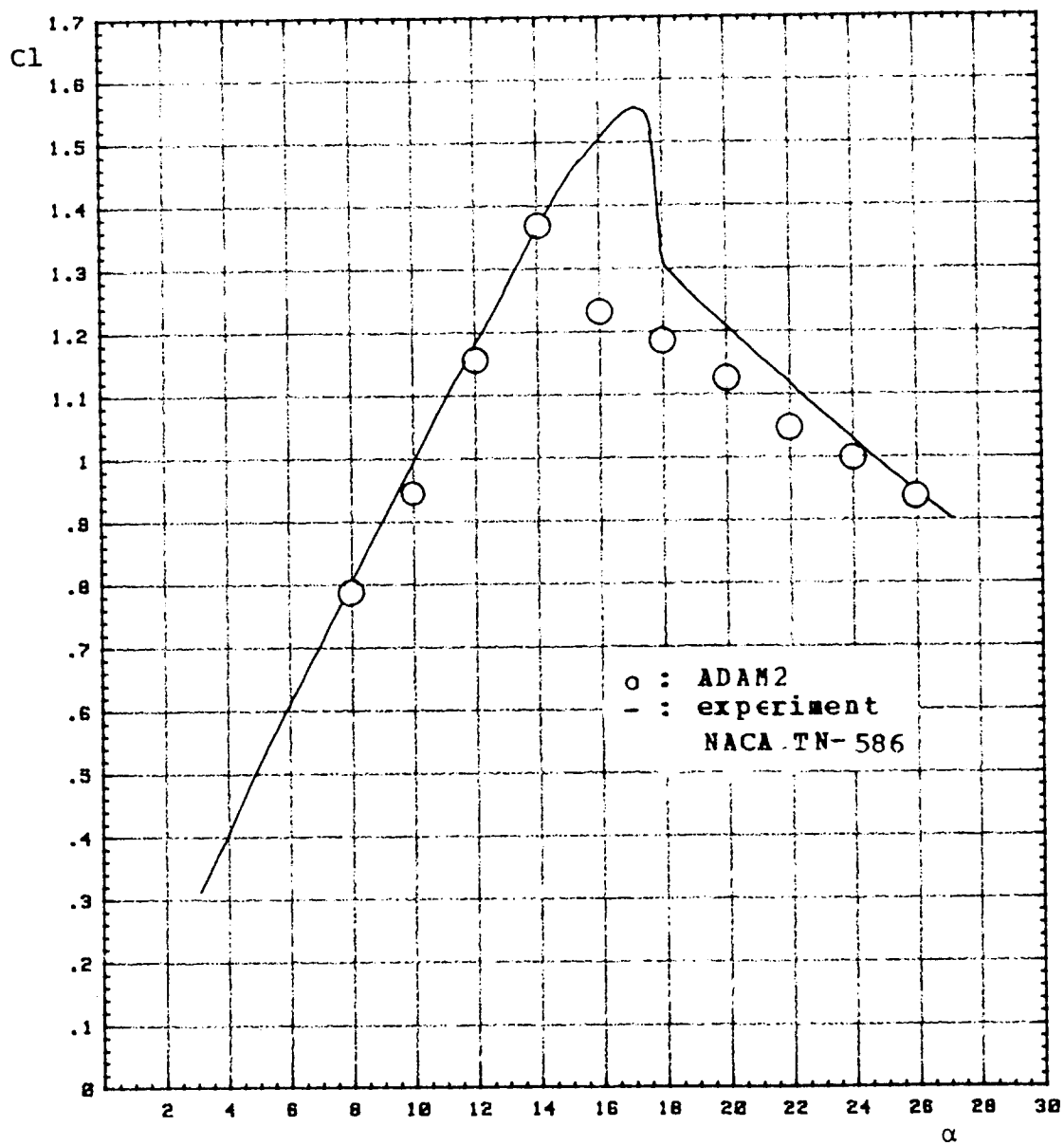
Figure 4.14   Variation of Lift Coefficients for
a NACA 0015 Airfoil at Re=3,260,000

progressively approaches its steady location. Currently, ADAM2 has difficulties in accurately predicting the movement of the boundary layer separation point. It generally advances towards the leading edge faster and further than expected. Basically, the influence of the nascent separating vortex on the suction side of an airfoil is disproportionately large which strengthens the adverse pressure gradient ahead of the instantaneous separation point. Consequently, there is a tendency for the separation point to be predicted further forward at each time step. For these reasons, the calculated lift tends to indicate an earlier stall than the experimental data.

Fig. 4.15 illustrates typical lift coefficient variations which occur over the 20 chord lengths of travel. The oscillatory changes of the lift are considered to be caused by wake surface deformation as well as slight variations of separation point location.

Since the vorticity shedding rate and the increment to $\partial\phi/\partial t$ are determined by the local edge velocity at the separation point, slight changes of separation point location will strongly affect the calculation of the surface pressure beneath separated wake surface. The value of $\partial\phi/\partial t$ itself was unrealistically large in the author's previous work (Ref. 20) and a reduction factor was required to obtain reasonable results. Similar problems have also been reported in the literature (see Ref. 16 and 45). However, it should be noted that no reduction factors are necessary for ADAM2. The use of a higher order panel singularity distribution is considered to be a major contributor to these improvements.

Fig. 4.16 illustrates a typical calculated wake geometry after 20 chord lengths of travel. The wake geometry has the familiar form of the
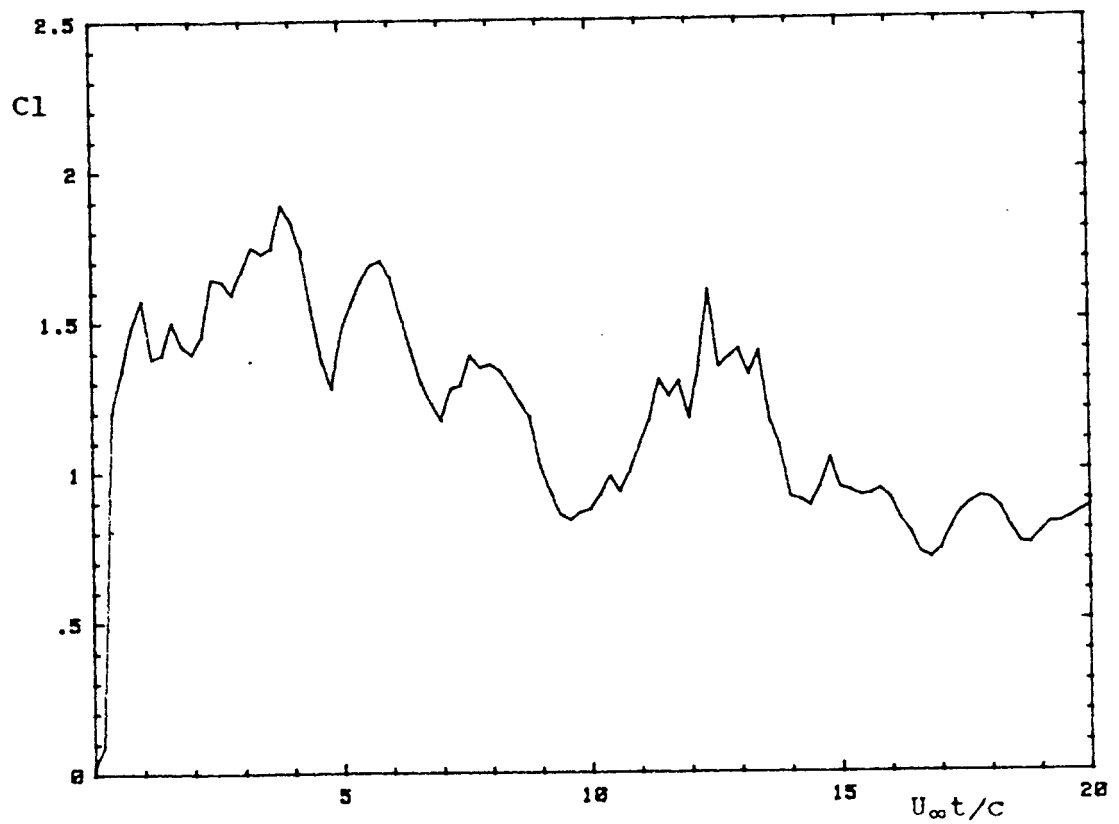
Figure 4.15   Variation of Lift Coefficients for an
               Impulsively Started NACA 0015 Airfoil at
               18° Angle of Attack and Re=3,260,000
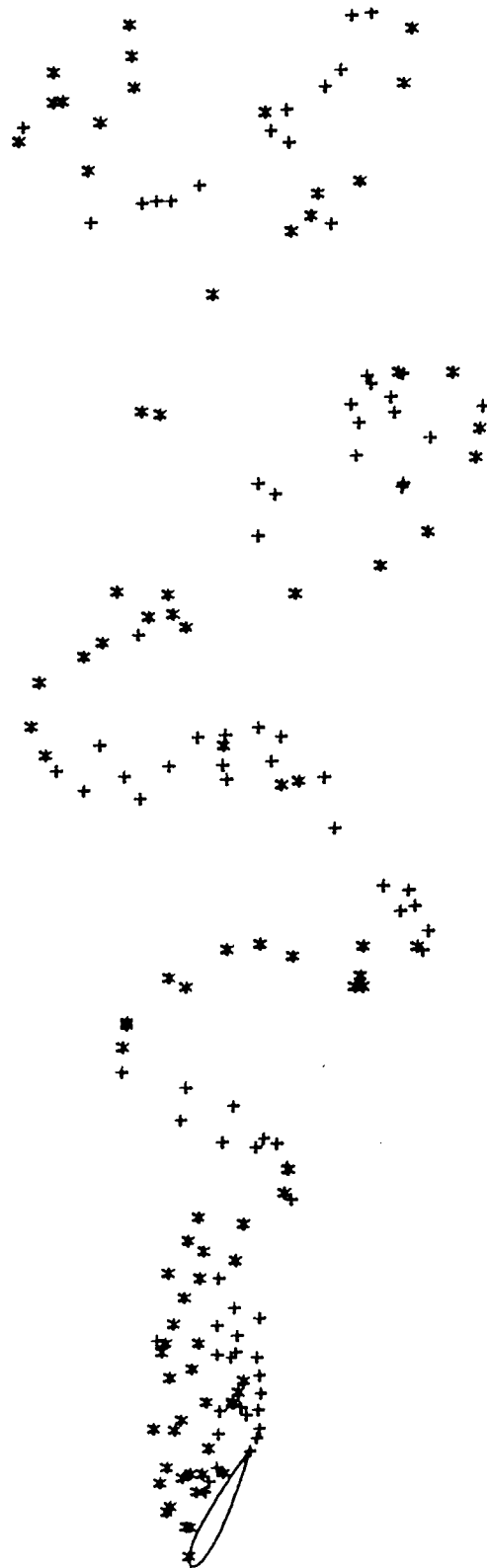
Figure 4.16 Wake Geometries Behind a NACA 0015 Airfoil at an Angle of Attack Equal to 26°

classical vortex street. The periodic nature of this wake structure is the source of the low frequency lift and drag fluctuations shown in Fig. 4.15. The frequency of the large vortex shedding may be nondimensionalized with the freestream velocity and the breadth of the airfoil across the stream to form a Strouhal number. The Strouhal number for the case of Fig. 4.16 is approximately 0.175 which agrees well with the experimental value of 0.18 reported by Blenk, Fuchs, and Liebers (Ref. 56).

Fig. 4.17 illustrates the comparison between the experimental and computed pressure distributions on an NLF (1)-0416 airfoil at a post stall angle of attack. The agreement is excellent, particularly on the suction side within the separated region. In this case, the separation point is predicted at 25% chord which is just ahead of a calculated sudden pressure drop on the suction side of the airfoil. Currently, a step change is applied across the separation point to represent the additional increment to the time derivatives of the velocity potential due to the boundary layer separation. However, in observing the actual separation phenonenon, it is observed that the boundary layer starts thickening throughout a relatively broad transition area before it separates fully. An accurate mathematical representation of the boundary layer separation process should include the effects of finite separation development length. One effect will be to diffuse the increment of $\partial\phi/\partial t$ which should result in a more continuous pressure variation in the vicinity of a separation point.

Figs. 4.18 through 4.21 illustrate the lift and drag coefficient variations as a function of time for the case of an airfoil undergoing a constant pitching motion. The calculated drag is in good agreement with
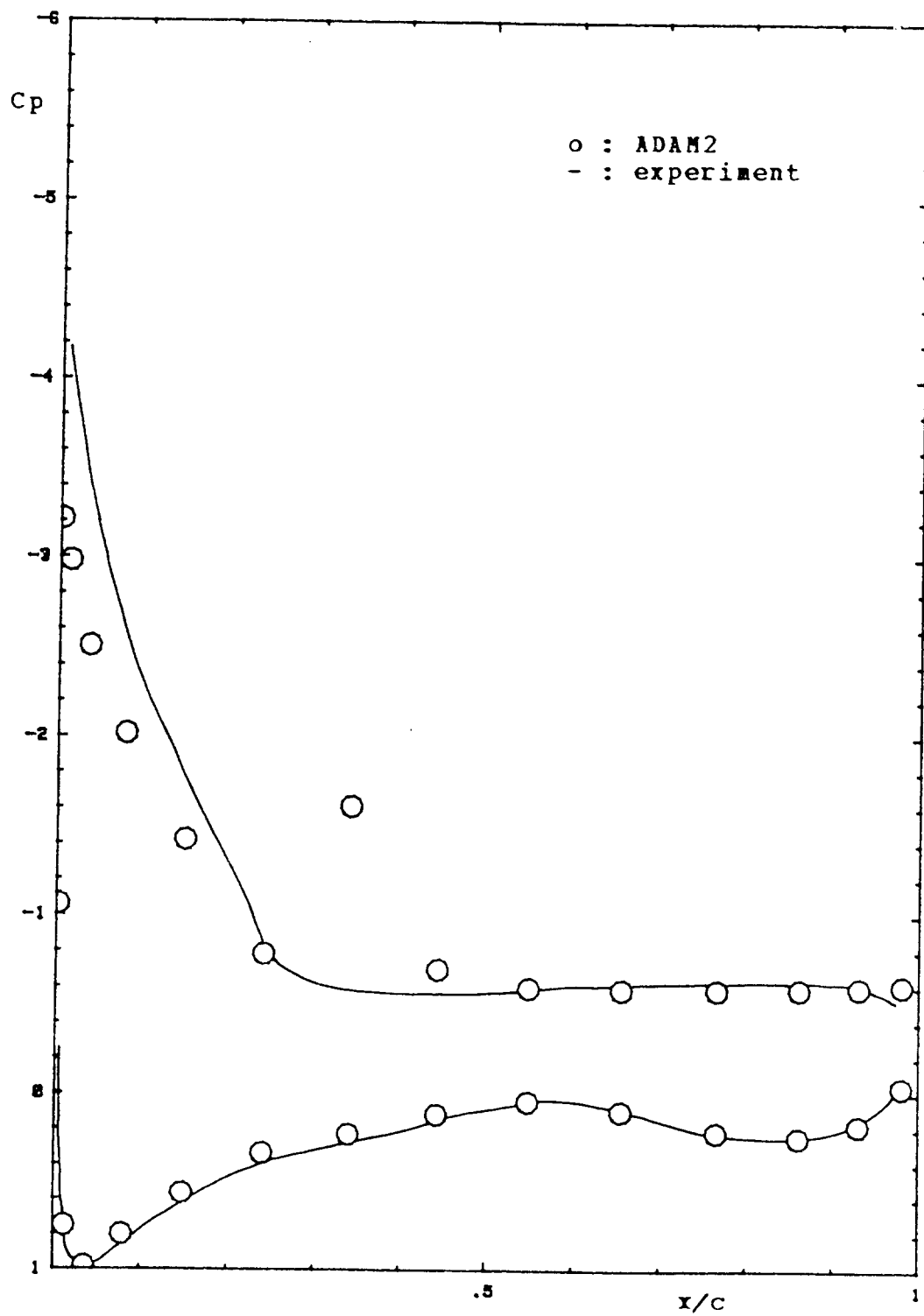
Figure 4.17   Pressure Distribution on an NLF(1)-0416
              Airfoil at 17.16° Angle of Attack and
              Re=1,000,000
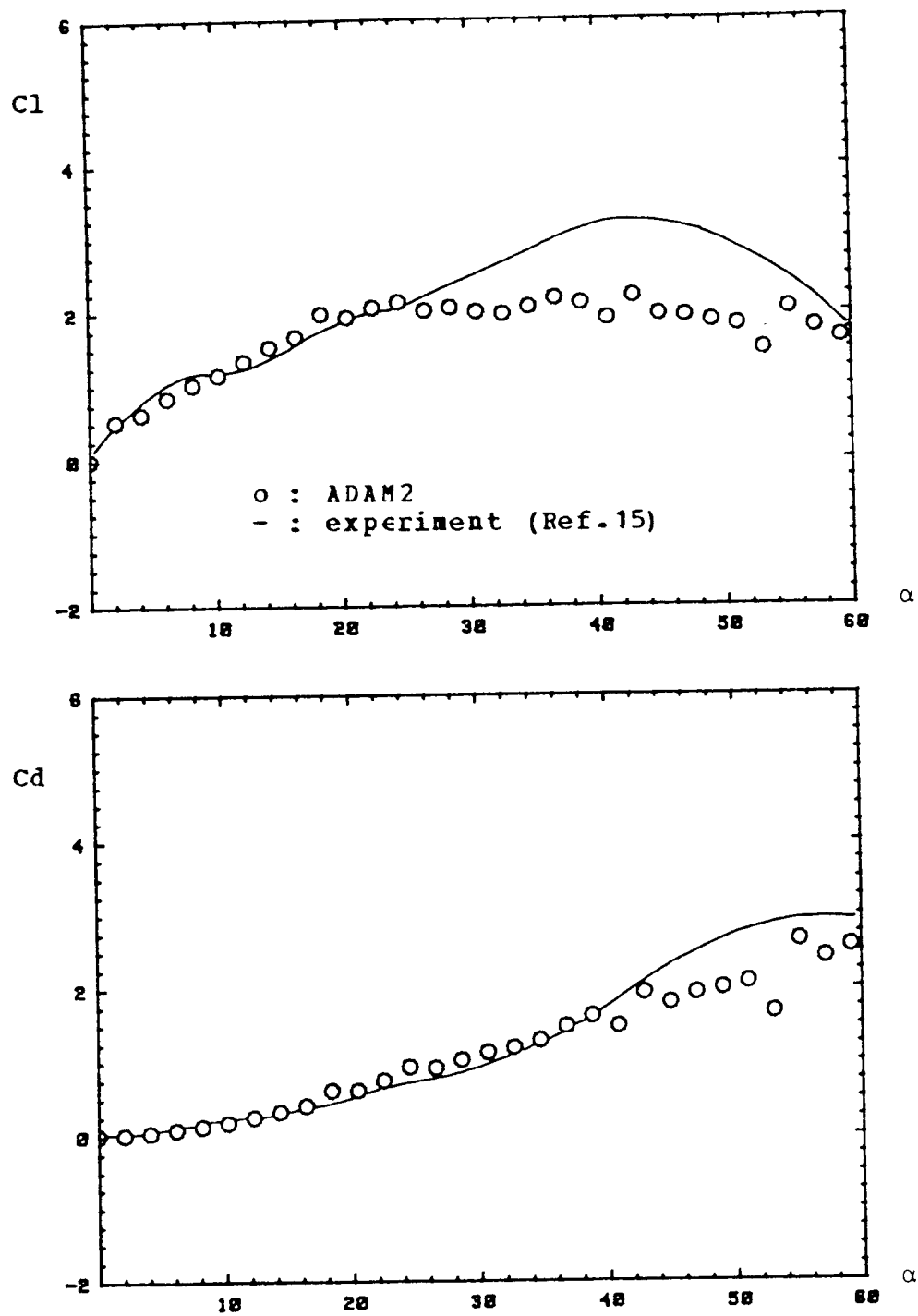
Figure 4.18   The Lift and Drag Coefficient for a NACA 0015
              Airfoil in Pitching Motion (Re=100,000,
              k=.089, 25% chord pitching center)
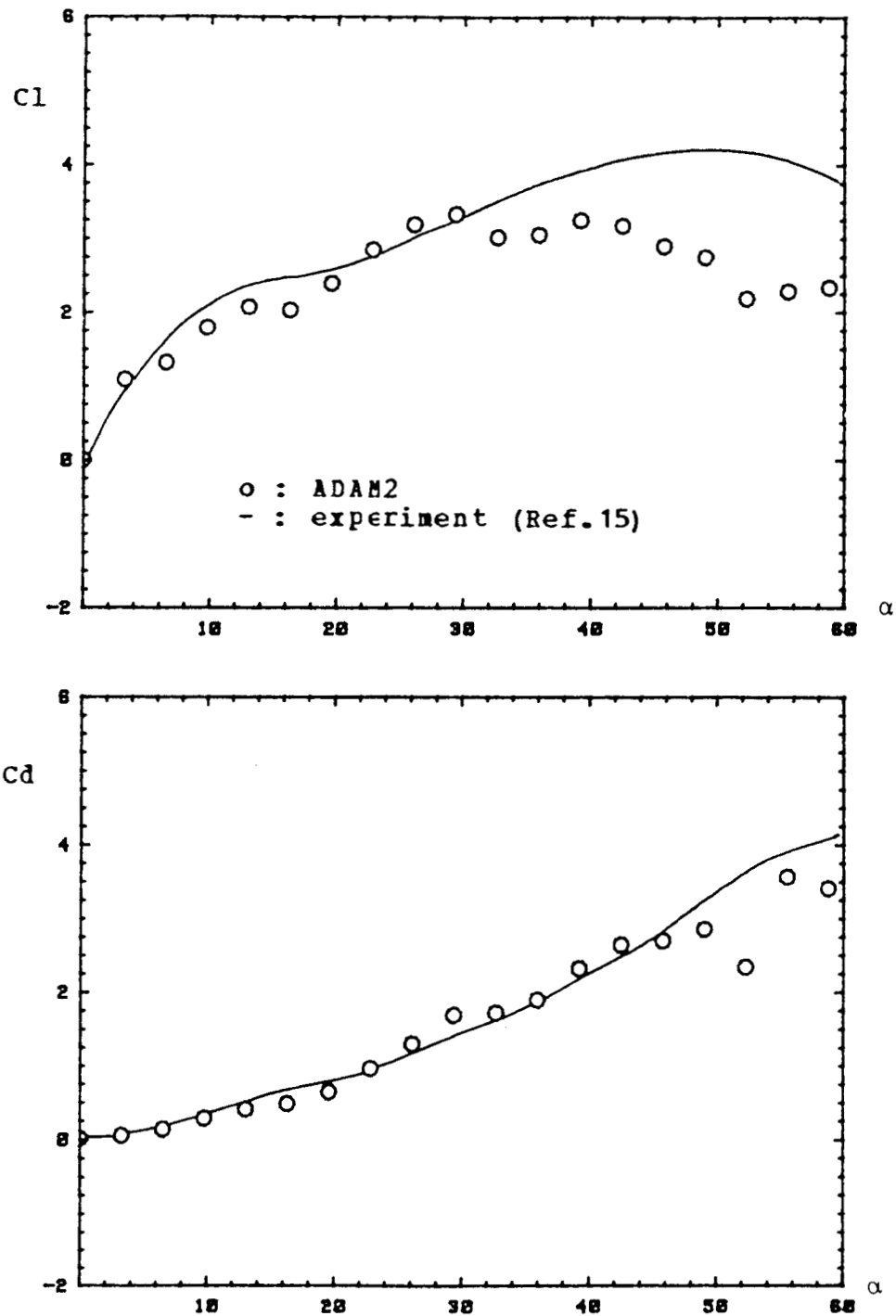
Figure 4.19   The Lift and Drag Coefficient for a NACA 0015
               Airfoil in Pitching Motion (Re=100,000,
               k=.19, 25% chord pitching center)
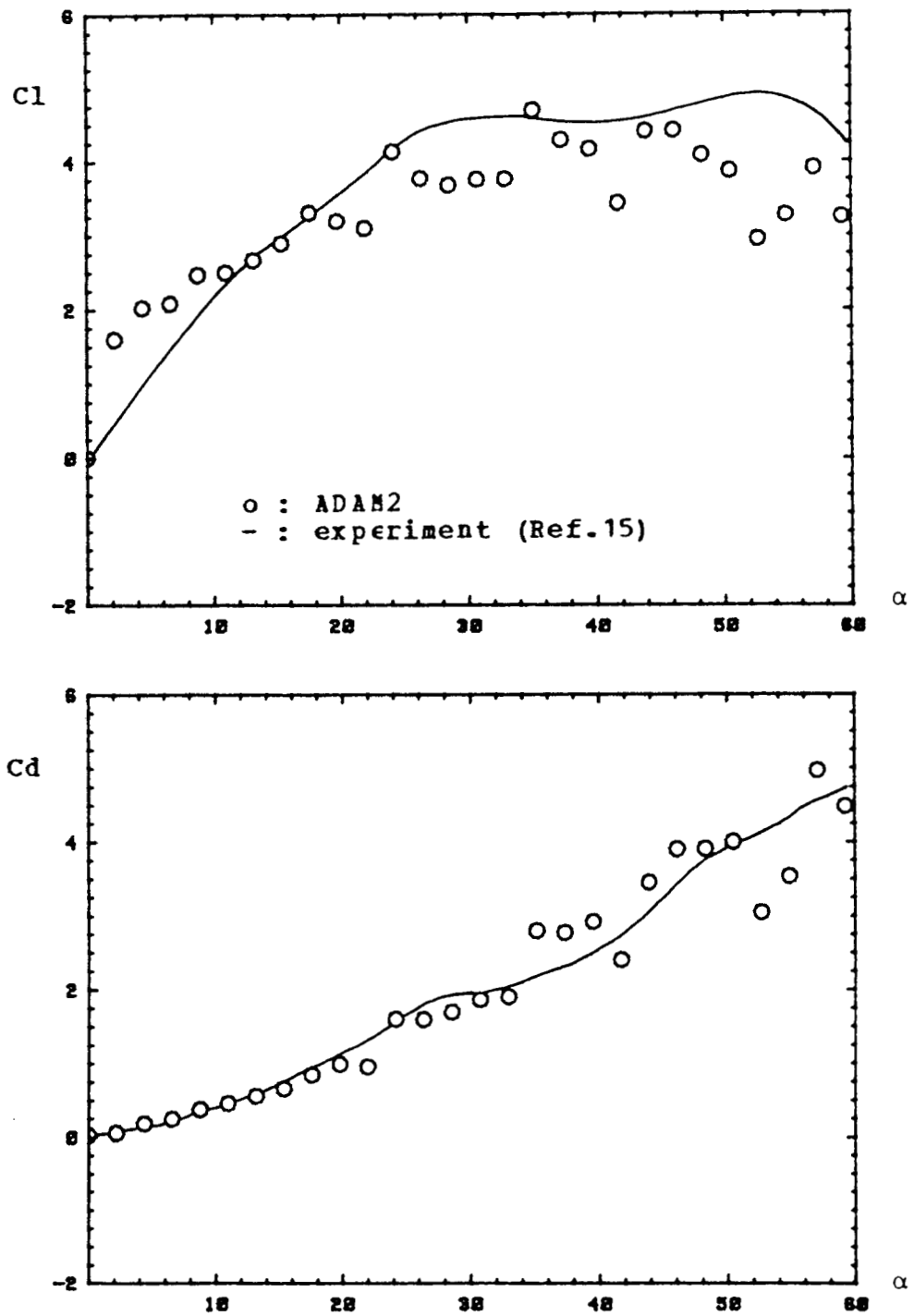
Figure 4.20   The Lift and Drag Coefficient for a NACA 0015
Airfoil in Pitching Motion (Re=100,000,
k=.29, 25% chord pitching center)
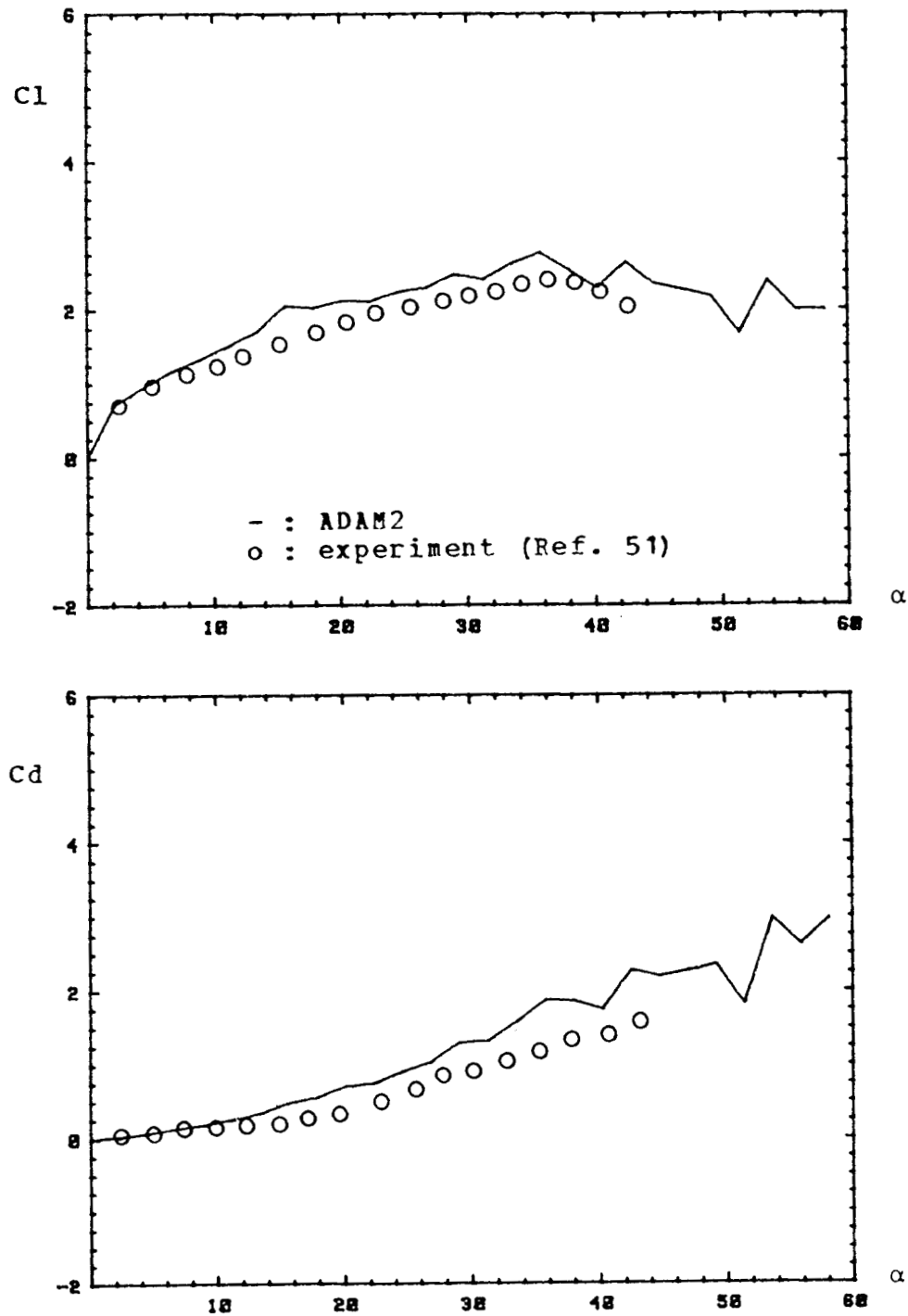
Figure 4.21   The Lift and Drag Coefficient for a NACA 0012
Airfoil in Pitching Motion (Re=77,700,
k=.13, 31.7% chord pitching center)

experimental data for all cases. However, the lift is considerably underestimated at the relatively high angle of attack ranges. This underestimation may also be caused by the unrealistically rapid boundary layer separation point progression predicted by ADAM2.

Fig. 4.22 presents the calculated and experimental variations of lift coefficient versus time for a NACA 0012 airfoil in oscillatory pitching motion. As is shown in the figure, ADAM2 underestimates the lift for the majority of the hysterisis loop. According to the experimental data (Ref. 35), the boundary layer separation point moves forward when the airfoil pitches up and toward the trailing edge when it pitches down. As was noted in the constant pitching cases, ADAM2 tends to over-predict the forward separation point movement as the airfoil pitches up. It also tends to under-predict the separation point retreatment as the airfoil pitches down. The backward movement is retarded to the extent that complete re-attachment does not occur at the end of a pitch cycle. Again, unreasonably strong influence of the separating vortex on the suction side of the air-foil is considered to be the source of the problem.
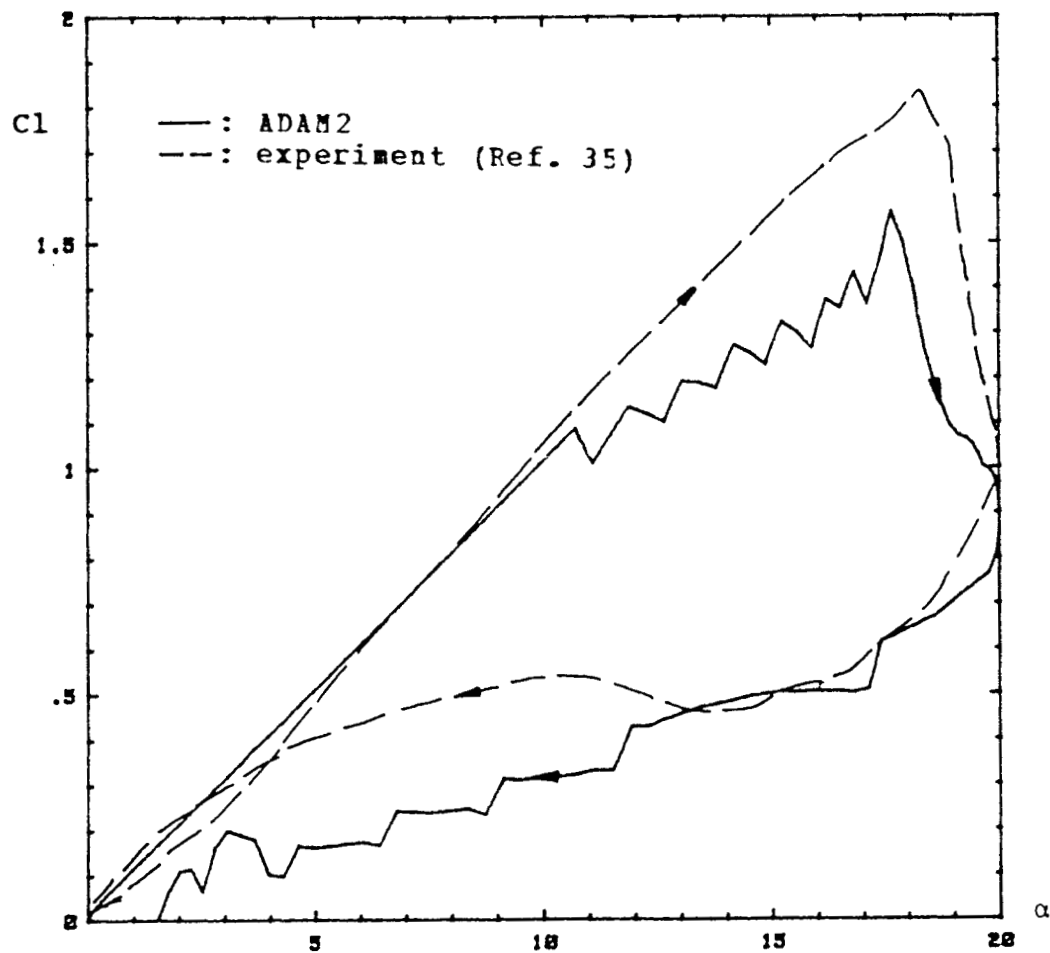
Figure 4.22 Lift Variations on a NACA 0012 Airfoil with
            Oacillatory Pitching Motion (Re =4,000,000,
            α=10°+10°sin(.2t), 25% chord pitching center)

CHAPTER V

CONCLUSIONS AND RECOMMENDATIONS

This chapter contains a summary of conclusions from the current study, and recommendations for future work.

5.1 Conclusions

A numerical model which is theoretically capable of predicting aerodynamic characteristics for an unsteady airfoil motion at high angles of attack has been developed in the current investigation. The capability of the current model, ADAM2, has been examined for various types of airfoils in steady and unsteady flow situations. For all the cases tested, the prediction accuracy has been notably improved over the previous model, USTAR2 (Ref. 20). In particular, the calculations for steady attached flows are sufficiently accurate to enable ADAM2 to be used as an analysis tool. The calculation results for separated flows have reasonable accuracy even though the current model has some difficulties yet to be overcome. More accurate predictions for these cases may be possible through the development of an improved representation of the viscid and inviscid interaction in the vicinity of boundary layer separation.

5.2 Recommendations

One of the goals of the current research was to develop a numerical model of dynamic stall as it occurs on the Darrieus turbine. In addition to that, the recently introduced supermaneuverability concept may be another stimulant to the development of models similar to ADAM2. In order to accomplish such goals, more investigations in the following areas are recommended.

1. More precise representation of the flow is needed in the vicinity of the boundary layer separation point and origin of the separating wake.

2. The inviscid model may need improvements to handle the laminar separation bubble phenomena which is often observed on a pitching airfoil.

REFERENCES

1. Abbot, I. H. and Doenhoff, A. E. ; "Theory of Wing Sections," Dover, 1949.

2. Arena, A. V. and Mueller, T. ; "Laminar Separation, Transition, and Turbulent Reattachment Near the Leading Edge of Airfoils," AIAA J., Vol. 18, 1980, pp. 747-753.

3. Ashley, H. ; "Machine Computation of Aerodynamic Loads in Linear and Nonlinear Situations," Fluid Dynamics Research Lab. Rept. 66-5, AFOSR 66-1440, 1966.

4. Bristow, D. R. and Grose, G. G. ; "Modification of the Douglas Neumann Program To Improve the Efficiency of Predicting Component Interference and High Lift Characteristics," NASA CR-3020, 1978.

5. Bristow, D. R. ; "Development of Panel Methods For Subsonic Analysis and Design," NASA CR-3234, 1980.

6. Bristow, D. R. and Hawk, J. D. ; "Subsonic Panel Method For the Efficient Analysis of Multiple Geometry Perturbations," NACA CR-3528, 1982.

7. Cebecci, T. and Smith, A. M. O. ; "Analysis of Turbulent Boundary Layers," Academic Press, 1974.

8. Clements, R. R. and Maull, D. J. ; "The Representation of Sheets of Vorticity by Discrete Vortices," Prog. in Aerospace Sciences, Vol. 16, 1971, p. 129.

9. Coles, D. ; "The Law of the Wake in the Turbulent Boundary Layer," JFM, Vol. 1, 1956, pp. 191-226.

10. Coles, D. and Hirst, E. A. ; "Computation of Turbulent Boundary Layers," 1968 AFOSR-RFP, Vol. 2, Stanford University.

11. Daneshayer, H. and Mugglestone, P. R. ; "An Integral Method for Calculating the Development of a Turbulent Boundary Layer with a Fluctuating Mainstream," Iranian J. of Science and Technology, Vol. 7, 1978, pp. 17-35.

12. Deffenbaugh, F. D. and Marshall, F. J. ; "Time Development of the Flow About an Impulsively Started Cylinder," AIAA J., Vol. 14, 1976, pp. 908-913.

13. Djojodihardjo, R. H. and Widnall, S. E. ; "A Numerical Method for the Calculation of Nonlinear, Unsteady Lifting Potential Flow Problems," AIAA J., Vol. 7, 1969, pp. 2001-2009.

91

14. Dwyer, H. A. and McCroskey, W. J. ; "Crossflow and Unsteady Boundary Layer Effects on Rotating Blades," AIAA J., Vol. 9, 1971, pp. 1498-1505.

15. Gerrard, J. H. ; "Numerical Computation of the Magnitude and Frequency of the Lift on a Circular Cylinder," Philosophical Transaction of the Royal Society of London, Vol. 261, 1967, pp. 137-162.

16. Goldstein, S. ; "Modern Developments in Fluid Dynamics," Dover, 1965.

17. Graham, G. M. ; "An Experimental Investigation of an Airfoil Pitching at Moderate to High Rates up to Large Angles of Attack," Ph.D. Dissertation, Texas Tech University, In Progress.

18. Ham, N. D. ; "Aerodynamic Loading on a Two-Dimensional Airfoil During Dynamic Stall," AIAA J., Vol. 6, 1968, pp. 1927-1934.

19. Houdeville, R. and Cousteix, J. ; "Premiers Resultats D'une Etude sur les Couches Limites Turbulentes en Encoulement Pulse Avec Gradient de Pression Moyen Defavorable," Translated into English in NASA TN-75799, 1979.

20. Im, B. J. ; A Numerical Method for the Calculation of Unsteady Lifting Potential Flow Problems," Master's Thesis, Texas Tech Univ., 1982.

21. Jones, R. T. ; "The Unsteady Lift of a Finite Wing," NACA TN-682, 1939.

22. Kadlec, E. G. ; "Overview of Current and Future Design Characteristics (of VAWT's)," Proceedings - VAWT Design Technology Seminar for Industry, Sandia Laboratory Rept. SAND80-0984, 1980.

23. Karamcheti, K. ; "Principles of Ideal-Fluid Aerodynamics," John Wiley and Sons, 1966.

24. Karlson, S. K. F. ; "Unsteady Turbulent Boundary Layer," J. Fluid Mechanics, Vol. 5, 1966.

25. Kim, J., Kline, S. J., and Johnston, J. P. ; "Investigation of Seperation and Reattachment of a Turbulent Shear Layer: Flow Over a Backward-Facing Step," J. Fluids Engrg., Vol. 102, 1980, pp. 392-398.

26. Kiya, M. and Arie, M. ; "A Contribution to an Inviscid Vortex-Shedding Model for an Inclined Flat Plate in Uniform Flow," J. Fluid Mech., Vol. 82, 1977, pp. 223-240.

27. Klimas, P. C. ; "Vertical Axis Wind Turbine Aerodynamic Performance Prediction Methods" Proceedings - VAWT Design Technology Seminar for Industry, Sandia Labratory Rept. SAND80-0984, 1980.

28. Klimas, P. C. ; "Possible Aerodynamic Improvements for Future VAWT System," Proceedings - VAWT Design Technology Seminar for Industry, Sandia Laboratory Rept. SAND80-0984, 1980.

29. Kraus, W. ; "Panel Methods in Aerodynamics-Numerical Methods in Fluid Dynamics," McGraw-Hill, Editors Wirz and Smolderen, 1978, pp. 237-297.

30. Lamb, Horace ; "Hydrodynamics," Dover Publications, 1932.

31. Lewis, R. I. ; "Surface Vorticity Modelling of Separated Flows From Two-Dimensional Bluff Bodies of Arbitrary Shape," J. of Mech. Engrg. Science, Vol. 21, 1981, pp. 1-12.

32. Lyrio, A. A., Ferziger, J. H., and Kline, S. J. ; "An Integral Method for the Computation of Steady and Unsteady Turbulent Boundary Layer Flows, Including the Transitory Stall Regime in Diffusers," Stanford University Report PD-23, 1981.

33. McCroskey, W. J. ; "Inviscid Flowfield of an Unsteady Airfoil," AIAA J., Vol. 11, 1973, pp. 1130-1137.

34. McCroskey, W. J. and Phillippe, J. J. ; "Unsteady Viscous Flow on Oscillating Airfoils," AIAA J., Vol. 13, 1975, pp. 71-79.

35. McCroskey, W. J. and Pucci, S. I. ; "Viscous - Inviscid Interaction on Oscillating Airfoil in Subsonic Flow," AIAA J., Vol. 20, 1982, pp. 167-174.

36. Morino, L. and Kuo, C. C. ; "Subsonic Potential Aerodynamics for Complex Configurations: A General Theory," AIAA J., Vol. 12, 1974, pp. 191-197.

37. Nash, J. F. and Patel, V. C. ; "Improved Entrainment Method for Calculating Turbulent Boundary Layer Development," NASA CR-2546, 1969.

38. Nash, J. F., Carr, L. W., and Singleton, R. E. ; "Unsteady Turbulent Boundary Layers in Two-Dimensional Incompressible Flow," AIAA J., Vol. 13, 1975, pp. 176-183.

39. Nash, J. F. and Scruggs, R. M. ; "Unsteady Boundary Layers with Reversal and Separation," Proceedings-Unsteady Aerodynamics, AGARD CP-227, 1978, pp. 18.1-18.12.

40. Oler, J. W. ; "An Investigation of a Numerical Method for the Exact Calculation of Unsteady Airloads Associated with Wing Intersection Problems," M.S. Thesis, University of Texas - Austin., 1976.

41. Oler, J. W. and Strickland, J. H. ; "Dynamic Stall Regulation of the Darrieus Turbine," Final Report on Sandia Contract No. 74-1218, 1982.

42. Robert, P. E. and Saaris, G. R. ; "Review and Evaluation of A Three-Dimensional Lifting Potential Flow Computational Method for Arbitrary Configurations," Boeing Co., 1972.

43. Roberts, W. B. ; "Calculation of Laminar Separation Bubbles and Their Effect on Airfoil Performance," AIAA J., Vol. 18, 1980, pp. 25-31.

44. Sandborn, V. A. and Kline, S. J. ; "Flow Models in Boundary Layer Stall Inception," J. of Basic Engineering, Trans. ASME, 1961, pp. 317-327.

45. Sarpkaya, Turgut ; "An Inviscid Model of Two-Dimensional Vortex Shedding for Transient and Asymptotically Steady Separated Flow Over an Inclined Plate," J. Fluid Mech., Vol. 68, part 1, 1975, pp. 109-128.

46. Sarpkaya, T., and Schoaff, R. L. ; "Inviscid Model of Two-Dimensional Vortex Shedding by a Circular Cylinder," AIAA J., Vol. 17, 1979, pp. 1193-1200.

47. Sarpkaya, T. and Kline, H. K. ; "Impulsively-Started Flow About Four Types of Bluff Body," J. of Fluids Engrg., Vol. 104, 1982, pp. 207-213.

48. Simpson, R. L., Strickland, J. H. and Barr, P. W. ; "Features of a Separating Turbulent Boundary Layer in the Vicinity of Separation ," JFM, Vol. 79, 1977, pp. 553-594.

49. Singleton, R. E. and Nash, J. F. ; "Method for Calculating Unsteady Turbulent Boundary Layers in Two- and Three-Dimensional Flows," AIAA J., Vol. 12, 1974, pp. 590-595.

50. Smith, A. M. O. and Hess, J. L. ; "Calculation of the Nonlifting Potential Flow About Arbitrary Three-Dimensional Bodies," Douglas Report. # E.S. 40622, 1967.

51. Strickland, J. H. ; "Dynamic Stall: A Study of the Constant Pitching Rate Case," USAF Summer Faculty Research Program 1983 Report.

52. Summa, J. M. ; "Potential Flow About Impulsively Started Rotors," J. Aircraft, Vol. 13, 1976, pp. 317-319.

53. Telionis, D. P. ; "Calculation of Time-Dependent Boundary Layers," Unsteady Aerodynamics, R. B. Kinney Ed., Vol. 1, 1975, p. 155.

54. Williams, J. C. ; "Flow Development in the Vicinity of the Sharp Trailing Edge on Bodies Impulsively Set Into Motion," J. of Fluid Mech., Vol. 115, 1982, pp. 27-37.

55. Woodward, F. A. ; "An Improved Method for the Aerodynamic Analysis of Wing-Body-Trail Configurations in Subsonic and Supersonic Flow," NASA CR-2228, 1973.

56. Blenk, H. F., Fuchs, D., and Liebers, F.; "Uber Messungen von Wirbelfrequenzen," Luftfahrtforschung, Vol. 12, 1935, pp. 38-41.

DISTURBANCE VELOCITY CALCULATIONS
FROM A SINGULARITY ELEMENT

This section contains the exact derivations of the induced velocities from various singularity distributions. Notations used here are illustrated in Fig. A.1.

A.1 For A Constant Source Distribution

$$\vec{V}_{S1} = \int_{-\frac{S}{2}}^{\frac{S}{2}} \frac{\mu d}{2\pi |R|} (\cos\theta \vec{i} + \sin\theta \vec{j})$$

$$= \begin{cases} \frac{\mu}{2\pi} \left[\ln\left|\frac{R_1}{R_2}\right| \vec{i} - (\theta_1 - \theta_2)\vec{j} \right] & , \quad n_0 \neq 0 \\[3em] \frac{\mu}{2\pi} \ln\left|\frac{R_1}{R_2}\right| \vec{i} & , \quad n_0 = 0 \end{cases}$$

A.2 For A Linear Source Distribution

$$\vec{V}_{SL} = \int_{-\frac{S}{2}}^{0} \frac{\mu d}{2\pi |R|} (\cos\theta \vec{i} + \theta \vec{j}),$$

$$= \begin{cases} \frac{a_1}{2\pi} \left[\xi_0 \ln\left|\frac{R_1}{R_0}\right| - \frac{S}{2} + n_0(\theta_0 - \theta_1) \right] \vec{i} \\[3em] - \frac{a_1}{2\pi} \left[\xi_0(\theta_1 - \theta_0) + n_0\ln\left|\frac{R_1}{R_0}\right| \right] \vec{j}, & n_0 \neq 0 \end{cases}$$
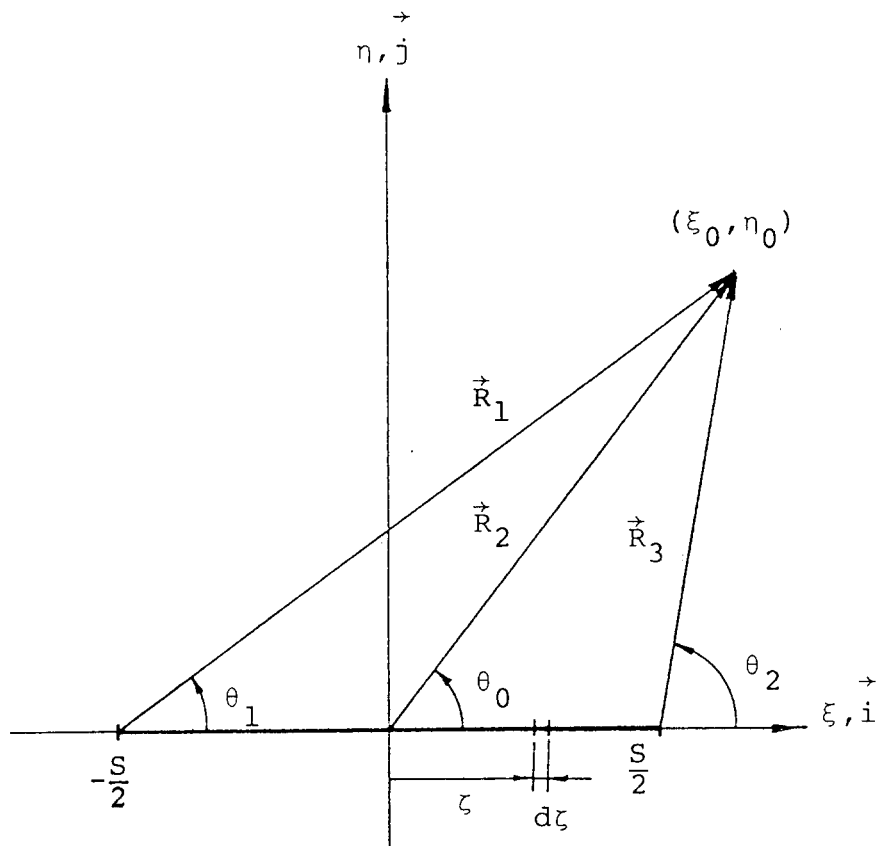
Figure A.1   Coordinate System for a Singularity Element

$$\left.\frac{1}{2\pi}\ \left[\xi_0 \ell n\ \left|\frac{R_1}{R_0}\right|\ -\ \frac{S}{2}\right]\ \vec{i}\right|^a \qquad\qquad , \qquad\qquad \eta_0 = 0$$

$$\vec{V}_{SR} = \int_o^{\frac{S}{2}}\ \frac{\mu\,d\zeta}{2\pi\,\overline{\left|\,R\,\right|}}\ (\cos\theta\,\vec{i} + \sin\theta\,\vec{j}),$$

$$= \begin{cases} \dfrac{a_2}{2\pi}\ \left[\xi_0 \ell n\ \left|\dfrac{R_0}{R_2}\right|\ -\ \dfrac{S}{2}\ +\ \eta_0(\theta_2 - \theta_0)\right]\ \vec{i} \\[2em] \qquad -\ \dfrac{a_2}{2\pi}\ \left[\xi_0(\theta_0 - \theta_2)\ +\ \eta_0 \ell n\ \left|\dfrac{R_0}{R_2}\right|\right]\ \vec{j}, \qquad \eta_0 \neq 0 \\[2em] \dfrac{a_2}{2\pi}\ \left[\xi_0 \ell n\ \left|\dfrac{R_0}{R_2}\right|\ -\ \dfrac{S}{2}\right]\ \vec{i} \qquad\qquad , \qquad \eta_0 = 0 \end{cases}$$

A.3 For A Constant Vortex Distribution

$$\vec{V}_{V1} = \int_{-\frac{S}{2}}^{\frac{S}{2}}\ \frac{\gamma\,ds}{2\pi\,\overline{\left|\,R\,\right|}}\ (-\sin\theta\,\vec{i} + \cos\theta\,\vec{j})$$

$$= \begin{cases} \dfrac{\gamma}{2\pi}\ \left[(\theta_1 - \theta_2)i\ +\ \ell n\ \left|\dfrac{R_1}{R_2}\right|\ \vec{j}\right] \qquad , \qquad \eta_0 \neq 0 \\[2em] \dfrac{\gamma}{2\pi}\ \ell n\ \left|\dfrac{R_1}{R_2}\right|\ \vec{j} \qquad\qquad\qquad , \qquad \eta_0 = 0 \end{cases}$$

A.4 For A Linear Vortex Distribution

$$\vec{V}_{V2} = \int_{-\frac{S}{2}}^{\frac{S}{2}} \frac{\gamma d\zeta}{2\pi |R|} \quad (-\sin\theta\vec{i} + \cos\theta\vec{j}),$$

$$= \begin{cases} \dfrac{a}{2\pi} \quad \left[\xi 0(\theta_1 - \theta_2) + \eta_0 \ln \left| \dfrac{R_2}{R_2} \right| \right] \vec{i} \\ \\ + \dfrac{a}{2\pi} \quad \left[\xi_0 \ell n \left| \dfrac{R_1}{R_2} \right| - s - \eta_0(\theta_1 - \theta_2) \right] \vec{j}, \quad \eta_0 \neq 0 \\ \\ \dfrac{a}{2\pi} \quad \left[\xi_0 \ln \left| \dfrac{R_1}{R_2} \right| - s \right] \vec{j} \qquad\qquad , \quad \eta_0 = 0 \end{cases}$$

APPENDIX B

THE PROBLEM IN BODY FIXED
COORDINATES

Assuming that the airfoil is rigid, the functional representation of its surface is independent of time when given with respect to a body fixed coordinate system. This plus the fact that the governing Laplace equation is not explicitly time dependent suggest that it would be advantageous to transform the problem to a body fixed coordinate system.

Consider the motion of an airfoil through an ideal fluid as shown in Fig. B.1. We denote by K with the subscript 'o', operations with respect to the fluid fixed frame. A K or the absence of a subscript indicates operations with respect to the body fixed frame. These coordinate systems are illustrated in Fig. B.1. It should be noted that the translational velocity, $\vec{U}_\infty$, of the K_o frame and the translational and rotational velocities, $\vec{U}_B$ and $\vec{\omega}_B$, of the K frame are taken with respect to an inertially fixed frame.

To establish the connection between the two coordinate systems, note that the position vectors for an arbitrary fluid fixed point P for the two reference frames are related by

$$\vec{r} = \vec{r}(\vec{r}_0, t)$$

$$= [T] \{\vec{r}_0 - \vec{r}_{K_0}(t)\}\] \tag{B.1}$$

where
$$r_{K_0} = \int_0^t \vec{U}_{K_0}(\tau)d\tau + \vec{r}_{K_0}(0)$$

and $[T]$ = coordinate transforamtion matrix, i.e., for any vector $\vec{A}_o$,

$$\{A\} = [T]\{A_o\}.$$
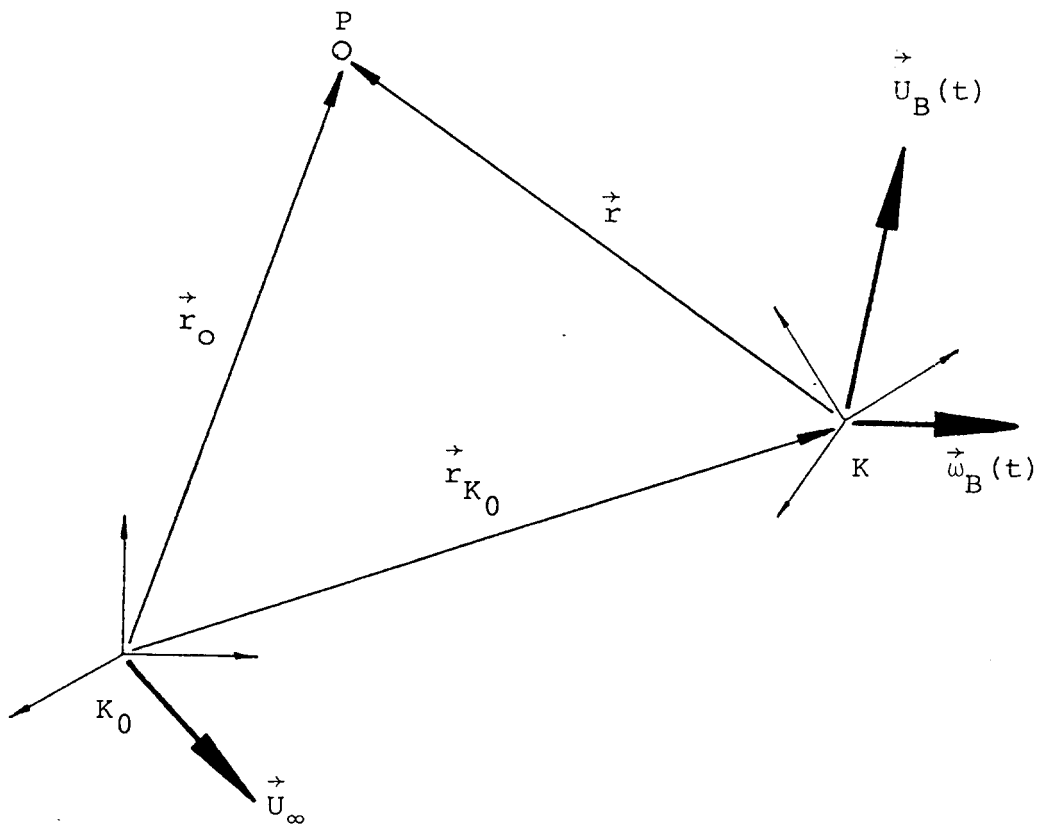
Figure B.1   Inertial and Body Fixed Reference Frame

Consider the potential field, Φ. Since the value of a scalar field is independent of the reference frame, we may write

$$\Phi_0(\vec{r}_0,t) = \Phi(\vec{r},t) \qquad (B.2)$$

Similarly, for the pressure field and airfoil surface function, it follows that

$$P_0(\vec{r}_0,t) = P(\vec{r},t) \qquad (B.3)$$

$$S_0(\vec{r}_0,t) = S(\vec{r},t) \qquad (B.4)$$

In Eq. B.4, advantage has been taken of the fact that S is independent of time with respect to the body fixed reference frame.

Since the gradient operator defines a vector field, gradients from the K_0 and K frames may be related by

$$\{\nabla\} = [T]\{\nabla_0\} \qquad (B.5)$$

Then for the Laplacian,

$$\nabla^2 = \{\nabla\}^T\{\nabla\}$$

or

$$\nabla^2 = \{\nabla_0\}^T[T]^T[T]\{\nabla_0\} \qquad (B.6)$$

For the particular case of a transformation matrix, it may be shown that

$$[T]^{-1} = [T]^T$$

so

$$[T]^T[T] = [I] \qquad (B.7)$$

101

Eq. B.6 then becomes

$$\nabla^2 = \{\nabla_0\}^T \{\nabla_0\}$$

or

$$\nabla^2 = \nabla_0^2 \qquad (B.8)$$

To relate the time derivatives for the two reference frames, we write

$$\frac{\partial}{\partial t_0} = \frac{\partial t}{\partial t_0} \frac{\partial}{\partial t} + \frac{\partial \vec{r}}{\partial t} \cdot \nabla \qquad (B.9)$$

But since time is unchanged by transformation,

$$\frac{\partial t}{\partial t_0} = 1$$

and

$$\frac{\partial}{\partial t_0} = \frac{\partial}{\partial t} + \frac{\partial \vec{r}}{\partial t} \cdot \nabla \qquad (B.10)$$

The second term of the right hand side of Eq. B.10 is the contribution to the temporal variation due to the motion of the K frame relative to the K_0 or fluid fixed frame. In a sense, it is like the convective contribution to a substantial derivative due to the fact that it represents the change of a property $Q(\vec{r})$ resulting from a variation of $\vec{r}$ with respect to the fluid fixed reference frame.

Eq. B.10 may be rewritten as

$$\frac{\partial}{\partial t_0} = \frac{\partial}{\partial t} + [\vec{U}_\infty - \vec{U}_B(t) - \vec{\omega}_B \times \vec{r}] \cdot \nabla \qquad (B.11)$$

102

where the relative velocity between the K and K_0 frames has been written as the difference of their velocity with respect to the inertially fixed frame.

Recall from the previous section that the governing equation for the potential flow model is

$$\nabla_0^2 \Phi_0(\vec{r}_0, t) = 0 \qquad (B.12)$$

where the subscripts 'o' indicate operations with respect to the fluid fixed frame. Subscription of Eqs. B.2 and B.8 into Eq. B.12 yields

$$\nabla^2 \Phi(\vec{r}, t) = 0 \qquad (B.13)$$

which is the governing equation for the body fixed problem.

The surface tangency boundary condition was written for the fluid fixed frame as

$$\frac{1}{\left| \nabla_0 S_0(\vec{r}_0, t) \right|} \frac{\partial S_0(\vec{r}_0, t)}{\partial t} + \nabla_0 \Phi_0(\vec{r}_0, t) \cdot \frac{\nabla_0 S_0(\vec{r}_0, t)}{\left| \nabla_0 S_0(\vec{r}_0, t) \right|} = 0 \qquad (B.14)$$

on $\quad S_0(\vec{r}_0, t) = 0$

Substitution of Eqs. B.2, B.4, and B.8 into Eq. B.14 yields

$$\frac{1}{\left| \nabla S(\vec{r}) \right|} \left\{ \frac{\partial S(\vec{r})}{\partial t} + [\vec{U}_\infty - \vec{U}_B(t) - \vec{\omega}_B(t) \times \vec{r}] \cdot \nabla S(\vec{r}) \right\}$$

$$+ \nabla \Phi \cdot \frac{\nabla S(\vec{r})}{\left| \nabla S(\vec{r}) \right|} = 0$$

or

$$\frac{\partial \Phi(\vec{r},t)}{\partial n(\vec{r})} = - \ [\vec{U}_\infty - \vec{U}_B(t) - \vec{\omega}_B(t) \times \vec{r} - \frac{\partial \vec{n}(r)}{\partial t}]$$ (B.15)

where $n(\vec{r})$ = outward normal on $S(\vec{r}) = 0$ with respect to the

airfoil fixed frame.

An expression for the pressure field in fluid fixed coordinates was

given previously by

$$P(\vec{r}_0,t) = P_\infty - \rho \ \{ \ \frac{\partial \Phi_0(\vec{r}_0,t)}{\partial t} + \frac{1}{2} \ [\nabla_0 \Phi_0(\vec{r}_0,t)]^2 \ \} \ .$$ (B.16)

This may be rewritten in body fixed coordinates as

$$P(\vec{r},t) = P_\infty - \rho \ \ \{ \frac{\partial \Phi(r,t)}{\partial t} + [\vec{U}_\infty - \vec{U}_B - \vec{\omega}_B(t) \times \vec{r}] \cdot \nabla\phi(\vec{r},t)$$

$$+ \frac{1}{2} \ [\nabla\Phi(\vec{r},t)]^2 \} \ .$$ (B.17)

104

DISTRIBUTION:

Alcoa Technical Center (5)
Aluminum Company of America
Alcoa Center, PA   15069
Attn: D. K. Ai
       J. T. Huang
       J. R. Jombock
       M. Klingensmith
       J. L. Prohaska

Alternative Sources of Energy
Milaca, MN 56353
Attn: L. Stoiaken

Amarillo College
Amarillo, TX   79100
Attn: E. Gilmore

American Wind Energy Association
1017 King Street
Alexandria, VA   22314-2922

Arizona State University
University Library
Tempe, AZ   85281
Attn: M. E. Beecher

Dr. A. S. Barker
Trinity Western
7600 Glover Road
Langley, BC
CANADA V3A 4R9

Battelle-Pacific Northwest Laboratory
PO Box 999
Richland, WA   99352
Attn: L. Wendell

Bechtel Group, Inc.
PO Box 3965
San Francisco, CA   94119
Attn: B. Lessley

Dr. George Bergeles
Dept. of Mechanical Engineering
National Technical University
42, Patission Street
Athens, GREECE

Bonneville Power Administration
PO Box 3621
Portland, OR   97208
Attn: N. Butler

Burns & Roe, Inc.
800 Kinderkamack Road
Oradell, NJ   07649
Attn: G. A. Fontana

Canadian Standards Association
178 Rexdale Blvd.
Rexdale, Ontario, M9W 1R3
CANADA
Attn: T. Watson

Professor V. A. L. Chasteau
School of Engineering
University of Auckland
Private Bag
Auckland, NEW ZEALAND

Colorado State University
Dept. of Civil Engineering
Fort Collins, CO   80521
Attn: R. N. Meroney

Commonwealth Electric Co.
Box 368
Vineyard Haven, MA   02568
Attn: D. W. Dunham

Gale B. Curtis
Curtis Associates
3089 Oro Blanco Drive
Colorado Springs, CO   80917

M. M. Curvin
11169 Loop Road
Soddy Daisy, TN   37379

Department of Economic Planning
  and Development
Barrett Building
Cheyenne, WY   82002
Attn: G. N. Monsson

Otto de Vries
National Aerospace Laboratory
Anthony Fokkerweg 2
Amsterdam 1017
THE NETHERLANDS

DOE/ALO
Albuquerque, NM   87115
Attn: G. P. Tennyson

DOE/ALO
Energy Technology Liaison Office
NGD
Albuquerque, NM   87115
Attn: Capt. J. L. Hanson, USAF

DOE Headquarters (20)
Wind/Oceans Technologies Division
1000 Independence Avenue
Washington, DC   20585
Attn: D. F. Ancona
       P. R. Goldman

J. B. Dragt
Nederlands Energy Research Foundation
(E.C.N.)
Physics Department
Westerduinweg 3 Petten (nh)
THE NETHERLANDS

Dynergy Systems Corporation
821 West L Street
Los Banos, CA   93635
Attn: C. Fagundes

Dr. Norman E. Farb
10705 Providence Drive
Villa Park, CA   92667

Electric Power Research Institute
3412 Hillview Avenue
Palo Alto, CA   94304
Attn: E. Demeo
       F. Goodman

Alcir de Faro Orlando
Pontificia Universidade Catolica-PUC/Rj
Mechanical Engineering Department
R. Marques de S. Vicente 225
Rio de Janeiro, BRAZIL

A. D. Garrad
Garrad Hasson
10 Northampton Square
London EC1M 5PA
UNITED KINGDOM

Gates Learjet
Mid-Continent Airport
PO Box 7707
Wichita, KS   67277
Attn: G. D. Park

H. Gerardin
Mechanical Engineering Department
Faculty of Sciences and Engineering
Universite Laval-Quebec, G1K 7P4
CANADA

R. T. Griffiths
University College of Swansea
Dept. of Mechanical Engineering
Singleton Park
Swansea, SA2 8PP
UNITED KINGDOM

Helion, Inc.
Box 445
Brownsville, CA   95919
Attn: J. Park, President

FloWind Corporation (3)
1183 Quarry Lane
Pleasonton, CA   94566
Attn: L. Schienbein
       I. Vas
       B. Im

Indal Technologies, Inc. (2)
3570 Hawkestone Road
Mississauga, Ontario
CANADA L5C 2V8
Attn: D. Malcolm
       C. Wood

Institut de Recherche d'Hydro-Quebec
1800, Montee Ste-Julie
Varennes, Quebec, JOL 2P0
CANADA
Attn: Gaston Beaulieu
       Bernard Masse

Iowa State University
Agricultural Engineering, Room 213
Ames, IA   50010
Attn: L. H. Soderholm

K. Jackson
West Wind Industries
P.O. Box 1705
Davis, CA   95617

M. Jackson
McAllester Financial
1816 Summit
W. Lafayette, IN   47906

Kaiser Aluminum and Chemical
  Sales, Inc.
14200 Cottage Grove Avenue
Dolton, IL   60419
Attn: A. A. Hagman

Kaiser Aluminum and Chemical
  Sales, Inc.
6177 Sunol Blvd.
PO Box 877
Pleasonton, CA   94566
Attn: D. D. Doerr

Kansas State University
Electrical Engineering Department
Manhattan, KS   66506
Attn: Dr. G. L. Johnson

R. E. Kelland
The College of Trades and Technology
PO Box 1693
Prince Philip Drive
St. John's, Newfoundland, A1C 5P7
CANADA

KW Control Systems, Inc.
RD#4, Box 914C
South Plank Road
Middletown, NY   10940
Attn: R. H. Klein

Kalman Nagy Lehoczky
Cort Adelers GT. 30
Oslo 2, NORWAY

L. K. Liljergren
1260 S.E. Walnut #5
Tustin, CA   92680

L. Liljidahl
Building 005, Room 304
Barc-West
Beltsville, MD   20705

Olle Ljungstrom
FFA, The Aeronautical Research
Institute
Box 11021
S-16111 Bromma, SWEDEN

Robert Lynette
R. Lynette & Assoc., Inc.
15921 SE 46th Way
Bellevue, WA   98006

Massachusetts Institute of Technology
77 Massachusetts Avenue
Cambridge, MA   02139
Attn: Professor N. D. Ham
         W. L. Harris, Aero/Astro Dept.

H. S. Matsuda
Composite Materials Laboratory
Pioneering R&D Laboratories
Toray Industries, Inc.
Sonoyama, Otsu, Shiga, JAPAN   520

G. M. McNerney
US Wind Power
160 Wheeler Road
Burlington, MA   01803

Michigan State University
Division of Engineering Research
East Lansing, MI   48825
Attn: O. Krauss

Napier College of Commerce and
Technology
Tutor Librarian, Technology Faculty
Colinton Road
Edinburgh, EH10 5DT
ENGLAND

National Rural Electric
  Cooperative Assn
1800 Massachusetts Avenue NW
Washington, DC   20036
Attn: Wilson Prichett, III

Natural Power, Inc.
New Boston, NH   03070
Attn: Leander Nichols

Northwestern University
Dept. of Civil Engineering
Evanston, IL   60201
Attn: R. A. Parmalee

Ohio State University
Aeronautical and Astronautical Dept.
2070 Neil Avenue
Columbus, OH   43210
Attn: Professor G. Gregorek

Oklahoma State University
Mechanical Engineering Dept.
Stillwater, OK   76074
Attn: D. K. McLaughlin

Oregon State University
Mechanical Engineering Dept.
Corvallis, OR   97331
Attn: R. E. Wilson

Pacific Gas & Electric
3400 Crow Canyon Road
San Ramon, CA   94583
Attn: T. Hillesland

Ion Paraschivoiu
Department of Mechanical Engineering
Ecole Polytecnique
CP 6079
Succursale A
Montreal H3C 3A7
CANADA

Riso National Laboratory
Postbox 49
DK-4000 Roskilde
DENMARK
Attn: Troels Friis Pedersen
        Helge Petersen

Jacques Plante
Hydro Quebec
Place Dupuis Ile etage
855 est rue Ste-Catherine
Montreal, Quebec
CANADA H2L 4P5

The Power Company, Inc.
PO Box 221
Genesee Depot, WI   53217
Attn: A. A. Nedd

Power Technologies Inc.
PO Box 1058
Schenectady, NY   12301-1058
Attn: Eric N. Hinrichsen

Public Service Co. of New Hampshire
1000 Elm Street
Manchester, NH   03105
Attn: D. L. C. Frederick

Public Service Company of New Mexico
PO Box 2267
Albuquerque, NM   87103
Attn: M. Lechner

RANN, Inc.
260 Sheridan Ave., Suite 414
Palo Alto, CA   94306
Attn: A. J. Eggers, Jr.

The Resources Agency
Department of Water Resources
   Energy Division
PO Box 388
Sacramento, CA   95802
Attn: R. G. Ferreira

Dr. R. Ganesh Rajagopalan, Asst. Prof.
Aerospace Engineering Department
Iowa State University
404 Town Engineering Bldg.
Ames, IA   50011

Reynolds Metals Company
Mill Products Division
6601 West Broad Street
Richmond, VA   23261
Attn: G. E. Lennox

R. G. Richards
Atlantic Wind Test Site
PO Box 189
Tignish P.E.I., COB 2B0
CANADA

A. Robb
Memorial University of Newfoundland
Faculty of Engineering and Applied
Sciences
St. John's Newfoundland, A1C 5S7
CANADA

Solar Energy Research Institute
1617 Cole Boulevard
Golden, CO   80401
Attn: R. W. Thresher

Dr. Ing. Hans Ruscheweyh
Institut fur Leichbau
Technische Hochschule Aachen
Wullnerstrasse 7
FEDERAL REPUBLIC OF GERMANY

Beatrice de Saint Louvent
Establissement d'Etudes et de
Recherches
  Meteorologigues
77 Rue de Serves
92106 Boulogne-Billancourt Cedex
FRANCE

Gwen Schreiner
Librarian
National Atomic Museum
Albuquerque, NM   87185

Arnan Seginer
Professor of Aerodynamics
Technion-Israel Institute of Technology
Department of Aeronautical Engineering
Haifa
ISRAEL

Mr. Farrell Smith Seiler, Editor
Wind Energy Abstracts
PO Box 3870
Bozeman, MT   59772-3870

David Sharpe
Dept. of Aeronautical Engineering
Queen Mary College
Mile End Road
London, E1 4NS
UNITED KINGDOM

Kent Smith
Instituto Technologico Costa Rico
Apartado 159 Cartago
COSTA RICA

Bent Sorenson
Roskilde University Center
Energy Group, Bldg. 17.2
IMFUFA
PO Box 260
DK-400 Roskilde
DENMARK

Peter South
ADECON
32 Rivalda Road
Weston, Ontario, M9M 2M3
CANADA

Southern California Edison
Research & Development Dept., Room 497
PO Box 800
Rosemead, CA   91770
Attn: R. L. Scheffler

G. Stacey
The University of Reading
Department of Engineering
Whiteknights, Reading, RG6 2AY
ENGLAND

Stanford University
Dept. of Aeronautics and
  Astronautics Mechanical Engineering
Stanford, CA   94305
Attn: Holt Ashley

Dr. Derek Taylor
Alternative Energy Group
Walton Hall
Open University
Milton Keynes, MK7 6AA
UNITED KINGDOM

R. J. Templin (3)
Low Speed Aerodynamics Laboratory
NRC-National Aeronautical Establishment
Montreal Road
Ottawa, Ontario, K1A OR6
CANADA

Texas Tech University (2)
Mechanical Engineering Dept.
PO Box 4289
Lubbock, TX   79409
Attn: J. W. Oler

K. J. Touryan
Moriah Research
6200 Plateau Dr.
Englewood, CO   80111

Tulane University
Dept. of Mechanical Engineering
New Orleans, LA   70018
Attn: R. G. Watts

Tumac Industries, Inc.
650 Ford Street
Colorado Springs, CO   80915
Attn: J. R. McConnell

J. M. Turner
Terrestrial Energy Technology
  Program Office
Energy Conversion Branch
Aerospace Power Division/
  Aero Propulsion Lab
Air Force Systems Command (AFSC)
Wright-Patterson AFB, OH   45433

United Engineers and Constructors, Inc.
PO Box 8223
Philadelphia, PA   19101
Attn: A. J. Karalis

Universal Data Systems
5000 Bradford Drive
Huntsville, AL   35805
ATTN: C. W. Dodd

University of California
Institute of Geophysics
  and Planetary Physics
Riverside, CA   92521
Attn: Dr. P. J. Baum

University of Colorado
Dept. of Aerospace Engineering Sciences
Boulder, CO   80309
Attn: J. D. Fock, Jr.

University of Massachusetts
Mechanical and Aerospace
  Engineering Dept.
Amherst, MA   01003
Attn: Dr. D. E. Cromack

University of New Mexico
New Mexico Engineering
  Research Institute
Campus P.O. Box 25
Albuquerque, NM   87131
Attn: G. G. Leigh

University of Oklahoma
Aero Engineering Department
Norman, OK   73069
Attn: K. Bergey

University of Sherbrooke
Faculty of Applied Science
Sherbrooke, Quebec, J1K 2R1
CANADA
Attn: A. Laneville
       P. Vittecoq

The University of Tennessee
Dept. of Electrical Engineering
Knoxville, TN   37916
Attn: T. W. Reddoch

USDA, Agricultural Research Service
Southwest Great Plains Research Center
Bushland, TX   79012
Attn: Dr. R. N. Clark

Utah Power and Light Co.
51 East Main Street
PO Box 277
American Fork, UT   84003
Attn: K. R. Rasmussen

Dirk Vandenberghe
State Univ. of Ghent
St. Pietersniewstraat 41
9000 Ghent
BELGIUM

W. A. Vachon
W. A. Vachon & Associates
PO Box 149
Manchester, MA   01944

VAWTPOWER, Inc.
134 Rio Rancho Drive
Rio Rancho, NM   87124
Attn: P. N. Vosburgh

Washington State University
Dept. of Electrical Engineering
Pullman, WA   99163
Attn: F. K. Bechtel

West Texas State University
Government Depository Library
Number 613
Canyon, TX   79015

West Texas State University
Department of Physics
P.O. Box 248
Canyon, TX   79016
Attn: V. Nelson

West Virginia University
Dept. of Aero Engineering
1062 Kountz Avenue
Morgantown, WV   26505
Attn: R. Walters

D. Westlind
Central Lincoln People's Utility
District
2129 North Coast Highway
Newport, OR   97365-1795

Wichita State University
Aero Engineering Department (2)
Wichita, KS   67208
Attn: M. Snyder
       W. Wentz

Wind Power Digest
PO Box 700
Bascom, OH   44809
Attn: Michael Evans

Wisconsin Division of State Energy
8th Floor
101 South Webster Street
Madison, WI   53702
Attn: Wind Program Manager

1520	D. J. McCloskey
1522	R. C. Reuter, Jr.
1523	J. H. Biffle
1524	A. K. Miller
1524	D. W. Lobitz
1550	R. C. Maydew
1556	G. F. Homicz
2525	R. P. Clark
3141-1	C. M. Ostrander (5)
3151	W. L. Garner (3)
3154-3	C. H. Dalin (28) For DOE/OSTI (Unlimited Release)
3160	J. E. Mitchell (15)
3161	P. S. Wilson
6000	D. L. Hartley
6200	V. L. Dugan
6220	D. G. Schueler
6225	H. M. Dodd (50)
6225	T. D. Ashwill
6225	D. E. Berg
6225	L. R. Gallo
6225	P. C. Klimas
6225	D. S. Oscar
6225	M. E. Ralph
6225	D. C. Reda
6225	M. A. Rumsey
6225	L. L. Schulter
6225	W. A. Stephenson
6225	H. J. Sutherland

7111	J. W. Reed
7544	D. R. Schafer
7544	T. G. Carne
7544	J. Lauffer
8024	P. W. Dean
9100	R. G. Clem
9122	T. M. Leonard